

Electronic Theses and Dissertations, 2004-2019

2005

System Design And Optimization Of Optical Coherence Tomography

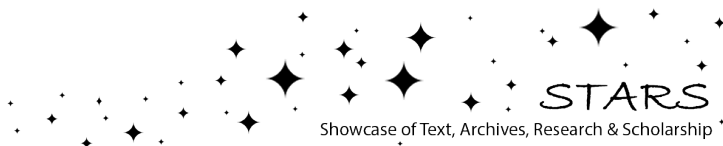
Avni Ceyhun Akcay
University of Central Florida

 Part of the [Electromagnetics and Photonics Commons](#), and the [Optics Commons](#)
Find similar works at: <https://stars.library.ucf.edu/etd>
University of Central Florida Libraries <http://library.ucf.edu>

This Doctoral Dissertation (Open Access) is brought to you for free and open access by STARS. It has been accepted for inclusion in Electronic Theses and Dissertations, 2004-2019 by an authorized administrator of STARS. For more information, please contact STARS@ucf.edu.

STARS Citation

Akcay, Avni Ceyhun, "System Design And Optimization Of Optical Coherence Tomography" (2005).
Electronic Theses and Dissertations, 2004-2019. 423.
<https://stars.library.ucf.edu/etd/423>



SYSTEM DESIGN AND OPTIMIZATION
OF OPTICAL COHERENCE TOMOGRAPHY

by

AVNI CEYHUN AKCAY

B.S. Middle East Technical University, Ankara, Turkey 1999
M.S. University of Central Florida, Orlando 2001

A dissertation submitted in partial fulfillment of the requirements
for the degree of Doctor of Philosophy
in the College of Optics and Photonics
at the University of Central Florida
Orlando, Florida

Summer Term
2005

Major Professor: Jannick P. Rolland

© 2005 Avni Ceyhun Akcay

ABSTRACT

Optical coherence imaging, including tomography (OCT) and microscopy (OCM), has been a growing research field in biomedical optical imaging in the last decade. In this imaging modality, a broadband light source, thus of short temporal coherence length, is used to perform imaging via interferometry. A challenge in optical coherence imaging, as in any imaging system towards biomedical diagnosis, is the quantification of image quality and optimization of the system components, both a primary focus of this research. We concentrated our efforts on the optimization of the imaging system from two main standpoints: axial point spread function (PSF) and practical steps towards compact low-cost solutions.

Up to recently, the criteria for the quality of a system was based on speed of imaging, sensitivity, and particularly axial resolution estimated solely from the full-width at half-maximum (FWHM) of the axial PSF with the common practice of assuming a Gaussian source power spectrum. As part of our work to quantify axial resolution we first brought forth two more metrics unlike FWHM, which accounted for side lobes in the axial PSF caused by irregularities in the shape of the source power spectrum, such as spectral dips. Subsequently, we presented a method where the axial PSF was significantly optimized by suppressing the side lobes occurring because of the irregular shape of the source power spectrum. The optimization was performed through optically shaping the source power spectrum via a programmable spectral shaper, which consequentially led to suppression of spurious structures in the images of a layered specimen. The superiority of the demonstrated approach was in performing reshaping before imaging, thus eliminating the need for post-data acquisition digital signal processing. Importantly, towards the optimization

and objective image quality assessment in optical coherence imaging, the impact of source spectral shaping was further analyzed in a task-based assessment method based on statistical decision theory. Two classification tasks, a signal-detection task and a resolution task, were investigated. Results showed that reshaping the source power spectrum was a benefit essentially to the resolution task, as opposed to both the detection and resolution tasks, and the importance of the specimen local variations in index of refraction on the resolution task was demonstrated.

Finally, towards the optimization of OCT and OCM for use in clinical settings, we analyzed the detection electronics stage, which is a crucial component of the system that is designed to capture extremely weak interferometric signals in biomedical and biological imaging applications. We designed and tested detection electronics to achieve a compact and low-cost solution for portable imaging units and demonstrated that the design provided an equivalent performance to the commercial lock-in amplifier considering the system sensitivity obtained with both detection schemes.

To my wife Anil

To my family

ACKNOWLEDGMENTS

Preeminently, I thank my advisor, Dr. Jannick Rolland, for guiding and supporting me to reach the success in this research and for believing in me and motivating me to achieve higher standards in my work. I want to thank the committee members, Dr. Peter Delfyett, Dr. Guifang Li, and Dr. Ratna Chakrabarti not only for their interest in this work, but also for their great input to my work sometimes by answering my questions, and sometimes by providing me access to their valuable laboratory equipment. I would like to thank Dr. Jason Eichenholz of Newport Corporation and the fellow Newport employees for providing us the means to carry out the optical spectral shaping experiment, Dr. Lars Furenlid at University of Arizona for sharing his expertise and for working with us together on the design and implementation of detection electronics, Dr. Eric Clarkson at University of Arizona for his contributions in the studies for the quantification of resolution and for his help with the derivation of the task-based performance assessment method, and Marko Slusarczyk of the Optoelectronics Industry Development Association (OIDA) for working with us through the Photonics Technology Access Program to obtain custom-designed broadband fiber couplers. I would like to thank the members of ODALab who directly or indirectly had input to this work: post docs, graduate students and interns. Specifically I thank the fellow students Kye-Sung Lee for his support and help he provided, Jason O'Daniel and Tony Delemos for their contributions in studies on modeling task-based performance analysis in Matlab, Pascale Parrein for her input to the work on quantification of axial resolution. I also thank the whole ODA team for their friendship and their critical evaluations of my presentations in group meetings. I thank my friends, who shared their

friendship generously, around me in CREOL and Orlando, and those who are far away in other places in the US or in Turkey.

My very special thanks go to my family; my father Husamettin, my mother Nilgun, my brother Cem and my twin sisters Cigdem and Ozlem for their love, unconditional support and encouragement, and particularly to my lovely wife Anil for her patience, support and endless love, which has been a major motivation for me all the time, and for being the source of joy and happiness in my life.

TABLE OF CONTENTS

ABSTRACT	iii
ACKNOWLEDGMENTS	vi
TABLE OF CONTENTS.....	viii
LIST OF FIGURES	xi
LIST OF TABLES.....	xvi
LIST OF ACRONYMS	xvii
CHAPTER ONE: INTRODUCTION.....	1
1.1 Optics in Medicine.....	1
1.2 Michelson Interferometer.....	3
1.3 Michelson Interferometer and Low-Coherence Imaging.....	5
1.4 Motivation.....	7
1.5 Research Summary	8
1.6 Dissertation Outline	9
CHAPTER TWO: RELATED WORK.....	12
2.1 Low-Coherence Interferometry in the Telecommunications Industry.....	12
2.2 Development of OCT.....	15
2.3 Advancements in OCT.....	17
CHAPTER THREE: PRINCIPLES AND THEORY OF OCT	24
3.1 Michelson Interferometry with Monochromatic Stationary Source	24
3.2 Principles of Low-Coherence Interferometry	28
3.3 OCT Signal.....	34

3.4	Discussion	40
CHAPTER FOUR: QUANTIFICATION OF RESOLUTION IN OCT		44
4.1	Lateral Resolution	44
4.2	Metrics for Axial Resolution	45
4.2.1	<i>Computing the Coherence Length</i>	47
4.2.2	<i>Coherence Length and Resolution</i>	48
4.3	Simulation Results	51
4.3.1	<i>Real PSD versus ideal PSD</i>	51
4.3.2	<i>Computation of Coherence Lengths of Sources with Extended PSDs</i>	56
4.3.3	<i>Ability to Resolve Two Layers</i>	59
4.3.4	<i>Discussion</i>	61
4.4	Task-based Metric	64
CHAPTER FIVE: OPTICAL SPECTRUM SHAPING FOR OPTIMIZATION OF THE PSF IN OCT		67
5.1	Improved the PSF by Optical Spectral Shaping	67
5.2	Possible Extension: Modular Optical Spectral Shaper	79
5.3	The Impact of Spectral Shaping on Task-Based Assessment	85
5.3.1	<i>Mathematical Model</i>	86
5.3.2	<i>Evaluation of the Hotelling Observer Performance</i>	88
5.3.3	<i>Task Definitions</i>	91
5.3.4	<i>Simulation Results</i>	94
5.3.4.1	<i>Signal-Detection Task</i>	96

5.3.4.2	<i>Resolution Task</i>	100
5.3.5	<i>Discussion</i>	102
CHAPTER SIX: DETECTION ELECTRONICS IN OCT		105
6.1	Analog Signal Processing.....	105
6.2	Imaging System	112
6.3	Custom-designed Detection Electronics.....	115
6.4	Results.....	119
6.5	Discussion.....	123
CHAPTER SEVEN: SUMMARY OF CONTRIBUTIONS AND CONCLUSION.....		125
APPENDIX A: CIRCUITRY OF DETECTION ELECTRONICS.....		129
APPENDIX B: LABVIEW INTERFACE.....		135
LIST OF REFERENCES.....		138

LIST OF FIGURES

Figure 1.1: A sketch of the Albert Michelson's <i>interferential refractor</i> , which is now universally called a Michelson interferometer. The light source employed was a small lantern with its flame at focal point of a lens.....	4
Figure 3.1: Schematic diagram of (a) a free-space and (b) a fiber-optic Michelson interferometer with the electric fields and their propagation distances traveled in the interferometer arms shown. PD: Photodetector, CL: Collimating Lens.....	26
Figure 3.2. Illustration of the interference phenomenon with a long coherence length (quasi-monochromatic) and a short coherence length (broadband) light sources.	31
Figure 3.3: A computer generated PSD which represents a virtual broadband light source	41
Figure 3.4: The interference signal simulated under ideal conditions according to the PSD shown in Figure 3.3. The dashed line is the envelope of the signal.....	42
Figure 3.5: Interference signal after demodulation, i.e. the envelope of the interference signal (a) in linear scale, (b) in logarithmic scale.	43
Figure 4.1: A specimen model with two layers to determine the axial resolution. Δz is the separation between the two layers n and n' are the refractive indices.....	50
Figure 4.2: (a) Measured PSD of the SLD-471: the normalized Gaussian PSD and the normalized Lorentzian PSD ($\lambda_o=950$ nm, $\Delta\lambda=62$ nm for each), (b) corresponding PSFs, i.e. modulus of the complex degree of temporal coherence functions.....	54

Figure 4.3: A Gaussian PSD with 100 nm -3 dB spectral bandwidth centered at 940 nm (red dashed line) and PSDs of the same bandwidth and center wavelength with different spectral dip amplitudes. 57

Figure 4.4: The coherence length is presented as a function of the amplitude percentage of the spectral dip in the source PSD computed using the ASI, RMSW and FWHM metrics. 0% dip corresponds to a pure Gaussian PSD, i.e. with no spectral dip..... 58

Figure 4.5: $|\gamma(\tau)|$ of the PSDs of the 100 nm bandwidth centered at 940 nm source with selected percentage of spectral dip. 58

Figure 4.6: Envelopes of the interferometric signals I_1 and I_2 due to backreflections from two successive layers (left column $\Delta z = l_{c.FWHM} / 2$, right column $\Delta z = l_{c.ASI} / 2$, and thus $\Delta \tau = 2\Delta z / c$) and the resulting signal I for a source with (a) Gaussian PSD, (b) Lorentzian PSD, (c) SLD-471 presented in Fig. 4.2(a), and (d) PSD with 8% spectral dip amplitude and (e) PSD with 49.13% spectral dip amplitude presented in Fig. 4.3. 61

Figure 5.1: Selective attenuation of optical power contained in different wavelength bands via DMD [Duncan 2003]. 71

Figure 5.2: Schematic of the experimental setup used for axial PSF measurements: PSP, programmable spectral processor; C, collimator; BS's, beamsplitters; M1, M2, mirrors. 72

Figure 5.3: (a) The source PSD is the blue curve and underneath it a Gaussian PSD is fitted, (b) the transmission function which is obtained from the ratio of the source and Gaussian PSDs shown in (a) and is then rounded to one decimal place to accommodate 0.1 dB amplitude resolution, (c) the source PSD (blue curve) is presented with the resulting PSD underneath it measured using the transmission curve shown in (b). 74

Figure 5.4: (a) The transmission functions to be transferred to the PSP to smooth the shape of the source power spectrum, (b) the power spectra measured with an OSA before and after spectral shaping: S_0 ; unshaped power spectrum, S_1 ; shaped power spectrum obtained with T_1 , and S_2 ; shaped power spectrum obtained with T_2 75

Figure 5.5: The PSFs recorded experimentally. We compare the change in PSF after first spectral shaping operation in (a), and after second one in (b) to the PSF recorded with the unshaped source power spectrum. 77

Figure 5.6: Images of onion before (a) and after (b) spectral shaping..... 78

Figure 5.7: Schematic that presents a possible structure for an optical spectral shaper..... 80

Figure 5.8: Transmission curve of DMD provided in three different versions. [Dudley 2003]. The yellow shaded area shows the range most OCT light sources emit at. 83

Figure 5.9: Beam profile (a) at the output of fiber collimator, (b) after DMD with micromirrors all tilted $+12^\circ$, and (c) after DMD where mirrors form a ‘checker image’ 85

Figure 5.10: Specimen model: n is the refractive index of the specimen and Δn is the change of refractive index from the specimen to the substrate. 91

Figure 5.11: The structure of the specimen which presents the cases when the hypothesis is true for (a) signal detection task where the difference in refractive index between specimen and the substrate Δn is the variable, and (b) resolution task where the specimen thickness is the variable..... 93

Figure 5.12: The frequency power spectrum of the ASE source S_0 ; solid curve, power spectrum after the first shaping operation S_1 (i.e.dotted curve) and after the second shaping operation S_2 (i.e. dashed curve)..... 95

Figure 5.13: (a) Detectability and (b) AUC as a function of change in refractive index Δn between the specimen and the substrate.	98
Figure 5.14: Power spectra each normalized to have unit optical power.	99
Figure 5.15: AUC curves computed using the power spectra shown in Figure 5.10.	99
Figure 5.16: Detectability as a function of the specimen thickness for the ASE source (a) with the power spectrum S_0 , (b) with the shaped power spectrum S_1 , and (c) with the shaped power spectrum S_2 which are shown in Figure 5.8, and the corresponding AUC as a function of the specimen thickness for the power spectra(d) S_0 , (e) S_1 , and (f) S_2	102
Figure 6.1: Interference signal phase modulated by a piezoelectric fiber stretcher driven at 20 kHz.....	110
Figure 6.2: Schematic of the time-domain OCT system implemented with dual-balanced detection. SLD: Superluminescent Diode, FC: Fiber Coupler, PM: piezoelectric phase modulator. A PCI DAQ card in the PC acquires the signal processed by the detection electronics. The PC also controls the scanning stages.....	113
Figure 6.3: Diagram of a lock-in amplifier.....	115
Figure 6.4: Schematic of the detection electronics designed to demodulate the OCT signal generated at the dual-balanced photoreceiver. BPF: Bandpass Filter, LPF: Low Pass Filter.	117
Figure 6.5: The output response of the detection electronics with and without the filtering and additional gain at the final stage.	118

Figure 6.6: Input and output waveform relation of the designed OCT demodulator. Bottom sinusoid is the input waveform V_{in} . The middle curve is the output V_{out1} when the LPF is bypassed and the top curve V_{out2} is the output when the LPF is switched on.	118
Figure 6.7: Photo of the printed circuit board designed for filtering and envelope detection. ...	119
Figure 6.8: The sample configuration to determine the sensitivity of the OCT system shown in Figure 6.1.	120
Figure 6.9: The OCT signals recorded using (a) the lock-in amplifier (SR830), (b) the custom-designed logarithmic amplifier-based detection electronics.	121
Figure 6.10: Onion image ($500 \mu\text{m} \times 640 \mu\text{m}$) where (a) the lock-in amplifier is employed to perform envelope detection, (b) the designed detection electronics is employed to process the analog signal generated by the photoreceiver.	123
Figure A.1: BPF circuitry	131
Figure A.2: Circuitry of the demodulation, i.e. envelope detection stage	132
Figure A.3: Circuitry of LPF	133
Figure A.4: Power supply circuitry.....	134
Figure B.1: The screen capture of the LabView interface where the parameters for imaging are entered. Such parameters are the speed of the stages, the distance they travel at each step, the sampling rate of the data acquisition and the number of samples recorded at each axial-scan.	136
Figure B.2: A screen capture of the LabView blockdiagram of the code controlling the stages and DAQ.....	137

LIST OF TABLES

Table 2.1 Summary of some of the broadband light sources for OCT imaging.....	22
Table 4.1 Coherence length of a Gaussian and Lorentzian PSD formulated for three metrics ...	53
Table 4.2 Coherence length of Sources with different shaped PSDs	55
Table 5.1 Axial resolution for the differently shaped power spectra computed according to three metrics described in Chapter 4.....	77
Table 6.1 System sensitivity S for the two detection electronics.....	122

LIST OF ACRONYMS

AC	Alternating Current
ASE	Amplified Spontaneous Emission
ASI	Absolute Square Integral
BPF	Bandpass Filter
DAQ	Data Acquisition
DC	Direct Current
DLP	Digital Light Processor
DMD	Digital Micro mirror Device
FWHM	Full-Width at Half-Maximum
GPIB	General Purpose Interface Bus
LPF	Low Pass Filter
NA	Numerical Aperture
NIR	Near-Infrared
OCDR	Optical Coherence-Domain Reflectometry
OCM	Optical Coherence Microscopy
OCT	Optical Coherence Tomography
OLCR	Optical Low-Coherence Reflectometry
OSA	Optical Spectrum Analyzer
PDF	Probability Density Function
PSD	Power Spectral Density (also called Power Spectrum)
PSF	Point Spread Function

PSP	Programmable Spectral Processor
RF	Radio Frequency
RMS	Root-Mean-Square
RMSW	Root-Mean-Square Width
RSOD	Rapid-Scanning Optical Delayline
SLD	Superluminescent Diode
SNR	Signal-to-Noise Ratio

CHAPTER ONE: INTRODUCTION

This part of the dissertation starts with a summary of the role of optics on medicine. Then, the origin and basics of biomedical optical imaging with interferometry will be discussed. Preliminary studies toward the invention of optical coherence tomography (OCT) and initial work on the subject will be reviewed. Finally, our motivation for the research and summary followed by the dissertation outline will be presented.

1.1 Optics in Medicine

We can state that the history of optics in medicine starts with the invention of the microscope. Microscopes have been used by scientists to magnify samples such as biological specimen since the late 17th century. However, simple microscopes are not able to provide images of the inner structures of specimens *in vivo*. Later, the discovery of x-rays by William Roentgen in 1895 enabled a new medical imaging system which measures the transmission of x-rays through biological materials such as the human body [Macovski 1983]. X-ray computerized tomography then emerged that deduced the spatial distribution of the absorption coefficient of portions of the human body based on a mathematical solution derived by J. Radon [Born and Wolf 2002]. Since x-rays were found not to be useful for scanning the soft tissues as they penetrate and pass through the soft tissue without significant change, other techniques such as ultrasound imaging were proposed to diagnose soft tissue [Fenster 2000]. A major drawback of ultrasound imaging is the poor resolution. To obtain images with higher resolution, techniques such as diffraction

tomography was developed. However, reconstruction of images with diffraction tomography is more complicated. Other techniques have thus been developed to obtain see through images of the human body. Magnetic resonance imaging is an important example [US Patent No. 4,319,190].

The interaction of light with biological systems has attracted the attention of scientists for a long time [Tuchin 2002]. Optical properties of tissues have been investigated since the early 1900's. Optical biomedical imaging techniques are based on one or more of the transmission, absorption, reflection, scattering and fluorescence of the light when it is incident on tissue. The studies showed that absorption of light in biological samples, such as skin and blood, is significantly low in an optical window between ~600 nm and ~1300 nm which is called the diagnostic and therapeutic window [Parrish 1981, Anderson 1981, and Roggan 1999]. Light emitted in this window can penetrate deeper into the tissue due to relatively low absorption enabling transfer of optical information from the inside of tissues. Outside this window, light is absorbed in short distance disabling penetration in the tissues because of high water absorption in the infrared, as given that 80% of the human body consists of water, and because of absorption and scattering by proteins and molecules in the ultraviolet [Tuchin 2002, Mobley 2003].

Different optical devices has been developed and/or employed to benefit from light in medicine some of which are based on historical instruments. For example the Michelson interferometer in biomedical optical imaging enables measuring the optical properties of light which can be used for biondiagnosis.

1.2 Michelson Interferometer

The physical structure of an OCT setup is based on a device invented by Albert Abraham Michelson, which is called the Michelson interferometer. The Michelson interferometer is used as the basis for all of the experimental setups discussed in this dissertation.

After Thomas Young proved that light possesses the properties of wave showing that light can interfere, many optical theories used the concept that there existed a medium in the whole universe called *luminiferous ether* which made the propagation of electromagnetic waves and thus light possible, since the scientists at that time believed that light could not propagate in empty space. For example, Maxwell studied mathematics of electromagnetism presuming that the propagation medium was *luminiferous ether*. It was assumed that the *luminiferous ether* was transparent, stationary and filled the whole space in the universe creating an absolute frame of reference.

The instrument, which is universally named as the Michelson interferometer, was invented by Albert A. Michelson in late 19th century. He planned to run an experiment to study the existence of the *luminiferous ether*, through which the earth was assumed to be moving. His idea was to build an apparatus which was supposed to have two arms perpendicular to each other, with one arm traveling in the direction of the earth's motion. He was expecting the light to travel a longer time in the direction of the earth's motion in *luminiferous ether* and a shorter time in the opposite

direction, and he was considering that the light traveling in the other arm perpendicular to the earth's motion would have traveled back and fourth in the arm in the same time [Michelson 1881].

In his instrument, which he proposed to be employed as an interferential refractor, Albert A. Michelson used a half-silvered, semitransparent glass plate, which is now called a beam splitter, a glass plate which is employed to compensate for the thickness of the half-silvered plate, and two plane glasses silvered on the front surface, namely mirrors. Figure 1.1 shows the structure of the Michelson interferometer as proposed by Albert Michelson [Michelson 1881, Michelson 1887].

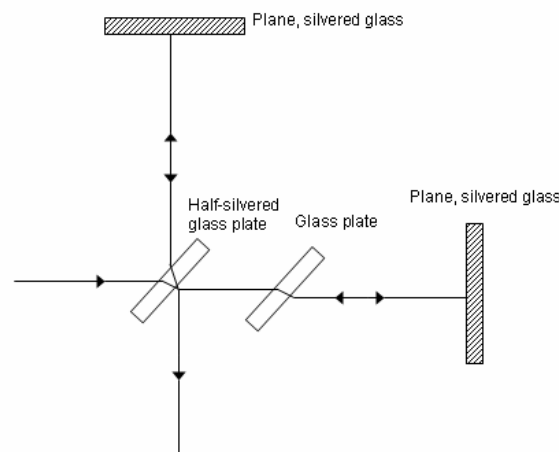


Figure 1.1: A sketch of the Albert Michelson's *interferential refractor*, which is now universally called a Michelson interferometer. The light source employed was a small lantern with its flame at focal point of a lens.

Albert Michelson employed this instrument to observe the interference fringes formed by superimposition of the light from the arms of the interferometer. He considered that there should have been a shift in the position of the interference fringes given that light was expected to travel a longer time in the arm which is in the direction of the earth's motion in the *luminiferous ether*. However, with his instrument he showed that there was no shift in the observed interference fringes which was possible only if there was no *luminiferous ether*, hence light was traveling at the same velocity in all directions. With this work and his results, Albert Michelson became the first US citizen to win the Nobel Prize (1907), as stated by the award committee, "for his optical precision instruments and the spectroscopic and metrological investigations carried out with their aid".

The Michelson interferometer later served in many fields of optics such as interferometric sensors, spectroscopy, reflectometry and biomedical optical imaging.

1.3 Michelson Interferometer and Low-Coherence Imaging

The Michelson interferometer is an amplitude-splitting type of interferometer. Light travels from a source to a beam splitter, which divides the incident light into two different paths generally with equal optical power. Light beams traveling in two different paths are scattered or reflected back, for example from mirrors, so that they follow the path back to the beam splitter where they are recombined and spatially mode-matched. Interference of the light beams is observed at an observation plane or at a photodetector.

Light is an electromagnetic field having an amplitude and phase. In coherent imaging, variations in both the amplitude and the phase of the light are recorded to form an image. The structure of the Michelson interferometer enables changing the phase of the fields while their amplitudes vary depending on the scattering or reflection coefficients of the materials placed at the end of the interferometer arms. Generally, one of the interferometer arms is employed as the reference and is called the reference arm. A sample is placed in the other arm which is called the sample arm. The amplitude variations due to the reflection or backscattering from a sample are detected by a photodetector. The detected amplitude variations are dependent on the relative phase difference between the fields in the interferometer arms.

Low-coherent (i.e. temporal coherence) light sources, which have short coherence time, emit light enclosed in a packet of finite number of waves with different wavelengths. A broad spectral bandwidth is a characteristic identity of low-coherent light sources. Coherence is related to the random nature of the optical fields with its amplitude and/or phase fluctuating in time [Mandel and Wolf 1995, Goodman 1985]. Two light beams from the same light source can be superimposed using a Michelson interferometer. The interference signal obtained at the detector presents the autocorrelation of the random fields, which is also called the temporal coherence function or the self coherence function, if the interfering two beams are equivalent. A time delay is introduced to the fields by varying the length of the interferometer reference arm. A general definition of the coherence time is given by the length of the time delay between the equivalent optical fields when they become uncorrelated. Coherence length is defined as the length of the path traversed by light in vacuum during the coherence time. Low-coherent light sources become

uncorrelated relatively much faster compared to the monochromatic or quasi-monochromatic sources with a narrow spectral bandwidth. Hence light beams from a low-coherent light source are able to interfere only for an extremely short time delay or short distance between them. For a time delay larger than the coherence time, no interference signal can be observed. The short coherence length provided by the low-coherent sources plays a critical role in low-coherence interferometry applications such as testing and investigating optical fibers and devices with a so called optical low-coherence reflectometer, and biomedical imaging with optical coherence tomography (OCT) [Huang 1991a].

1.4 Motivation

Light is a promising medium to be used in biomedical imaging. The Michelson interferometer by itself is an amazing optical instrument that can be used in different applications for different purposes including OCT. Its structural simplicity is an advantage for research. However, a challenge in optical coherence imaging, as in any imaging system towards biomedical diagnosis, is the quantification of image quality and optimization of the system components.

A full system design and optimization of OCT including the light source, the detection technology, and scanning are inevitable to extract useful data from biological samples. OCT is a relatively novel biomedical imaging system which needs to be further improved and optimized in order to be accepted by the medical community in biondiagnosis. Furthermore, important measures in the imaging, such as the axial point spread function and the axial resolution, are to

be carefully quantified. Factors influencing such measures are to be analyzed towards the assessment of image quality, and negative impacts are to be corrected. Also, for such assessment a useful mathematical method needs to be employed for early optimization of the imaging system to save time, energy, and cost. Moreover, compact low-cost solutions are to be developed to ensure portable units that can be employed in clinical settings. One step towards compactness is replacing bulky laboratory equipment, for example the lock-in amplifier, with compact components, for example detection electronics implemented on a small printed circuit board.

1.5 Research Summary

The purpose of the research is the optimization of the OCT system from two main standpoints: axial point spread function (PSF) and practical steps towards compact low-cost solutions.

The axial PSF and axial resolution are mainly related to the spectral characteristics of the imaging light source. In our research we discuss in detail the quantification the axial resolution in an optical coherence imaging system and propose different metrics in order to understand which ones may be more reliable in biomedical imaging, while presenting the results of those metrics especially when the light source employed has irregularities in the shape of its power spectrum. Furthermore, we propose to optically shape the source power spectrum to suppress side lobes in the PSF of the imaging system, which also leads to suppression of spurious structures in the final image reconstructed. Importantly, towards the optimization and objective image quality assessment in optical coherence imaging, impact of source spectral shaping is further analyzed in

a task-based assessment method based on statistical decision theory. In the final part of this research, we study the analog detection of the phase-modulated interference signal and present a compact low-cost design that can achieve equivalent performance to a commercial high end lock-in amplifier.

1.6 Dissertation Outline

The rest of the dissertation is organized in the following way:

Chapter 2 summarizes the previous related work performed on low-coherence interferometry and reflectometry which have played a critical role for the development of OCT, and describes advancements and achievements in research on OCT.

Chapter 3 details the principles and theory of OCT along with the theory of the Michelson interferometer with coherent and low-coherent sources. The imaging system is quantified by developing a mathematical framework presenting the detected interferometric signal.

Chapter 4 discusses resolution in OCT and some of the source parameters influencing it. The axial or longitudinal resolution provides the resolution along the path of depth-scanning which is related to the spectral characteristics of the light source employed in the system. The lateral or transversal resolution is related to the optics focusing in the sample arm. We propose and analyze different metrics for axial resolution, which is the main focus of Chapter 4, and present the

impact of the shape of the source power spectrum on the axial resolution and PSF. Furthermore, we briefly discuss a novel optimization and performance assessment method for optical coherence imaging based on statistical decision theory.

In Chapter 5 we introduce a novel method to improve the PSF of the OCT imaging system. The method is based on shaping the power spectrum of the broadband light source illuminating an OCT system with a technology based digital micromirror device. We demonstrate the suppression of side lobes in the PSF recorded with an ASE light source after the spectral shaping process. We then analyze the impact of the source spectral shaping in a task-based assessment method based on statistical decision theory.

Chapter 6 discusses a crucial component in OCT imaging, which is the detection electronics. First the mathematical background of detection is presented and then the design of compact low-cost demodulating detection electronics with monolithic integrated-circuit active filters and logarithmic amplifier is demonstrated. We quantify the sensitivity of the system with both the designed electronics and the commercial lock-in amplifier, and present images of fresh onion for comparison of two different detection schemes.

Chapter 7 summarizes the contributions of the research presented in this dissertation and discusses the results of the research.

CHAPTER TWO: RELATED WORK

In this chapter, the steps toward the development of the technology leading to OCT imaging are discussed. We review the previous research and advancements achieved in OCT research, which has been a fast growing field in the last decade.

2.1 Low-Coherence Interferometry in the Telecommunications Industry

Light is reflected or backscattered at the interfaces of optical structures where there is an abrupt change in index of refraction. The Michelson interferometer illuminated with a low-coherent light source has been successfully applied to test the continuity of optical structures such as optical fibers. The technique used to detect the location where Rayleigh backscattering and/or Fresnel reflection occur in optical structures has been called optical low-coherence reflectometry (OLCR), also known as optical coherence-domain reflectometry (OCDR).

In 1987 Youngquist et al. proposed to replace one of the mirrors in a free-space Michelson interferometer with a miniature optical assembly [Youngquist 1987]. They employed a laser diode with short coherence length to illuminate the interferometer. Given that the interference of the light beams recombined at the beam splitter occurs only when the beams are coherent (i.e. time delay between the beams is as short as the coherence time of the light source) Youngquist presented locations in optical assemblies where reflections occurred with 10 μm resolution.

Danielson and Whittenberg, meanwhile, introduced a new type of reflectometer which they used to test single-mode optical fibers [Danielson 1987]. They built a fiber-optic Michelson interferometer illuminated by an LED and used directional couplers instead of beam splitters. Measuring the interference signal occurring due to Fresnel reflections in discrete locations along the fiber, they determined the gap separation in a single-mode optical fiber, loss due to this separation, and the effect of stress applied to the optical fiber on the interferogram. They also discussed that dispersion in the two arms of the fiber-optic interferometer is to be matched to prevent broadening in the interference signal. Later in 1991 Danielson et al. proposed to measure the phase slope of the Fourier components of the interference signal detected in time domain in order to determine the locations of the reflections with higher precision [Danielson 1991]. A dispersive sample was employed in the sample arm of the interferometer.

A group in Japan, Takada et al., again in 1987 reported experiments to locate the faults in optical waveguides devices with a fiber-optic Mach-Zehnder interferometer in combination with a free-space Michelson interferometer [Takada 1987]. Takada et al. employed a superluminescent diode (SLD) with a coherence length of 50 μm . A fiber-optic Mach-Zehnder interferometer was built with a fixed mirror at the end of the reference arm and a fixed optical fiber or waveguide in the other arm. Light beams reflected from the reference mirror, and reflected or backscattered from the optical fiber or waveguide were directed to a free-space Michelson interferometer. The Michelson interferometer consisted of a fixed mirror in one arm and another mirror placed on a translating stage in the other arm. Optical path difference was introduced in the Michelson interferometer by moving the mirror where light beams were superimposed and detected by a Si

PIN diode. Takada et al. modulated the light in the sample arm of the Mach-Zehnder interferometer and performed envelope detection with a lock-in amplifier. The lock-in amplifier was set to detect the signal to account for the frequency of modulation plus the frequency shift introduced by the moving mirror in the Michelson interferometer. The fiber-optic Mach-Zehnder interferometer provided the sum of the reference field and sample field with low coupling loss while the correlation was obtained in the Michelson interferometer. They reported a measurement sensitivity of -116 dB and estimated the spatial resolution to be 380 μm which was the displacement in the mirror location by which the signal dropped to a noise level of -116 dB. Takada et al. also estimated the refractive index of the fiber core under test by immersing the fiber end to index matching oil and measuring the amplitude of the interference signal while changing the refractive index of the index matching oil. No reflection and thus no interference signal were expected when the refractive indices of the fiber core and index matching oil were equivalent.

The development of OLCR in telecommunication industry was reviewed by Gilgen et al. [Gilgen 1989] and Masters [Masters 1999]. The achievements of high spatial resolution and dynamic range in OLCR later inspired some research groups to apply it to form 2-dimensional tomographic images of biological samples.

2.2 Development of OCT

Huang *et al.* recognized that the principles of low-coherence interferometry were analogous to ultrasound imaging [Huang 1991a]. The idea to measure the reflections and scatterings of waves from biological samples has been successfully applied in ultrasound imaging. Given that a sensitivity of as low as -120 dB had been achieved in OLCR, optical power as low as an order of femtowatt reflected from a sample was able to be detected. However, until 1991 nobody had tried to employ a biological tissue as a sample in OLCR and to form a 2-dimensional image with the backscattered or reflected light from a biological sample.

In 1986 Fujimoto *et al.* demonstrated a new technique to investigate the microstructure of biological systems [Fujimoto 1986]. This technique was based on nonlinear cross-correlation using femtosecond laser pulses. A beam splitter was employed to direct a portion of the 65-femtosecond pulses on a biological sample and a delay line. The light beam traveling through the variable delay line reached to an angle-phase-matched KDP second-harmonic crystal. Reflected and backscattered pulses from the sample also arrived to the KDP crystal, but through a different path. Reference and sample light beams were cross-correlated at the KDP crystal. Fujimoto *et al.* suggested that the spatial resolution of the system was $\sim 15 \mu\text{m}$ which was equal to the full-width at half-maximum (FWHM) of the cross-correlation traces. Using this technique Fujimoto *et al.* observed the cross-correlation signal of light beams reflected and backscattered from the eye of a rabbit and human skin with the reference beam. Moreover, they measured the thickness of the cornea of the rabbit eye. We should note that the intensities of the light beams not their amplitudes were cross-correlated in this technique.

The idea of cross-correlating reflected or backscattered light beams were also applied by a group of researchers in Austria. Fercher *et al.* measured the optical eye length of several human beings using a Fabry-Perot interferometer illuminated by a semiconductor laser with relatively short coherence length [Fercher 1988]. They observed the Newton's interference fringes from the eye. The principle was based on sending two superimposed light beams one of which was delayed by the Fabry-Perot interferometer by two times the separation of its reflective plates. Interference fringes were visible with an infrared-scope if the delay introduced by the interferometer were compensated by the optical eye length of the subject with an uncertainty of source coherence length. Fercher *et al.* measured the eye length of several human beings optically with their interferometric system and acoustically by the ultrasonic technique and compared the results which demonstrated a small difference in the order of 0.1 mm.

In early 1991 a group of researchers in MIT led by James Fujimoto reported their work for the distance measurements in the anterior eye [Huang 1991b]. A modified Michelson interferometer illuminated by a broadband light source was employed. The experimental system was similar to the one demonstrated by Youngquist *et al.* [Youngquist 1987]. The interference signal was recorded by a detector followed by lock-in amplifier as a function of the reference mirror position which was placed on a translating stage with a stepper motor. Basically, Huang *et al.* successfully used the optical coherence domain reflectometry technique to measure corneal thickness, corneal excision depth and anterior chamber depth of the eye with a spatial resolution of 10 μm .

In late 1991 an article was published in *Science* with the title of “Optical Coherence Tomography” [Huang 1991a]. For the first time 2-dimensional cross-sectional images of internal structures in biological samples were demonstrated. In this work, the low-coherence interferometer or reflectometer was extended to form tomographical images of biological tissues. The system was a fiber-based Michelson interferometer built using single mode fiber and one 50/50 fiber coupler. The source was a superluminescent diode. The axial or depth scanning of the sample was performed with a mirror mounted on a translating stage. Similarly, the lateral position of the beam focused to the sample was translated laterally after each depth scan. The group of researchers headed by James Fujimoto demonstrated 2-dimensional OCT images of human retina and human coronary artery with an axial resolution of 17 μm . It was reported that the system could detect reflected power as low as 10 fW with ~ 95 dB dynamic range. Huang *et al.* opened a new field in biomedical optical imaging with their work in 1991 and added the term “Optical coherence tomography” to the literature.

2.3 Advancements in OCT

The results reported by Huang *et al.* in 1991 showed that optical coherence tomography is a promising technique for clinical applications especially in ophthalmology to form tomographic images of human eyes. Clivaz *et al.*, independent from the research group in MIT, reported that they employed an optical low-coherence reflectometer built using a single-mode fiber to study the optical parameters of diffusive biological samples (i.e. fresh artery), such as refractive index and attenuation [Clivaz 1992]. Schmitt *et al.* further investigated measuring optical properties of

biological tissues using a low-coherence reflectometer [Schmitt 1993]. Schmitt *et al.* based their studies on first-order scattering theory unlike Clivaz *et al.* who studied Fresnel reflections from biological samples. Later, Tearney *et al.* employed OCT to determine the refractive index of highly scattering human tissue by measuring the optical path length in the tissue or tracking the focal length shift in tissue moving along the optics axis [Tearney 1995]. Furthermore, Kholodynkh *et al.* precisely measured the backscattering and scattering coefficient of tissue, such as skin, using OCT suppressing the speckle noise in the system [Kholodynkh 2003].

In a classical OCT system the sample arm light beam is focused on the sample with a low numerical aperture lens. The low numerical aperture lens provides a relatively large field of view in the sample which is longer than the coherence length of the source. When a high numerical aperture focusing element is employed in the sample arm, OCT is called optical coherence microscopy (OCM) [Izatt 1994, 1996, Yadlowski 1995]. High numerical aperture focuser provides a relatively small field of view in the sample. However, high numerical aperture focusing improves the transverse or lateral resolution on the sample compared to low numerical aperture focusing. In OCM different scanning methods, such as focus tracking, were implemented to compensate the defocusing of backreflected or scattered light due to the small field of view of the focusing element [Schmitt 1997a]. In focus tracking the focal point in the sample is scanned into depth along with the reference arm scanner.

There have been several different depth scanning mechanisms implemented for OCT imaging. The most common scanning mechanism is a linear translational stage with a DC or a stepper

motor. A mirror or retroreflector is mounted on the stage. Translating the stage along the optic axis allows collection of backscattered or reflected light from the inner structure of the sample given that the interference of the beams is observed only if the optical path length difference between the arms is less than or equal to the source coherence length. Increasing the speed of scanning has been one of the main investigations since motion artifacts cause severe artifacts and loss of information in OCT images of living biological systems. An alternative scanning mechanism was implemented by Tearney *et al.* for OCT [Tearney 1996]. Single-mode fiber in the reference arm was wrapped around a cylindrical piezoelectric transducer which stretched the fiber and thus increased the optical path length when a voltage applied with a speed (~600 Hz repetition rate) about two orders of magnitude more than former scanning methods. Another depth-scan mechanism was implemented again by Tearney *et al.* [Tearney 1997a]. This technique was based on a well-known property of Fourier transform, i.e. a linear phase ramp in the frequency domain corresponds to a time delay in the time domain and is analogous to the femtosecond pulse shaping technique presented by Weiner *et al.* [Weiner 1988]. The reference beam is dispersed with a diffraction grating and imaged on an oscillating galvomirror where the phase ramp is introduced to its Fourier transform. This mechanism is called rapid-scanning optical delay line (RSOD) and was previously implemented by Kwong *et al.* for femtosecond time-resolved signal averaging measurements and for rapid autocorrelators to measure the pulsewidth [Kwong 1993]. Later, video-rate (32 frames/second) OCT was accomplished by Rollins *et al.* employing an RSOD with a scan repetition rate of 4-kHz [Rollins 1998]. The delay and dispersion characteristics of the RSOD have recently been detailed by Zvyagin *et al.* [Zvyagin 2003]. A different scanning mechanism was also realized by Szydlo *et al.* by rotating a

cube before the reference mirror with an air bearing turbine at 28.6-kHz scan repetition rate [Szydlo 1998]. This scanning system was employed in an optical low-coherence reflectometer.

The sources commonly employed in OCT are superluminescent diodes (SLD) radiating at near infra-red (centered at wavelengths from ~800 nm to ~1550 nm) with a broad bandwidth (~60 nm) and thus a short coherence length (~10 μm). SLDs are laser diodes with anti-reflection coatings on both facets, which prevent them from lasing even at high bias currents, so they solely amplify spontaneous emission in a broad spectrum. Since the spectral bandwidth of the source is related to the axial resolution of the system, several different light sources other than SLDs with larger spectral bandwidth have been proposed to be used in OCT. The improved light sources for OCT provide higher resolution and signal-to-noise ratio (SNR). Bouma *et al.* built and optimized a Kerr-lens mode-locked Ti:Al₂O₃ oscillator emitting around 800 nm with a spectral bandwidth of 145 nm [Bouma 1995]. Later, Bouma *et al.* also implemented a self-phase-modulated Kerr-lens mode-locked Cr:forsterite laser source emitting at 1.28 μm as an alternative OCT light source for high resolution imaging [Bouma 1996]. A Yb-doped high power fiber source was also applied in OCT [Bashkansky 1998a]. This fiber laser was a high power light source emitting at 1.08 μm with a smooth spectral shape. However the spectral bandwidth was relatively narrow. Therefore the axial resolution was relatively poor compared to other light sources used in OCT. Another light source implemented for OCT was a Kerr-lens mode-locked Ti:Sapphire laser with double-chirped mirrors [Drexler 1999]. This femtosecond laser source was emitting sub-two-cycles pulses centered at 800 nm with bandwidths of up to 350 nm. Drexler *et al.* accomplished a depth resolution of as low as 1 μm in tissue. Povazay *et al.* combined a commercial compact sub-

10-fs Ti:Sapphire laser with a photonic crystal fiber and built a light source emitting at 725 nm with a spectral bandwidth of 325 nm [Povazay 2002]. The reported axial resolution of the OCT system implemented with this source was 0.75 μm . Recently, a commercially available broadband light source radiating at around 1300 nm was successfully employed by Bizheva *et al.* for OCT imaging [Bizheva 2003]. This light source consists of pulsed erbium fiber laser in combination of a highly nonlinear fiber which leads to a supercontinuum generation from 1.1 μm up to ~ 2 μm . The drawback of the light source is the instability of the emitted light. Fluctuations in power spectral density (also called power spectrum or PSD) and thus output power cause troubles in OCT imaging. Other light sources applied in OCT are thermal lamps such as tungsten halogen lamps [Fercher 2000, Vabre 2002] and xenon arc lamps [Fercher 2000]. The extremely broad bandwidth of thermal light sources provides about 1 μm resolution. However, the disadvantages of the thermal sources are their low-brightness and thus relatively smaller dynamic range. Table 2.1 summarizes some of the light sources with their properties which have been utilized or have the potential to be utilized in OCT imaging.

The research work on OCT performed since 1991 has been slightly focused on theoretical analysis beside the system improvement. Pan *et al.* established a relation of the interference modulation with path-length-resolved reflectance simulated using a Monte Carlo technique [Pan 1995]. Schmitt *et al.* adapted the extended Huygens-Fresnel formulation of beam propagation in turbulent atmosphere to OCT with the investigation of speckle noise in the images [Schmitt 1997b]. Another theoretical analysis of OCT based on the extended Huygens-Fresnel principle was performed for both single- and multiple scattering in highly scattering tissue [Thrane 2000].

In their model Thrane *et al.* took multiple scattered photons into account together with multiple scattering effects.

Table 2.1 Summary of some of the broadband light sources for OCT imaging

Light Source	Center Wavelength [nm]	Bandwidth [nm]	Power [mW]	Reference
SLD	830	70	12	[Superlum 2005]
	930	100	7.5	
	1300	50	10	
	1500	170	0.15	
Multiplexed SLD	890	155	4	[Ko 2004]
KLM*	~800	145	400	[Bouma 1995]
		800	350	[Drexler 1999]
Cr:forsterite	1300	120	100	[Bouma 1996]
ASE	1565	80	7.72	[Akçay 2003]
Nonlinear fiber	Er-pulsed	1375	470	[Bizheva 2003]
		Nd: Glass	1064	139
Yb-doped fiber	1064	30	40	[Bashkansky 1998a]
PCF**	725	325	27	[Povazay 2002]
Tungsten halogen lamp	887	320	2×10^{-4}	[Fercher 2000]
	840	260		[Vabre 2002]

*KLM: Kerr-lens modelocked, **PCF: Photonic Crystal Fiber

Some other studied subjects in OCT are as follows; detection [Podoleanu 2000], optimal interferometer designs [Rollins 1999], endoscopic applications with OCT [Tearney 1997b,

Feldchtein 1998, Pan 2001], *en-face* imaging [Podoleanu 1999, Sticker 2002], polarization-sensitive OCT [Hee 1992, de Boer 1999, 2002], different medical applications of OCT other than human eye, such as dental [Colston 1998] and dermatology [Welzel 2001], image enhancement with signal processing on the acquired interferometric signal [Kulkarni 1997, Bashkansky 1998b] and on the power spectral density of the light source [Tripathi 2002]. Furthermore, some general review articles about OCT have been published [Fercher 1996, 2002, 2003, Schmitt 1999].

CHAPTER THREE: PRINCIPLES AND THEORY OF OCT

This chapter describes and discusses the principles and theory of OCT based on the fact that an OCT system has the same structure as of a Michelson interferometer. First, we detail the operation of the Michelson interferometer and discuss the impact of the temporal coherence of a light source which illuminates it. Then, the interference of low-coherent (i.e. low-temporal coherent) light sources is explicated. Finally, the formation and properties of an OCT signal, which are crucial toward the quantification of axial resolution, are discussed.

3.1 Michelson Interferometry with Monochromatic Stationary Source

The superposition of two or more light beams at a region in space is called interference. The interference phenomenon of light beams is explained with the wave nature of light, since the intensity at the superposition region is not simply the arithmetic sum of the intensities of the interfering light beams, but it presents variations in time and/or space depending on the phase difference between them.

An interferometer is a device which is utilized to superpose the light beams. We discussed the structure of Michelson interferometer in Chapter 1 and stated that it realizes the interference by splitting the amplitude of a light beam into two different paths, i.e. arms of the interferometer, and by recombining the split beams each of which possess an additional phase accumulated by propagation in the arms of the interferometer.

Figure 3.1 presents the schematic of a common free-space and fiber-optic Michelson interferometer. The light beam from the source is incident on a beam splitter. The beam splitter divides the amplitude of the incident light beam and directs the light to two different paths which we call the reference arm and sample arm of the interferometer. The distance of the mirror in the reference arm and the distance of the mirror or the sample in sample arm from the beam splitter are denoted as l_r and l_s , respectively. When the light source illuminating the interferometer is assumed to be monochromatic, i.e. coherent, the electric fields traveling in the arms of the interferometer represented by E_r and E_s are given by

$$\begin{aligned} E_r(t) &= A_r \cdot \exp\{-i(k \cdot 2l_r - \omega \cdot t)\} \\ E_s(t) &= A_s \cdot \exp\{-i(k \cdot 2l_s - \omega \cdot t)\} , \end{aligned} \quad (3.1)$$

where k is the propagation constant and equals $2\pi n / \lambda$, where λ is the wavelength and n is the refractive index of the medium in which light propagates (n equals 1 for air), and ω is the optical frequency and equals $2\pi c / \lambda$, where c is the speed of light. The factor of 2 in the exponentials of Equation 3.1 denotes the round trip of the light in the arms of the interferometer. A photodetector with a finite integration time detects the superposed light beams and provides the time integrated/averaged intensity which we call interference signal henceforth.

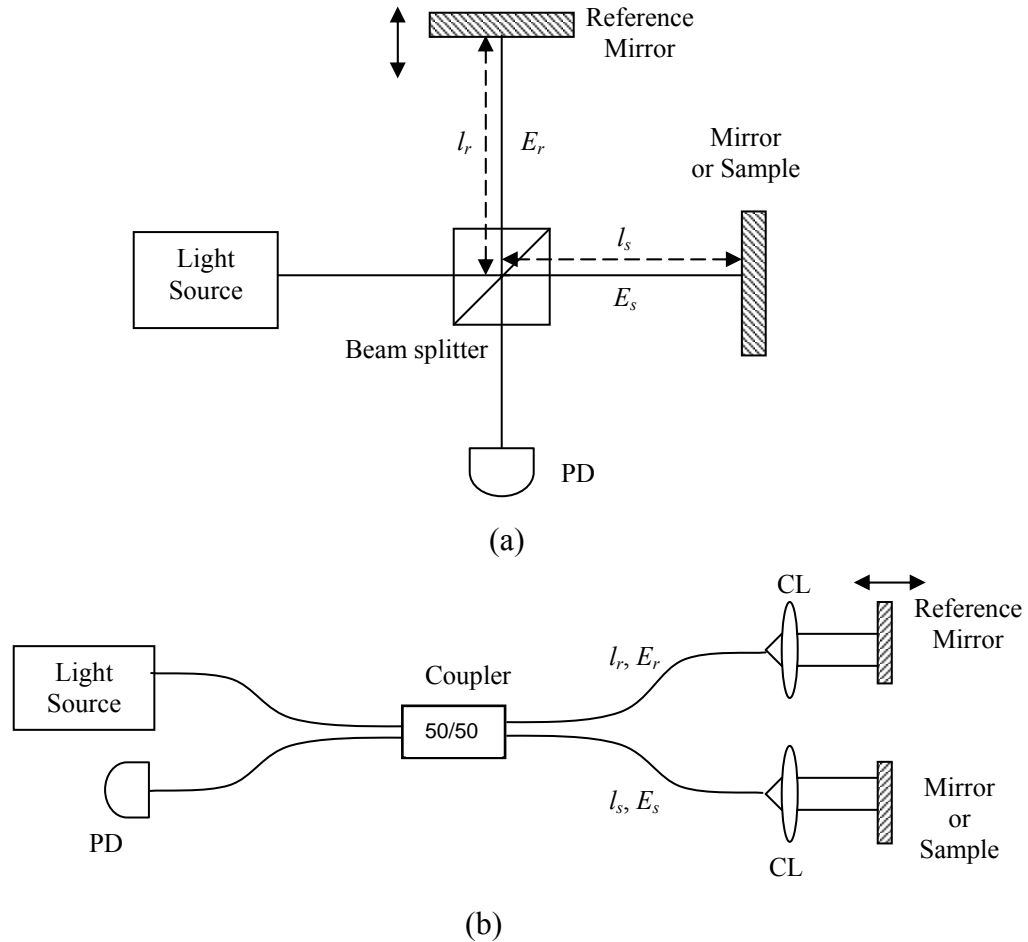


Figure 3.1: Schematic diagram of (a) a free-space and (b) a fiber-optic Michelson interferometer with the electric fields and their propagation distances traveled in the interferometer arms shown. PD: Photodetector, CL: Collimating Lens.

The mathematical description of the interference signal measured by the photodetector of the Michelson interferometer demonstrated in Figure 3.1 can be given by

$$I_d(t, t') = \left\langle \left| \alpha_r E_r(t) + \alpha_s E_s(t') \right|^2 \right\rangle, \quad (3.2)$$

where α_r and α_s are coefficients describing the losses along the interferometer arms including the reflections at the mirror and the sample, the brackets describe the time averaging over the integration time of the detector. If the source field is stationary, then the interference signal $I_d(t, t')$ can be given as a function of τ , i.e. in the form of $I_d(\tau)$, where τ is the difference of the time-of-flight of the light beam between the interferometer arms given by $t - t' = 2(l_r - l_s)/c$. When the sample in the interferometer is a mirror, and the beam splitter divides the amplitude of the light source equally, then A_r and A_s in Equation 3.1 are equal and can be expressed by A which implies that E_r and E_s become equivalent fields and thus Equation 3.2 can be expressed as

$$\begin{aligned}
 I_d(\tau) &= \langle \alpha_r^2 \cdot E_r(t) \cdot E_r^*(t) + \alpha_s^2 \cdot E_s(t-\tau) \cdot E_s^*(t-\tau) + 2 \cdot \alpha_r \cdot \alpha_s \cdot E_r(t) \cdot E_s^*(t-\tau) \rangle \\
 &= (\alpha_r^2 + \alpha_s^2) \Gamma(0) + \alpha_r \cdot \alpha_s \cdot [\Gamma(\tau) + \Gamma^*(\tau)] \\
 &= (\alpha_r^2 + \alpha_s^2) \Gamma(0) + 2\alpha_r \cdot \alpha_s \cdot \text{Re}\{\Gamma(\tau)\},
 \end{aligned} \tag{3.3}$$

where Γ is the autocorrelation of the electric fields and Re is the real part of the complex expression. The time difference τ can be converted to a difference in the distances that the light beams travel in the reference and the sample arms of the interferometer. With this conversion and by using the description of the electric field given in Equation 3.1, Equation 3.3 can be given by

$$I_d(\Delta l) = (\alpha_r^2 + \alpha_s^2) A^2 + 2 \cdot \alpha_r \cdot \alpha_s \cdot A^2 \cdot \text{Re}\{\exp(-i \cdot k \cdot 2\Delta l)\}, \tag{3.4}$$

where Δl is path length difference between interferometer arms which is l_r minus l_s . Equation 3.4 represents an electrical signal which consists of a DC and an AC part. The DC part has a fixed voltage value throughout the measurement, which is also called a DC offset. The AC part is a sinusoid which fluctuates as a function of the phase difference of electric fields propagating different distances in the interferometer arms and thus accumulating different phase. While the DC offset is the arithmetic sum of the intensities of the interfering light beams, the AC part of Equation 3.4 presents the interference phenomenon. Therefore, the DC component of the detected signal does not contain useful information about the interference and usually filtered out electrically.

3.2 Principles of Low-Coherence Interferometry

In Section 3.1 we discussed the interference with a coherent/monochromatic light source. According to Born and Wolf two light beams are coherent if the amplitude and phase fluctuations are completely correlated [Born and Wolf 2002]. Similarly, we describe a coherent light source as a light source which is able to interfere with itself as shown in Equation 3.4 for any phase difference even if one of them propagates an infinite distance and accumulates infinite phase. Therefore, the coherence length of a coherent light source is infinite, where the coherence length is a term used to call the maximum acceptable difference in path length, for example $2(l_r - l_s)$ for the system shown in Figure 3.1a, for which two light beams can still interfere, in which case they are said to be correlated.

In a real physical case no light source can be monochromatic, i.e. it cannot emit at a single wavelength. The power spectral density (power spectrum or PSD) of a monochromatic light source would be expected to consist of a single line at the emission wavelength. However, it is not realistic and even the sharpest spectral line in the PSD of a source has a finite width [Born and Wolf 2002]. If a spectral width is present in the source PSD, then the light source is polychromatic, which means it emits at more than one wavelength. Another physically unrealistic condition is a light source having a PSD with infinite width. In Equation 3.3 we showed that the interference signal is related to the real part of the autocorrelation of the electric fields propagating through the interferometer arms. According to the Wiener-Khintchine theorem, the autocorrelation function and PSD of a light source establish a Fourier Transform pair which is expressed by

$$\Gamma(\tau) \xleftrightarrow{\mathfrak{F}} S(\omega) \quad (3.5)$$

where $S(\omega)$ is the power spectral density in the angular frequency domain, which can also be represented as the wavelength power spectral density $S(\lambda)$, and \mathfrak{F} denotes the Fourier transform operation. Hence, a light source with a PSD of infinite width presents no correlation with itself for any nonzero time-delay τ or difference of path length Δl , which implies that the coherence length of incoherent sources is zero. With an incoherent light source it is physically impossible to observe any fluctuations in the interference signal, which are called fringes, and the intensity of the detected superposed light beams equals the arithmetic sum of the individual intensities of each beam.

Coherent and incoherent light sources are physically non available. All light sources in nature are partially coherent since as stated they always have a finite width PSD. The degree of coherence of a light source is described using its coherence length. The coherence length of partially coherent light sources is neither zero nor infinite. However, some partially coherent light sources may provide an interference signal over large path length differences or time-delays and some of them over relatively shorter path length differences or time-delays. A low-coherent light source is a type of partially coherent light source. It has a relatively short coherence length meaning that the interference signal using for example a Michelson interferometer can be observed only for small differences in path length, i.e. $2\Delta l$ is within the short coherence length of the light source. Fig. 3.2 illustrates the interference with long and short coherence length light sources.

The coherence length of a light source is related to its PSD. From Equation 3.5 we can see that the interference signal for a light source with finite width PSD cannot be expressed as in Equation 3.4 anymore. A mathematical description of the interference signal is to be formulated for light sources with a PSD of finite width considering the Wiener-Khintchine theorem. Thus, we can derive the following mathematical relation between the interference signal and PSD of a light source,

$$I_d(\Delta l) = (\alpha_r^2 + \alpha_s^2) \cdot I + 2 \cdot \alpha_r \cdot \alpha_s \cdot \text{Re} \left\{ \int_{-\infty}^{\infty} S(\lambda) \exp \left(-i \cdot \frac{2\pi}{\lambda} \cdot 2\Delta l \right) d\lambda \right\}, \quad (3.6)$$

where I is the intensity of the light source, the expression with the integral represents the Fourier transform operation, and $S(\lambda)$ is the PSD of the light source which can be measured by an optical

spectrum analyzer (OSA). In Equation 3.6 we see that the AC part of the expression is related to the PSD. From the Fourier transform theory we know that if a function is broad in one domain, then its Fourier transform will be narrow in the transform domain. Then we can deduce that a short coherence length light source should have a broad bandwidth. Meanwhile, we previously stated that the interference signal with a low-coherent light source is observed for a small Δl only that has a maximum limit of the source coherence length. The relation between Δl and bandwidth of PSD will be discussed and quantified in detail in Chapter 4.

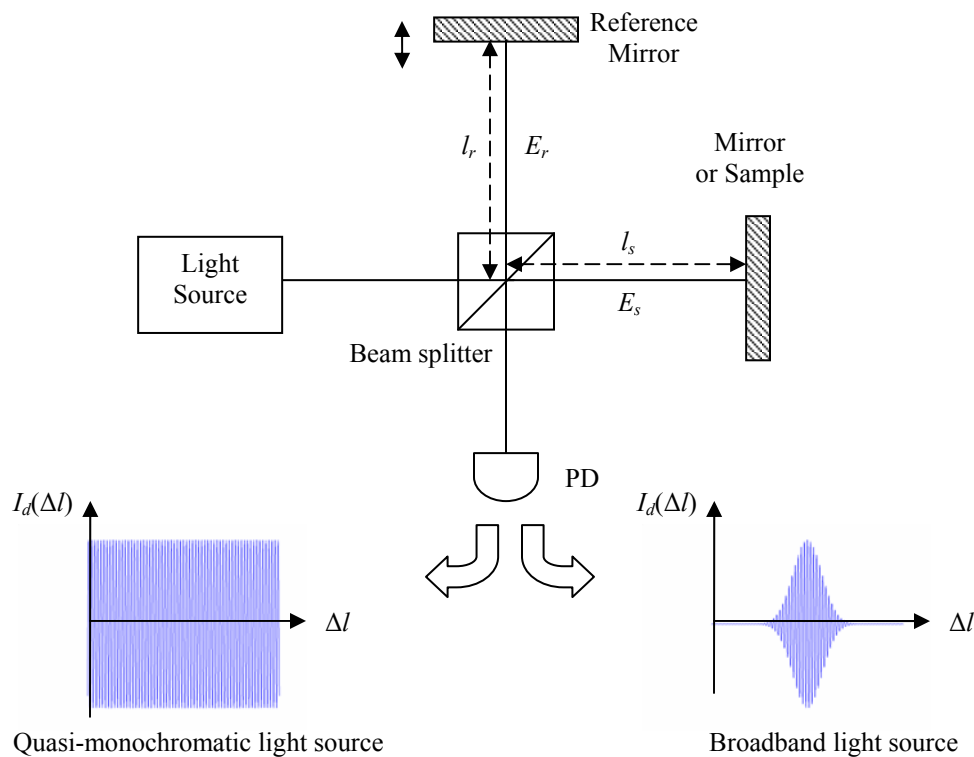


Figure 3.2. Illustration of the interference phenomenon with a long coherence length (quasi-monochromatic) and a short coherence length (broadband) light sources.

Let us assume that the DC offset of the interference signal detected by the photodetector is filtered out after photodetection using a high pass or band pass filter. So, the remaining AC part of the signal is given by

$$I_{AC}(\Delta l) = K \cdot \text{Re} \left\{ \int_{-\infty}^{\infty} S(\lambda) \exp \left(-i \cdot \frac{2\pi}{\lambda} \cdot 2\Delta l \right) \cdot d\lambda \right\}, \quad (3.7)$$

where K is a constant equal to $2\alpha_r\alpha_s$. Performing a Taylor Series expansion about the center wavelength λ_o of the PSD for the phase term in the exponential, Equation 3.7 becomes

$$I_{AC}(\Delta l) = K \cdot \text{Re} \left\{ \int_{-\infty}^{\infty} S(\lambda) \exp \left[-i \left(\frac{2\pi}{\lambda_o} - \frac{2\pi}{\lambda_o^2} (\lambda - \lambda_o) + \frac{2\pi}{\lambda_o^3} (\lambda - \lambda_o)^2 + \dots \right) \cdot 2\Delta l \right] \cdot d\lambda \right\}. \quad (3.8)$$

Since the higher order terms in the expansion are small compared to the lower order terms we can neglect the higher order terms in Equation 3.7 and express it as

$$I_{AC}(\Delta l) \cong K \cdot \text{Re} \left\{ \int_{-\infty}^{\infty} S(\lambda) \exp \left[-i \left(\frac{2\pi}{\lambda_o} - \frac{2\pi}{\lambda_o^2} (\lambda - \lambda_o) \right) \cdot 2\Delta l \right] \cdot d\lambda \right\}. \quad (3.9)$$

When the path length of the interferometer reference arm l_r is varied in time for example by moving the reference mirror with a translational stage, a rate of change for Δl is provided. If the speed of the translational stage is given by v_m and t is the time duration of path length change, then Δl is given by $v_m \cdot t$ and Equation 3.9 becomes

$$I_{AC}(t) \cong K \cdot \text{Re} \left\{ \exp \left[-i \frac{2\pi}{\lambda_o} 2v_m t \right] \cdot \int_{-\infty}^{\infty} S(\lambda) \exp \left[i \frac{2\pi}{\lambda_o^2} (\lambda - \lambda_o) \cdot 2v_m t \right] \cdot d\lambda \right\} . \quad (3.10)$$

In Equation 3.10 there is a phase term outside the integral operation which is related to the rate of change of Δl , i.e. v_m , and the center wavelength of the source PSD. This term represents a phase modulation in the electrical signal generated by the photodetector. The phase modulation in this case is due to the Doppler shift caused by scanning the reference arm path length with a translational stage moving at a constant speed. Because of the Doppler shift the center electrical frequency of the signal f_o is shifted in the electrical frequency domain by the amount given by

$$f_o = \frac{2v_m}{\lambda_o} . \quad (3.11)$$

The phase modulation with the Doppler shift provides optical heterodyning and demodulation of the heterodyne signal after the photodetection increases the signal-to-noise ratio (SNR) of the detected signal. The demodulation, i.e. envelope detection, process is detailed in Chapter 6.

Equation 3.10 presents a basic expression for the photodetector response of a low-coherence interferometer based on the wavelength PSD of the light source. Converting the wavelength to optical frequency ω we also can express the photodetector response as a function of optical frequency whichever is convenient. We present a more detailed mathematical framework in Section 3.3 which presents the OCT signal considering more features than the source PSD and the rate of change in the reference arm path length reference. Indeed we shall see that it is an

approach to the derivation of the interference signal which accounts for statistical features in the source field and the photodetection.

3.3 OCT Signal

We stated in Section 3.2 that an essential component of a low-coherence interferometer is to have a broadband and thus a short coherence length light source. A light source with a broad spectral bandwidth emits an electric field which consists of multiple plane waves at different optical frequencies in the spectral band of the source PSD propagating as a wave package. Indeed, the Fourier transform of the plane waves describes the emitted source electric field vector $\mathbf{E}_{so}(t)$ which is given by

$$\mathbf{E}_{so}(t) = \int_{-\infty}^{\infty} \exp(i\omega t) \hat{\mathbf{E}}_{so}(\omega) d\omega , \quad (3.12)$$

where the caret (^) denotes a Fourier domain function and all variables in boldface denote either a vector or a matrix. The amplitude of the electric field emitted by the light source is split at the beam splitter and directed into the reference and the sample arms of the interferometer. We can describe the losses due to the beam splitter, the absorption in the interferometer arms, non-equal reflections from the reference mirror and the sample mirror or a sample as a frequency-dependent function by $\hat{\alpha}_r(\omega)$ in the reference arm and $\hat{\alpha}_s(\omega)$ in the sample arm. So, the expression for the electric field at the photodetector which presents the electric fields unified at

the beam splitter after propagating in the reference and sample arms of the interferometer can be given by

$$\mathbf{E}(t) = \int_{-\infty}^{\infty} \{ \hat{\alpha}_r(\omega) \exp[i\phi_r(\omega, t) + i\omega t] + \hat{\alpha}_s(\omega) \exp[i\phi_s(\omega, t) + i\omega t] \} \hat{\mathbf{E}}_{so}(\omega) d\omega, \quad (3.13)$$

where $\phi_r(\omega)$ and $\phi_s(\omega)$ are the phases accumulated through propagation in the reference and sample arms of the interferometer, respectively. For the sake of simplicity in future mathematical descriptions we define

$$m(\omega, t) = \hat{\alpha}_r(\omega) \exp[i\phi_r(\omega, t)] + \hat{\alpha}_s(\omega) \exp[i\phi_s(\omega, t)] \quad . \quad (3.14)$$

Therefore, Equation 3.13 will be expressed as

$$\mathbf{E}(t) = \int_{-\infty}^{\infty} m(\omega, t) \exp(i\omega t) \hat{\mathbf{E}}_{so}(\omega) d\omega \quad . \quad (3.15)$$

$\mathbf{E}(t)$ and $\hat{\mathbf{E}}_{so}(\omega)$ are stochastic processes. When the PSD of the light source possess a broad spectral bandwidth, the electric field emitted $\mathbf{E}_{so}(t)$ obeys circular Gaussian statistics, which implies that $\langle \mathbf{E}_{so}(t) \rangle$ equals zero [Goodman 1985, Rolland 2005], where $\langle * \rangle$ denotes the ensemble average or statistical average. Similarly, from Equation 3.13 we infer that the ensemble average of $\mathbf{E}(t)$ equals zero as well.

The electric field $E(t)$ arriving at the photodetector induces a photocurrent which can be expressed as

$$I(t) = \frac{e}{\Delta t} \int_{t-\Delta t}^t N(t') dt' , \quad (3.16)$$

where $N(t)$ is the number of photoelectrons created, Δt is the integration time of the detector, and e is the electron charge (1.6×10^{-19} Coulombs). If we define a time window $r(t)$ with a duration equal to the integration time of the detector, Equation 3.16 becomes

$$I(t) = \frac{e}{\Delta t} \int_{-\infty}^{\infty} r(t-t') N(t') dt' , \quad (3.17)$$

where $r(t)$ is defined as

$$r(t) = \begin{cases} 1, & \text{for } 0 \leq t \leq \Delta t \\ 0, & \text{otherwise} \end{cases} . \quad (3.18)$$

It is well known that the photocurrent generation is a Poisson process resulting from the random arrival of photons at the detector. Therefore, the time-varying number of photoelectrons $N(t)$ can be referred to as a doubly stochastic Poisson process [Barrett 2004]. Given that there are two sources of randomness in our system which are the Poisson process associated with the detection and the Gaussian process associated with the source electric field, in order to obtain mean photocurrent, $N(t)$ is to be statistically averaged over each process as given by

$$\langle\langle N(t) \rangle\rangle = \langle\bar{N}(t)\rangle = \rho \langle \mathbf{E}^\dagger(t) \mathbf{E}(t) \rangle, \quad (3.19)$$

where ρ is given by

$$\rho = \frac{R \cdot A}{e \cdot \eta_o}, \quad (3.20)$$

where R is the responsivity of the detector, A is the area of the detector, and η_o is the impedance of free space which equals 377 Ohms. In Equation 3.19, we first get the conditional mean of $N(t)$ over the Poisson statistics denoted as $\langle * \rangle$ or $\bar{*}$, and then average it over the Gaussian statistics.

Plugging Equation 3.19 to Equation 3.17 we obtain the mean photocurrent at the detector as

$$\begin{aligned} \langle\langle I(t) \rangle\rangle &= \left\langle \left\langle \frac{e}{\Delta t} \int_{-\infty}^{\infty} r(t-t') N(t') dt' \right\rangle \right\rangle \\ &= \frac{e}{\Delta t} \int_{-\infty}^{\infty} r(t-t') \langle\langle N(t') \rangle\rangle dt' . \end{aligned} \quad (3.21)$$

Using the description of $\mathbf{E}(t)$ given in Equation 3.15 and adopting the description of $\langle\langle N(t) \rangle\rangle$ given in Equation 3.19 we can rewrite the expression of the mean photocurrent as

$$\begin{aligned} \langle\langle I(t) \rangle\rangle &= \frac{e\rho}{\Delta t} \int_{-\infty}^{\infty} \int_{-\infty}^{\infty} \int_{-\infty}^{\infty} r(t-t') [m^*(\omega, t) m(\omega', t) \exp(i(\omega' - \omega)t)] \\ &\quad \cdot \langle \hat{\mathbf{E}}_{so}^\dagger(\omega) \hat{\mathbf{E}}_{so}(\omega') \rangle d\omega d\omega' dt' \end{aligned} \quad (3.22)$$

where $\langle \hat{\mathbf{E}}_{so}^\dagger(\omega) \hat{\mathbf{E}}_{so}(\omega') \rangle$ can be described as

$$\langle \hat{\mathbf{E}}_{\text{so}}^\dagger(\omega) \hat{\mathbf{E}}_{\text{so}}(\omega') \rangle = \frac{1}{4\pi^2} \int_{-\infty}^{\infty} \int_{-\infty}^{\infty} \exp[i(\omega't - \omega t')] \langle \hat{\mathbf{E}}_{\text{so}}^\dagger(t') \hat{\mathbf{E}}_{\text{so}}(t) \rangle dt' dt. \quad (3.23)$$

Assuming the source electric field is stationary, the expression $\langle \hat{\mathbf{E}}_{\text{so}}^\dagger(t') \hat{\mathbf{E}}_{\text{so}}(t) \rangle$ represents the scalar autocovariance function of the source electric field which will be denoted by $G(t-t')$.

The Fourier transform of the scalar autocovariance function $\hat{G}(\omega)$ gives us the PSD of the light source denoted by $S(\omega)$. Hence, we can relate Equation 3.23 to the PSD of the light source

$$\begin{aligned} \langle \hat{\mathbf{E}}_{\text{so}}^\dagger(\omega) \hat{\mathbf{E}}_{\text{so}}(\omega') \rangle &= \frac{1}{4\pi^2} \int_{-\infty}^{\infty} \int_{-\infty}^{\infty} \exp[i(\omega't - \omega t')] G(t-t') dt' dt \\ &= \frac{1}{2\pi} \delta(\omega' - \omega) \int_{-\infty}^{\infty} \exp\left[i \frac{\omega + \omega'}{2} (t-t')\right] G(t-t') d(t-t') \quad (3.24) \\ &= \delta(\omega' - \omega) S(\omega) \end{aligned}$$

Now, taking the last expression in Equation 3.24 and using it in Equation 3.22 we can obtain the definition of the mean photocurrent in relation to the source PSD as

$$\langle \langle I(t) \rangle \rangle = \frac{e\rho}{\Delta t} \int_{-\infty}^{\infty} r(t-t') \left[\int_{-\infty}^{\infty} |m(\omega, t)|^2 S(\omega) d\omega \right] dt' \quad (3.25)$$

If the detector integration time is assumed to be instantaneous, which means $r(t-t') = \delta(t-t')$,

then Equation 3.25 becomes

$$\langle \langle I(t) \rangle \rangle = \frac{e\rho}{\Delta t} \int_{-\infty}^{\infty} |m(\omega, t)|^2 S(\omega) d\omega \quad (3.26)$$

Let us assume that α_r and α_s are constants rather than frequency-dependent functions. When we multiply $m(\omega, t)$ defined in Equation 3.14 with its complex conjugate and obtain $|m(\omega, t)|^2$ and then plug it to Equation 3.26 we obtain the mean photocurrent as

$$\langle\langle I(t) \rangle\rangle = \frac{e\rho}{\Delta t} \left\{ [\alpha_r^2 + \alpha_s^2] \int_{-\infty}^{\infty} S(\omega) d\omega + 2\alpha_r \alpha_s \int_{-\infty}^{\infty} S(\omega) \cos[\phi_r(\omega, t) - \phi_s(\omega, t)] d\omega \right\}, \quad (3.27)$$

where $\int_{-\infty}^{\infty} S(\omega) d\omega$ is the intensity of the light. Equation 3.27 presents the mean photocurrent as the response of an instantaneous detector under the assumption that system losses are independent of the optical frequency. The phase accumulated for example with the propagation of the light in the reference arm is defined as

$$\phi_r(\omega, t) = \frac{\omega}{c} 2l_r = \frac{2\pi}{\lambda} 2l_r, \quad (3.28)$$

where l_r is related to time as shown in Equation 3.9 to 3.10.

Equations 3.6 and 3.27 can be used to model the mean photocurrent. We should note that a detector with an instantaneous response and a system with flat loss at all source frequency or wavelength is physically not available. However, such assumptions are legitimate in simulations to reduce the complexity of the simulation process including coding and runtime.

3.4 Discussion

In this Section we present and discuss simulation results based on the mathematical framework derived in Section 3.2 and 3.3. To simulate a single scan OCT signal we first assume that the sample in the sample arm is a mirror with 100% reflectivity over all source wavelength or optical frequency and there is no wavelength-dependent loss thus no dispersion in the system. The missing information to simulate the detector response is the PSD of the light source. Therefore, we first need to generate a PSD. In Chapter 1 we discussed that in biophotonics the best spectral region for light-tissue interaction is the diagnostics and therapeutic window which is from 600 nm to 1300 nm along with spectral characteristics of light sources suitable for OCT imaging demonstrated in Table 2.1.

In Figure 3.3 we present a computer generated source power spectrum centered at 950 nm with a spectral bandwidth of 50 nm. The PSD is chosen to be a Gaussian function of wavelength which is a common practice in simulations associated with broadband optical light sources [Schmitt 1997b, Bruno 2003] under the assumption that the commercially available light sources such as SLDs produce near-Gaussian power spectra. The accuracy of such assumption shall be discussed later. The expression used for the interference signal is given by Equation 3.7, as well as 3.27. Figure 3.4 presents the AC response of the detector, i.e. interference signal, as a function of reference mirror displacement where for example a displacement of zero means that the optical path length of the reference and sample arms are equal. The simulated interference signal is associated with its envelope demonstrated by a dashed line. In the simulation we observe a modulated signal. The modulation happens as the optical path length of the reference arm is

changed at a constant rate, i.e. certain distance per time for example 1 mm/second. A carrier signal is a sinusoid with a carrier frequency given by Equation 3.11. Its period in terms of the reference mirror displacement is always half the center wavelength λ_0 regardless of the rate of change in the optical path length of the reference arm. This outcome can be deduced from Equation 3.10 where at each instance when the mirror displacement $v_m t$ equals $\lambda_0/2$, the phase of the signal changes by 2π .

In the detection process the interference signal will be demodulated so that the envelope of the signal will be extracted, as the carrier signal does not include useful information but just shifts the electrical frequency of the signal into other frequency ranges where there is less noise [Haykin 1994].

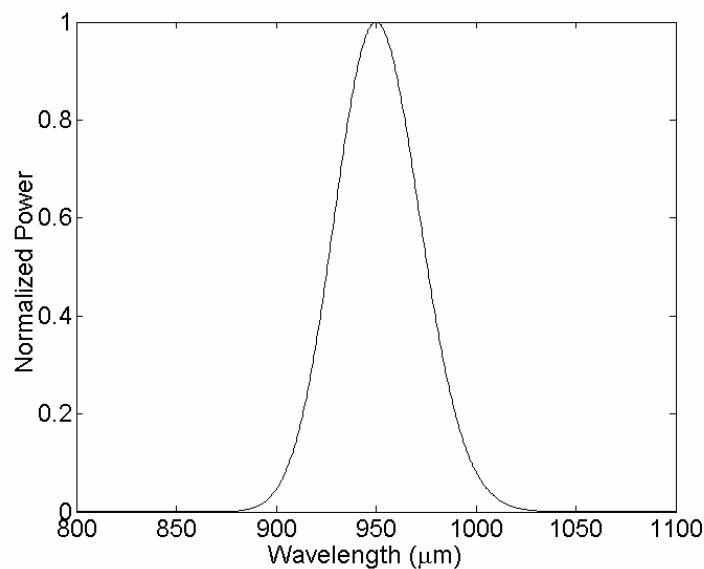


Figure 3.3: A computer generated PSD which represents a virtual broadband light source

In Figure 3.5(a) we demonstrate only the envelope of the interference signal, i.e. demodulated interference signal, in linear scale and in Figure 3.5(b) in logarithmic scale. The plot in logarithmic scale gives us an idea about the dynamic range of the envelope. Given that the Fourier transform of a Gaussian function is also a Gaussian and the interference signal is the modulated Fourier transform of the source PSD as given by Equation 3.10, we expect the envelope function to be Gaussian. We see in Figure 3.5(b) that the Gaussian envelope presents a high dynamic range and fast dropoff as the reference mirror displacement departs from the zero position. Indeed, a Gaussian PSD leading to Gaussian envelope with such features is the main reason for the desire to employ light sources having a Gaussian PSD in OCT imaging.

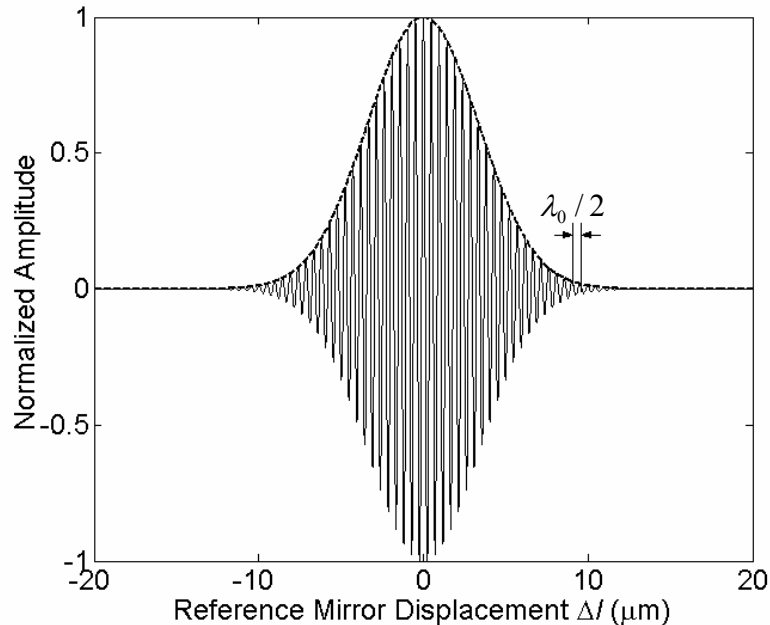


Figure 3.4: The interference signal simulated under ideal conditions according to the PSD shown in Figure 3.3. The dashed line is the envelope of the signal.

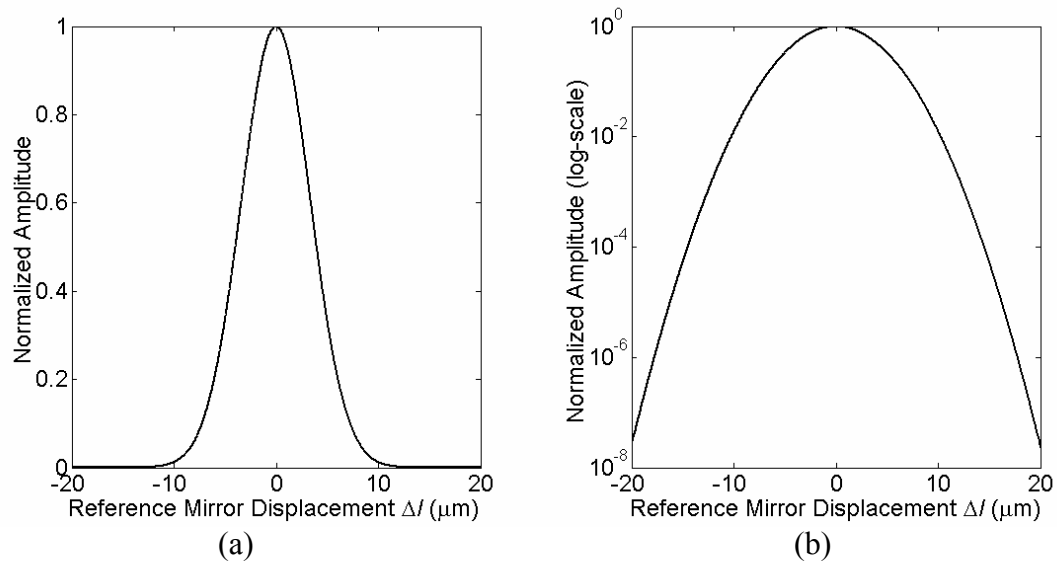


Figure 3.5: Interference signal after demodulation, i.e. the envelope of the interference signal (a) in linear scale, (b) in logarithmic scale.

CHAPTER FOUR: QUANTIFICATION OF RESOLUTION IN OCT

In this Chapter we discuss resolution in OCT and source parameters influencing it. The discussion is based on that an OCT system has an axial or longitudinal resolution giving the resolution along the path of depth-scanning that is related to the spectral characteristics of the light source employed in the system, and a lateral or transversal resolution that is related to the optics focusing sample arm light beam onto the sample. After briefly describing the lateral resolution, we discuss the main topic, i.e. axial resolution, where we propose and analyze different metrics and present the impact of the shape of the source power spectrum on the axial resolution and PSF. Finally, we briefly discuss a novel optimization and performance assessment method for optical coherence imaging based on statistical decision theory.

4.1 Lateral Resolution

In OCT the lateral or transverse resolution is independent of axial resolution unlike in classical microscopy and is determined by the optics which is focusing the sample arm beam onto the sample regardless of the coherence length of the source. By definition the diameter of the focused beam defines the lateral resolution.

Focusing optics with low NA is commonly employed in OCT because they have a relatively large Rayleigh range and thus provide longer depth of focus. The depth of focus is required to be at least as large as the scanning range in the sample which is usually <3 mm for highly scattering

tissue. Low NA optics ensures sufficiently large depth focus however at the expense of a larger spot size thus worse lateral resolution. On the other hand high NA lenses has smaller F/# and thus provide smaller spot size than low NA lens at the expense of short depth of focus that often does not stretch along for example a 3 mm scanning range in a turbid sample.

For high NA applications a dynamic focus tracking which moves the position of the spot size in the sample along the scanning direction is required for depth, i.e. axial, imaging [Schmitt 1997c, Qi 2004]. However, high NA focusing may be employed for high-resolution *en-face* or parallel OCT imaging where the sample is scanned in 2-dimensions laterally [Izatt 1996] rather than axially, i.e. in-depth. A common term used for an OCT system which occupies a high NA optics to focus the light beam onto the sample is optical coherence microscopy (OCM) [Izatt 1994, Aguirre 2003]. In the literature we see that up to 0.8-NA microscope objectives have been used for OCM imaging [Clark 2004], while an OCT system usually employs ~ 0.20 -NA focusing optics [Izatt 1996, Bizheva 2003].

4.2 Metrics for Axial Resolution

In OCT the coherence length sets the temporal width of the interferometric OCT signal formed by the low-coherence interferometer, and consequently sets an upper bound on the axial resolution of the imaging system.

The power spectrum (or PSD) of the source, which is fully characterized by its shape, its spectral bandwidth, and its center wavelength, is of a critical importance for the ability to resolve small structures in optical coherence imaging as it sets the base of coherence length computing. In optical coherence imaging, the coherence length appears in the detected signal through the self-coherence function which is regarded as the axial point spread function (PSF) of the imaging system [Goodman 1985]. Here, we investigate the PSF based on the spectral characteristics of the source.

There are various metrics for the measurement or estimation of the coherence length that is the product of the speed of light c with the coherence time τ_c from the PSF which extracts a measure about its width. For example, we can measure the full-width at half-maximum (FWHM), the width at e^{-1} of the maximum, and the equivalent width of the PSF where each metric is separately used to quantify the width of a function [Bracewell 1965]. The coherence length defined as the full width at half maximum (FWHM) of the PSF has been most extensively used to predict axial resolution in optical coherence imaging while for an estimation of the coherence length, thus axial resolution, the spectral shape of a source is usually assumed to be Gaussian. Nevertheless, the power spectra of real sources are typically non Gaussian. The advantage of such an assumption is that a mathematical expression can be used for the estimation of the coherence length. Such a mathematical expression employs the numerical values of the bandwidth and the center wavelength of the source PSD to obtain a numerical estimation of the coherence length or coherence time (one leading to another) instead of recording or simulating the PSF and measuring its width or computing its coherence length and time from the PSF.

4.2.1 Computing the Coherence Length

The self-coherence function, which is also called the autocorrelation function, of a light source is the PSF of the OCT system when the light beams reaching the photodetector are identical which occurs when the specimen in the sample arm is a high reflective mirror, and when there is no dispersion, no wavelength-dependent loss, and the source PSD remains unchanged throughout the system. This assumption is more realistic for free-space OCT given that air unlike optical fiber does not induce any dispersion on the light beam propagating in the interferometer.

Under the described conditions the self-coherence function of the light source becomes the inverse Fourier transform of the source PSD as given by Equation 3.5 (i.e. $\Gamma(\tau) = \mathfrak{F}^{-1}\{S(\lambda)\}$, where $\Gamma(\tau)$ is the self-coherence function). The normalized self-coherence function provides the complex temporal coherence function of the source that is given by $\gamma(\tau) = \Gamma(\tau)/\Gamma(0)$.

A first, most commonly employed metric for the coherence length is the FWHM of the PSF that is the modulus of the complex temporal coherence function $|\gamma(\tau)|$

$$l_{c.FWHM} = c(\tau' - \tau'') = c \cdot \tau_{FWHM} \quad , \quad (4.1)$$

where $|\gamma(\tau')| = |\gamma(\tau'')| = |\gamma(0)|/2$. Another metric for the coherence length is that defined as the product of the speed of light c and the coherence time τ_c given by [Goodman 1985, Mandel and Wolf 1995]

$$l_{c.ASI} = c \cdot \int_{-\infty}^{\infty} |\gamma(\tau)|^2 d\tau \quad , \quad (4.2)$$

where the absolute-square-integral (ASI) of the complex temporal coherence function is defined as the coherence time. We also used the root-mean-square (RMS) width of the temporal coherence function as a metric for axial resolution [Akcaay 2003]. The RMS-Width (RMSW) l_{σ} of the complex temporal coherence function is given by

$$l_{\sigma} = c\tau_{\sigma} = c \cdot \sqrt{\frac{\int_{-\infty}^{\infty} (\tau - \mu)^2 \gamma(\tau) d\tau}{\int_{-\infty}^{\infty} \gamma(\tau) d\tau}} \quad , \quad (4.3)$$

where μ is the mean of $\gamma(\tau)$ and is given by

$$\mu = \int_{-\infty}^{\infty} \tau \gamma(\tau) d\tau / \int_{-\infty}^{\infty} \gamma(\tau) d\tau \quad . \quad (4.4)$$

4.2.2 Coherence Length and Resolution

A general definition of longitudinal resolution accepted in optical coherence imaging is half the coherence length of the source given that light performs a return trip in the arms of the interferometer [Fercher 1996, Zhang 2001a]. The choice of the FWHM of $|\gamma(\tau)|$, i.e. PSF, for coherence length, most commonly chosen as previously mentioned, is historical in nature and derived from the Rayleigh resolution criterion, which states that two equally bright point sources

are barely resolved when the first zero of the Airy disc of the image of one point, which is the spatial PSF of the imaging system for a circular aperture, is at the center of the Airy disc of the image of the other point. In this configuration, the resulting image intensity at the center corresponds to 73.5% of the intensity at the peaks [Goodman 1985]. It is important to note that the shape of the PSF is critical to the value of the composed image intensity at the center. Therefore, a criterion derived for Airy disks shaped PSFs may not necessarily apply generally to other shaped functions.

If we return to fundamentals, the longitudinal resolution of an optical coherence imaging system is the minimum longitudinal separation detectable in two successive distinct locations (or layers) in the specimen that is illustrated in Figure 4.1 with different optical characteristics such as varying refractive index, where backreflections occur. To formulate the signal detected while scanning the specimen model shown in Figure 4.1 we can use Equation 3.27 and present the OCT signal as

$$\begin{aligned} \langle\langle I(t) \rangle\rangle = \frac{e\rho}{\Delta t} \left\{ \left[\alpha_r^2 + \alpha_s^2 \right] \int_{-\infty}^{\infty} S(\omega) d\omega \right. \\ \left. + 2\alpha_r\alpha_s \left\{ \int_{-\infty}^{\infty} S(\omega) \left(\cos\left[\frac{\omega}{c} 2(l_r(t) - l_s) \right] + \cos\left[\frac{\omega}{c} 2(l_r(t) - l_s - \Delta z) \right] \right) d\omega \right\} \right\}, \quad (4.5) \end{aligned}$$

where $l_r(t)$ indicates that the reference arm path length is scanned. The first and second cosine term presents the interference of the reference arm field with the field E_1 and E_2 in Figure 4.1, respectively. While the variable τ in previous Equations represents the difference of time-of-flight of the light beams in the reference and sample arms of the interferometer setup which is

associated with the speed of light and is called time delay in the dissertation, the variable t represents the measurement time which is associated with the scanning speed of the reference arm. Filtering out the DC term in Equation 4.5, the information-bearing AC term is given by

$$\langle\langle I(t) \rangle\rangle_{AC} = \frac{e\rho}{\Delta t} 2\alpha_r\alpha_s \left\{ \int_{-\infty}^{\infty} S(\omega) \left(\cos\left[\frac{\omega}{c} 2(l_r(t) - l_s)\right] + \cos\left[\frac{\omega}{c} 2(l_r(t) - l_s - \Delta z)\right] \right) d\omega \right\}. \quad (4.6)$$

In establishing an upper bound for axial resolution, we shall assume that the displacement between two layers Δz is an integer multiple of the center wavelength of the source in the material of propagation. Hence, the temporal coherence functions are assumed to be in phase. In this case, the envelope of the detected signal is proportional to the summation of the modulus of the two temporal coherence functions with a time delay in between them. If a phase mismatch exists, the resulting signal will also depend on the phase of the complex temporal coherence functions. The assumption of phase matching leads to the worst result in terms of resolution. However we use this assumption in order to be able to compare the metrics

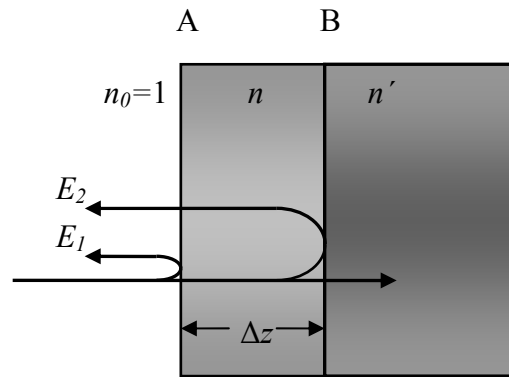


Figure 4.1: A specimen model with two layers to determine the axial resolution. Δz is the separation between the two layers n and n' are the refractive indices.

4.3 Simulation Results

4.3.1 *Real PSD versus ideal PSD*

Light sources employed in optical coherence imaging systems have usually PSDs $S(\lambda)$ approximated to a Gaussian function in order to estimate the axial resolution [Fercher 1996, Izatt 1996, Hitzenberger 1999, Bouma 1995 and Pan 1995]. Several groups have carried out experimental assessments showing a good agreement between the self-coherence width predicted from the source spectrum and the measured PSF [Wang 1999, Hitzenberger 1999, Bouma 1995]. The two last examples, which employ a superluminescent diode and a Ti:Al₂O₃ laser, respectively, underline the need of taking into account the fact that the sources were not Gaussian to evaluate the coherence length. In order to present the impact of the source PSD on the coherence length, we first consider two general mathematically defined PSDs which are Gaussian and Lorentzian. Later, we compare the Gaussian and Lorentzian PSDs to a real source PSD all having the same spectral bandwidth and the same center wavelength.

A general expression for a normalized Gaussian PSD (i.e. $\int S(\lambda)d\lambda = 1$) and its inverse Fourier transform, $\Gamma(\tau)$ is given by

$$S(\lambda) = \frac{2\sqrt{\ln 2}}{\sqrt{\pi} \cdot \Delta\lambda} \exp \left[- \left(\frac{2\sqrt{\ln 2} \left(\frac{1}{\lambda} - \frac{1}{\lambda_0} \right)}{\left(\frac{\Delta\lambda}{\lambda_0^2} \right)} \right)^2 \right], \quad (4.7)$$

$$\Gamma(\tau) = \exp\left[-\left(\frac{\pi \cdot c \Delta\lambda \cdot \tau}{\lambda_o^2 \cdot 2\sqrt{\ln 2}}\right)^2\right] \cdot \exp\left[-i \cdot \left(\frac{2\pi c \tau}{\lambda_o}\right)\right], \quad (4.8)$$

where λ_o is the center wavelength and $\Delta\lambda$ is the -3 dB spectral bandwidth. $\Gamma(\tau)$ is by definition normalized to one. If the PSD of the source is a normalized Lorentzian instead of a Gaussian, $S(\lambda)$ and $\Gamma(\tau)$ are given by

$$S_{Lzn}(\lambda) = 2 \left[(\pi \Delta\lambda) \cdot \left(1 + \left(\frac{\left(\frac{1}{\lambda} - \frac{1}{\lambda_o} \right)}{\frac{\Delta\lambda}{\lambda_o^2}} \right)^2 \right) \right]^{-1}, \quad (4.9)$$

$$\Gamma_{Lzn}(\tau) = \exp\left[-\frac{\pi c \Delta\lambda}{\lambda_o^2} |\tau|\right] \cdot \exp\left[-i \cdot \left(\frac{2\pi c \tau}{\lambda_o}\right)\right]. \quad (4.10)$$

An explicit mathematical expression for the coherence length of a light source with a mathematically defined PSD is derivable for each metric discussed in Section 4.1.1. In Table 4.1 we present these expressions which formulate the coherence length of a source with either a Gaussian or a Lorentzian PSD that have temporal coherence functions as given by Equations 4.8 and 4.10.

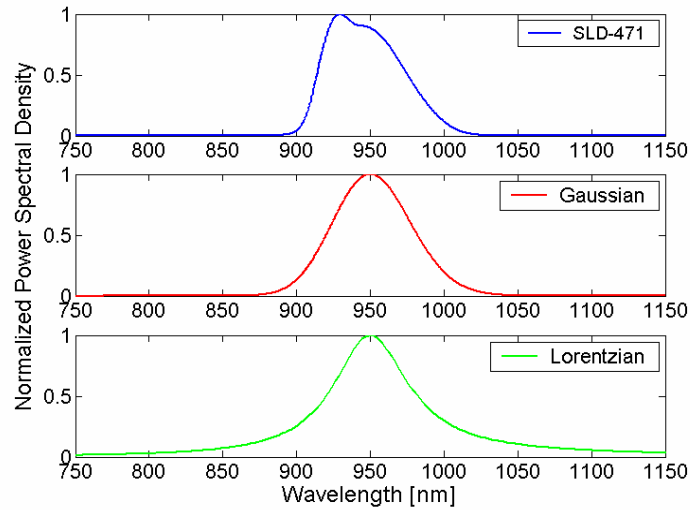
To study the effect of the assumption that a real source has an ideal PSD, where ideal means a Gaussian or Lorentzian, we compare the coherence lengths computed for a real source PSD and equivalent (i.e. same bandwidth and central wavelength) Gaussian and Lorentzian PSDs. The real light source we considered is a superluminescent diode (Superlum Diodes SLD-471). It is a

broadband, low-coherence source centered at 950 nm with a spectral bandwidth of 62 nm. In Fig. 4.2(a) we present the PSD of the real source, as well as the normalized Gaussian and Lorentzian PSDs given by Equations 4.7 and 4.9, where the center wavelength and bandwidth were set to match that of the SLD-471. The presented PSDs are normalized to unity for comparison. Fig. 4.2(b) shows the computed modulus of the complex temporal coherence functions $|\gamma(\tau)|$ corresponding to the PSF of the imaging system associated to each PSD shown in Fig 4.2(a).

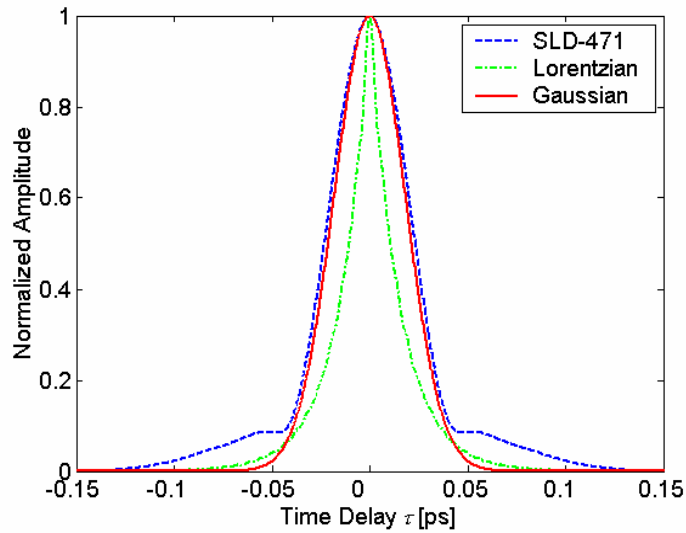
Table 4.1 Coherence length of a Gaussian and Lorentzian PSD formulated for three metrics

PSD	$l_{c.FWHM}$	$l_{c.ASI}$	$l_{c.\sigma}$
Gaussian	$\frac{4 \ln 2}{\pi} \frac{\lambda_o^2}{\Delta \lambda}$	$\sqrt{\frac{2 \ln 2}{\pi}} \cdot \frac{\lambda_o^2}{\Delta \lambda}$	$\frac{\sqrt{2 \ln 2}}{\pi} \cdot \frac{\lambda_o^2}{\Delta \lambda}$
Lorentzian	$\frac{2 \ln(2)}{\pi} \frac{\lambda_o^2}{\Delta \lambda}$	$\frac{\lambda_o^2}{\pi \cdot \Delta \lambda}$	$\frac{\sqrt{2} \cdot \lambda_o^2}{\pi \cdot \Delta \lambda}$

The spectrum analyzer employed to measure the PSD of the SLD-471 provides a discrete data set of 1001 samples (N) with 0.4 nm resolution ($\delta\lambda$). The domain of the time delay τ depends on the center wavelength λ_o and $\delta\lambda$ as $[-\lambda_o^2 / (2c \cdot \delta\lambda), \lambda_o^2 / (2c \cdot \delta\lambda)]$, such that the time delay resolution $\delta\tau$ will be $\lambda_o^2 / ((N-1) \cdot c \cdot \delta\lambda)$ which equals 7.513 femtoseconds. The complex temporal coherence function is estimated using an inverse fast Fourier transform.



(a)



(b)

Figure 4.2: (a) Measured PSD of the SLD-471: the normalized Gaussian PSD and the normalized Lorentzian PSD ($\lambda_o=950$ nm, $\Delta\lambda=62$ nm for each), (b) corresponding PSFs, i.e. modulus of the complex degree of temporal coherence functions.

Table 4.2 presents the computed coherence lengths of the SLD-471 and the two theoretical sources. As shown in Table 4.2, different spectral shapes present different coherence lengths, thus axial resolutions for images recorded by OCT, although they have the same bandwidth and center wavelength. While approximating the PSD of the SLD-471 to a Gaussian function results in an error of about 10% for coherence lengths evaluated through ASI and FWHM metrics, the error increases up to ~40% for RMS-width metric. The results show that the coherence lengths computed from the Lorentzian PSD are about half that of the coherence lengths of the Gaussian PSD and the SLD-471 for ASI and FWHM metrics, however its RMSW is larger than for a Gaussian.

Table 4.2 Coherence length of Sources with different shaped PSDs

Sources	$l_{c.FWHM}$ [μm]	$l_{c.ASI}$ [μm]	$l_{c.\sigma}$ [μm]
SLD-471	14.14	10.78	9.61
Gaussian	12.83	9.65	5.49
Lorentzian	6.42	4.64	6.58

SLD-471, Gaussian, and Lorentzian correspond to the PSDs as presented in Fig. 4.2(a) with the same label, respectively. The metrics used to compute the coherence length are described in Section 4.1.1.

To validate the accuracy of these computations we compared the values for the coherence length of the Gaussian and Lorentzian PSDs obtained from Equations 4.1, 4.2, and 4.3 to those presented in Table 4.1 which relate only the bandwidth and center wavelength of the source PSD to the coherence length for each metric. Numerical computational errors between 0% and 0.7%

occurred between the results obtained from computation with the formulas and from the simulated PSF. These numerical errors, which occurred due to the discrete form of the PSD and the temporal coherence functions, are small enough to neglect.

4.3.2 *Computation of Coherence Lengths of Sources with Extended PSDs*

PSDs of real sources usually include spectral bumps and dips in their shapes, which leads to sidelobes in the interferometric signal. The sidelobes may significantly affect the resolution of the system. However, longitudinal resolution can always be estimated from the measured PSD of the light source following the metrics presented.

The deformation (i.e. dips) of the spectral shape of sources employed in optical coherence imaging is usually observed for high power ($\sim 10^1$ to $\sim 10^2$ mW) broadband sources ($\sim 10^2$ nm), such as the Superlum SLD-47-HP with a Gaussian dip in its spectrum as shown in the specification sheet of the product [Superlum 2005], mode-locked Ti:Al₂O₃ laser sources with multiple dips and bumps in their spectrum [Bouma 1995, Drexler 1999], and the SLD-370 as presented in a partial coherence interferometry experiment [Hitzenberger 1999].

We investigated the effect of a dip in the PSD of virtual sources on the coherence length and associated longitudinal resolution. A Gaussian PSD with 100 nm spectral bandwidth centered at 940 nm was generated with Matlab™. We introduced spectral dips into the Gaussian PSD by subtracting Gaussian functions of 45 nm spectral bandwidth centered at 940 nm and different magnitudes. Each resulting normalized PSD had a 100 nm spectral bandwidth with different

amplitudes of spectral dip. Figure 4.3 shows the Gaussian PSD (red dashed line) and the generated PSDs with spectral dips.

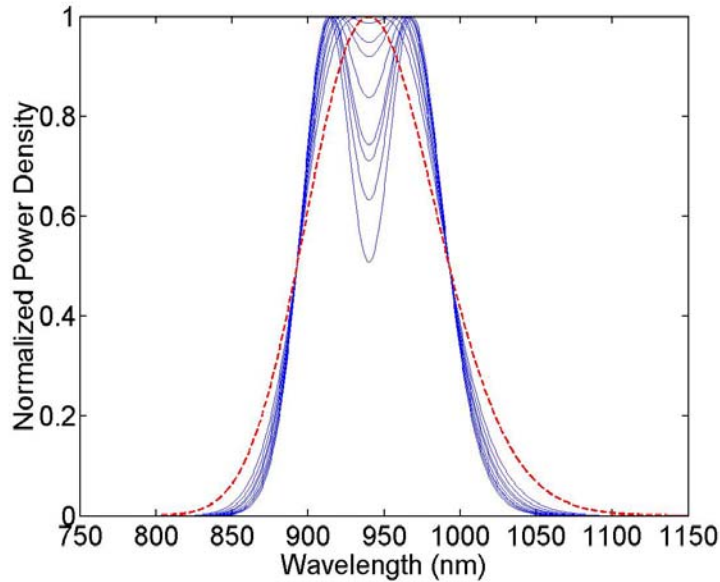


Figure 4.3: A Gaussian PSD with 100 nm -3 dB spectral bandwidth centered at 940 nm (red dashed line) and PSDs of the same bandwidth and center wavelength with different spectral dip amplitudes.

Power spectral analyses of these PSDs were performed. Figure 4.4 presents the plot of the numerical results for the coherence length of each PSD as a function of the percentage of the level difference between the dip minimum (PSD value at the dip) and the peak of the PSD (maximum value which equals one in a normalized PSD), where a zero percentage of spectral dip refers to the Gaussian PSD. In Figure 4.5 the simulated modulus of the temporal coherence functions of the PSDs with 49.13%, 5.1% dip, and Gaussian are presented as examples. Coherence lengths were estimated using three metrics presented in Equations 4.1, 4.2, and 4.3.

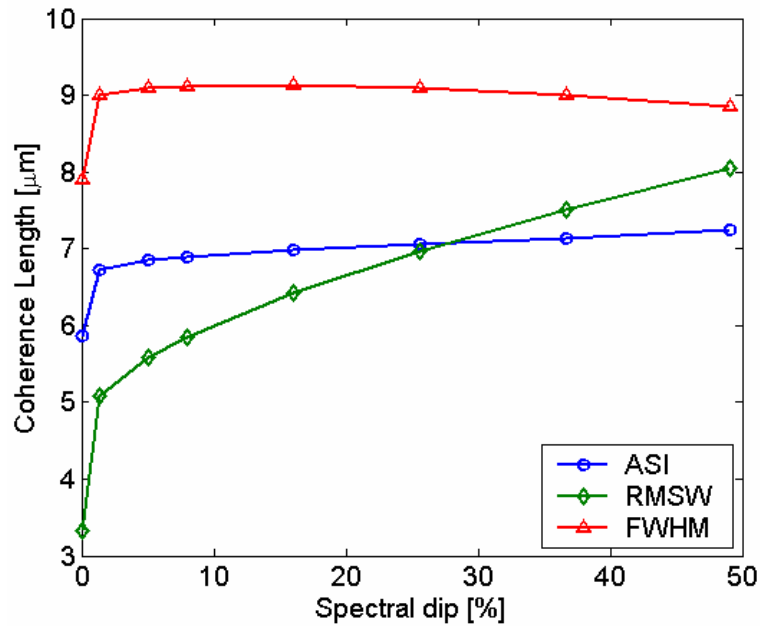


Figure 4.4: The coherence length is presented as a function of the amplitude percentage of the spectral dip in the source PSD computed using the ASI, RMSW and FWHM metrics. 0% dip corresponds to a pure Gaussian PSD, i.e. with no spectral dip.

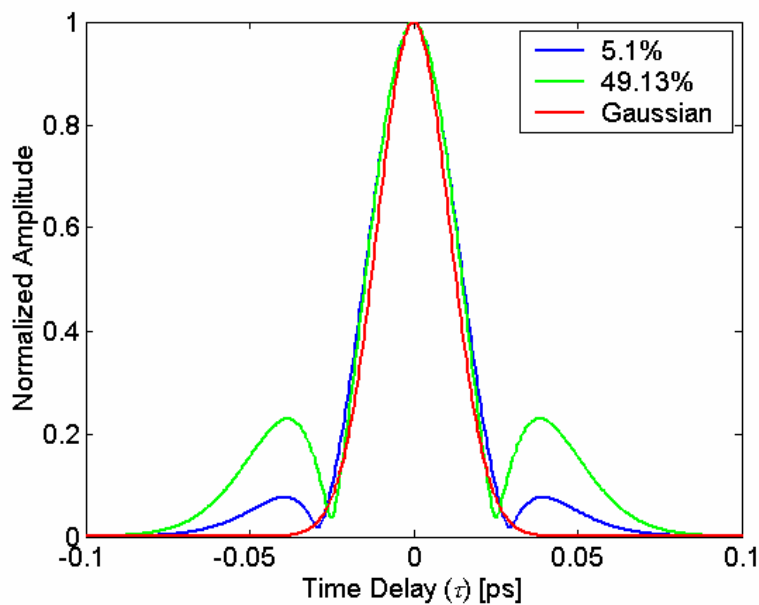
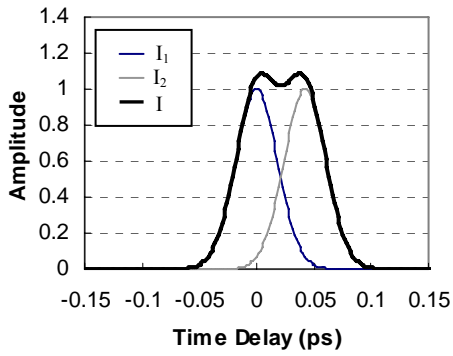


Figure 4.5: $|\gamma(\tau)|$ of the PSDs of the 100 nm bandwidth centered at 940 nm source with selected percentage of spectral dip.

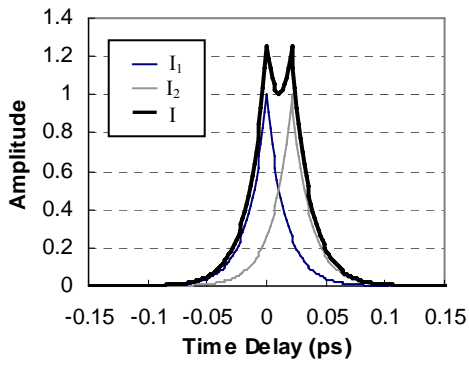
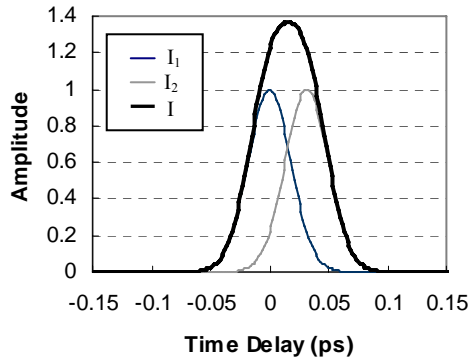
4.3.3 Ability to Resolve Two Layers

We shall predict here the ability to resolve two layers separated by Δz for the selected sources discussed above. Referring to Figure 4.1, we assume as previously detailed that the phases of the complex temporal coherence functions are the same, and the index of refraction n' is chosen such that α_{sm} , given by Equation 4.6, equals one. We set the separation of these layers Δz to half $l_{c.FWHM}$ given by Equation 4.1 or half $l_{c.ASI}$ given by Equation 4.2, both presented in Table 4.2 and Figure 4.4. We first considered the normalized Gaussian, Lorentzian, and SLD-471 PSDs, which were described in Section 4.2.1. The ability to resolve two layers are presented in Figure 4.6(a)-(c), respectively. Then, we employed two of the PSDs, specifically with the 8% and the 49.13% spectral dips, presented in Section 4.2.2. The results are demonstrated in Figure 4.6(d) and 4.6(e).

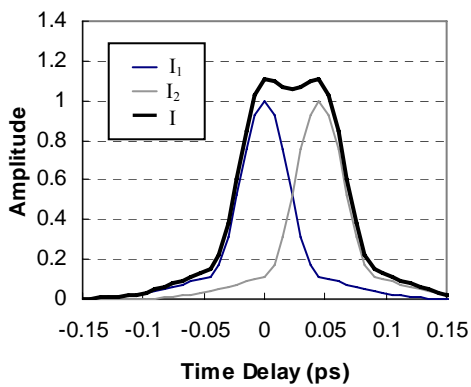
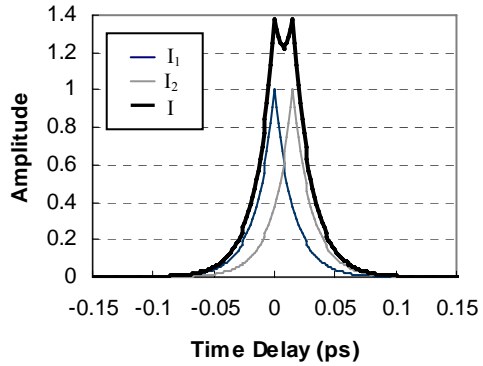
In Figure 4.6 we do not set the layer separation according to the source coherence lengths determined from the RMSW metric because the other two metrics are sufficient to describe the resolution trend given that $l_{c,\sigma}$ has a value either less than $l_{c.ASI}$ or between $l_{c.ASI}$ and $l_{c.FWHM}$ as shown in Table 4.2 and Figure 4.4 except for a slightly larger value in the case with Lorentzian PSD.



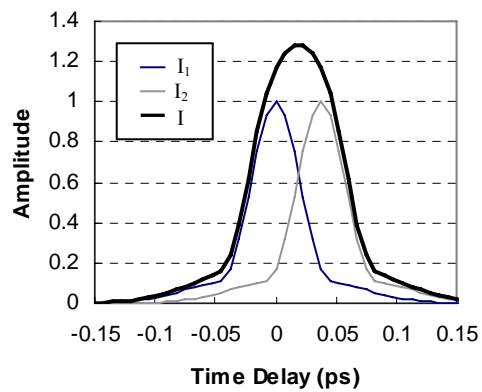
(a)



(b)



(c)



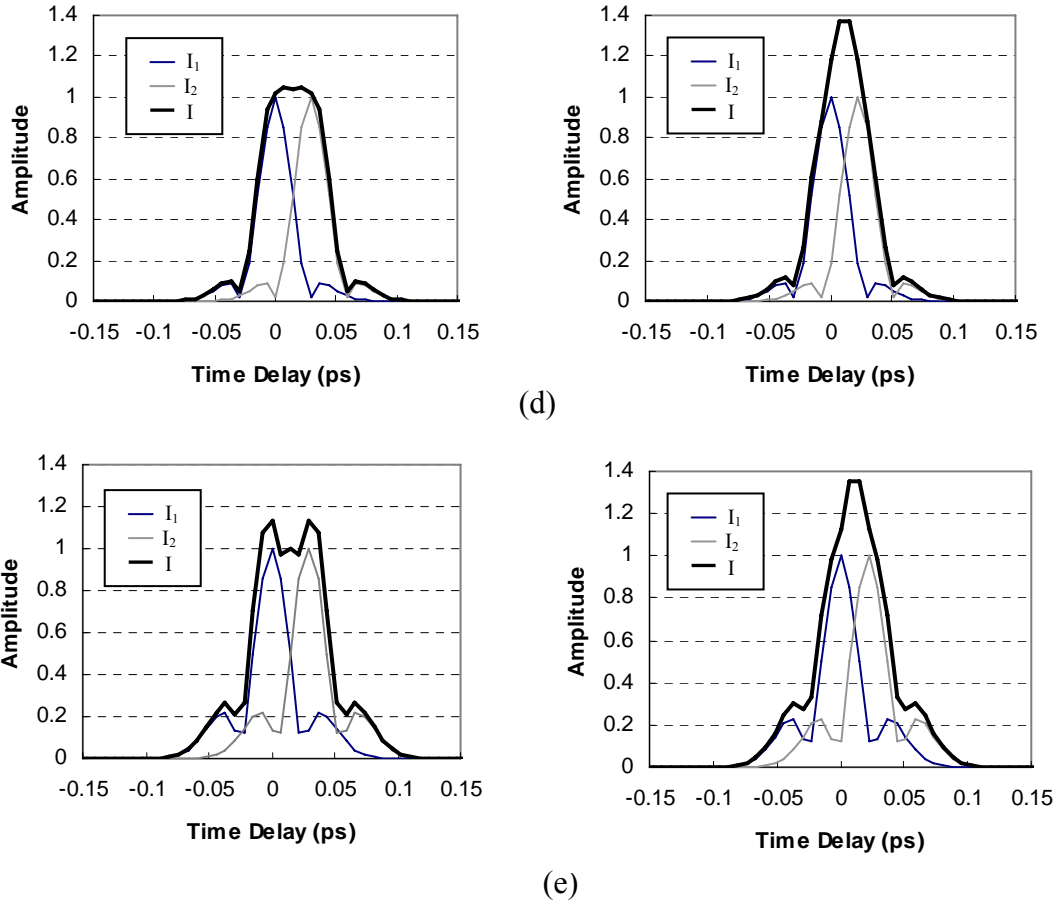


Figure 4.6: Envelopes of the interferometric signals I_1 and I_2 due to backreflections from two successive layers (left column $\Delta z = l_{c.FWHM} / 2$, right column $\Delta z = l_{c.ASI} / 2$, and thus $\Delta \tau = 2\Delta z / c$) and the resulting signal I for a source with (a) Gaussian PSD, (b) Lorentzian PSD, (c) SLD-471 presented in Fig. 4.2(a), and (d) PSD with 8% spectral dip amplitude and (e) PSD with 49.13% spectral dip amplitude presented in Fig. 4.3.

4.3.4 Discussion

Significant differences in computed longitudinal resolution and coherence length for real and theoretical sources with the same bandwidth and center wavelength but with different spectral shapes were presented. Such results demonstrate the importance of taking into account the shape

of the source PSD in predicting axial resolution. A source with a slightly narrower spectral bandwidth than another source could possibly lead to higher resolution than the latter, simply based on its ‘superior’ shape. Such findings are further strengthened by the analysis of coherence lengths from PSDs of same spectral width, yet having varying amplitudes of spectral dips. Results show that approximating a PSD with a spectral dip to a Gaussian PSD of the same center wavelength and bandwidth leads to incorrect values of coherence length obtained using any metrics considered. In Figure 4.4 we see that the source coherence length computed with all metrics increases significantly when there is even a shallow dip in the source PSD compared to the coherence length of a Gaussian PSD with the same spectral characteristics. This outcome indicates that the optimum PSD of a broadband light source to be used in OCT is one which is free of spectral dips. While the spectral bandwidth and the center wavelength is carefully considered as a major parameter which affects the axial resolution in OCT, the spectral shape of the source PSD should not be undervalued.

A spectral dip in a PSD introduces side lobes in the temporal coherence function. When computing the coherence length through the FWHM metric, we measure the FWHM of the main lobe disregarding the side lobes. If the side lobes are located close to the main lobe, the overall FWHM of the temporal coherence function could be larger than the FWHM of the main lobe. When using the ASI and RMSW metric to compute the coherence length, the integration process extends through the main lobe and the side lobes (e.g. Figure 4.5). Integrating the side lobes will result in a larger value of the coherence length and thus worse axial resolution compared to the axial resolution value obtained from a PSF with the same main lobe but no side lobes. However,

if a case occurs where the side lobes are far from the main lobe, the effect on the image will be the presence of ghost images and will not be necessarily a decrease in axial resolution especially according to the FWHM metric.

In the simulations conducted based on the separation of two layers and various PSDs, results show that two layers, with a separation of half the FWHM of the modulus of the temporal coherence function, can not always be resolved depending on the shape of the PSD of the source, as shown in Figure 4.6(d). Also, the half of the coherence length derived through the absolute-square-integration does not provide a detectable separation of the layers except in the case of a source with a Lorentzian PSD. Moreover, the plots in Figure 4.6 indicate that the dip between the two maxima of the resulting signal is not as low as 73.5% of the amplitude of the peak, which is required by the Rayleigh resolution criterion for the PSFs having the shape of the Airy pattern. However, none of the PSFs presented in this Chapter have the shape of the Airy pattern. Given that the PSF of an OCT imaging system may own different shapes depending on the spectral shape of the source PSD, defining a resolution criterion assuming that the PSF has a single shape such as Gaussian is not suitable.

The metrics used and presented are limited in their ability to precisely predict experimental results, given that the refractive index n has to be taken into account in the resolution prediction as shown in Section 4.4 and Section 5.3. Furthermore, the media itself could significantly affect the axial resolution as a result of dispersive effects of the specimen [Lee 2005]. Finally the setup, including the detection scheme, may also be a source of decrease in resolution, given the group

velocity dispersion in the fiber of a fiber-based OCT system, the polarization mismatch between the two arms and unsuitable coating for the optical elements across the entire spectrum of the source, and noise.

Two additional remarks are necessary to end the discussion. The first one concerns the other aspects of the sources that are also important for the quality of optical coherence imaging, such as the dynamic range [Chinn 1993], and the temporal fluctuations [Drexler 1999]. The second one underscores the fact that the axial resolution we have set is not the last limit we could achieve if we take into account image processing. Indeed, knowing the self-coherence function, the noise and some optical properties of the media, appropriate deconvolution operation may lead to improve axial resolution [Kulkarni 1997, Schmitt 1998]. Furthermore, in next Chapter we present an approach to optimize the PSF of the imaging system by suppressing the side lobes via optically shaping the source power spectrum.

4.4 Task-based Metric

We developed a mathematical framework based on task performance that uses statistical decision theory for the optimization and performance assessment of OCT [Rolland 2005]. The development of such framework was motivated by the art of diagnosis in medical imaging, where image quality is estimated based on the performance of an observer on specific tasks [Barrett 1998]. Assessing the image quality provided by an imaging system without a given task and based on the observer's subjective assessment is called subjective assessment. Subjective assessment

provides arguable results as it may change with the system or the observer and it does not fulfill a purpose [Barrett 1990]. Therefore, a definition of task is necessary for objective assessment. The pioneer studies on objective assessment of image quality were conducted by Barrett *et al.* [Myers 1985, Smith 1986]. Two major task categories may be defined: classification and estimation. In our current study we limit our investigation to classification tasks. We define two tasks: a signal-detection task and a resolution task. A signal-detection task is generated to investigate whether the OCT signal can be detected. The purpose of a resolution task is to study whether two interfaces can be resolved with the OCT system [Rolland 2005].

Signal-detection and resolution tasks are binary classification tasks since they consist of only two hypotheses which are the negative hypothesis H_0 and the positive hypothesis H_1 such as signal is present or absent, or the layers can be resolved or not. We have two classes defined for these tasks: the 0th class for the cases when H_0 is true and the 1st class for the cases when H_1 is true. An ideal observer can be employed to perform the task if all statistical information of the data is available to the observer, i.e. a probability density function (PDF) is known under each hypothesis. The ideal observer provides the maximum performance one can get from any observer. When the PDF information is not available, the Hotelling observer [Barrett 2004] is a preferred alternative. The Hotelling observer is a linear discriminant which depends on the second order statistics of the data. In our studies, we employ the Hotelling observer to perform the defined classification tasks which is discussed in-depth in Chapter 5. The Hotelling observer generates a scalar detectability index to discriminate data into a certain class according to negative and positive hypotheses. In a recent paper [Rolland 2005] we proposed to use the

detectability index and area under the receiver operating characteristics curve (AUC) to determine how well an optical coherence imaging system which is considered to be a free-space Michelson interferometer performs a given task. Different types of observer models have been described and discussed in the literature [Myers 1985, Smith 1986, Fiete 1987, Barrett 1990, Rolland 1992, Wollenweber 1999, Barrett 2004, Rolland 2005].

In task-based performance analysis, we investigate the impact of some system parameters such as the source coherence length and/or the spectral shape of the PSD and sample model on the detectability and AUC of the imaging system. While the task-based metric does not provide an exact numerical value for the axial resolution, the AUC curve shows the system performance for a resolution task. We discuss the task-based performance analysis further in Chapter 5 in an application of the task-based assessment method.

CHAPTER FIVE: OPTICAL SPECTRUM SHAPING FOR OPTIMIZATION OF THE PSF IN OCT

In this Chapter we introduce a novel method to improve the PSF of the OCT imaging system. The method is based on shaping the power spectrum of the broadband light source illuminating an OCT system with a technology based digital micromirror device. The technology presented is applied to the OCT system at the output of the light source before the interferometer and thus before the data acquisition. We demonstrate optimization of the axial PSF obtained from an ASE light source where the side lobes of the PSF are suppressed by smoothing the shape of the source power spectrum via a programmable spectral processor. We then demonstrate the impact of the spectral shape of broadband light sources in a task-based approach for assessment of signal-detection and resolution in OCT.

5.1 Improved the PSF by Optical Spectral Shaping

In Chapter 4 we demonstrated that the temporal coherence property of the light source or power spectrum governs the axial PSF of the imaging system [Bouma 2002, Akcay 2002], thus the axial resolution. In OCT, light sources having smooth and rather symmetrical power spectra are preferred. Specifically, irregularities in the shape of the power spectrum such as spectral dips lead to side lobes in the axial PSF as shown in Figure 4.5 that cause ghost images and mask weak axial reflections located near a strong reflection for example. Real broadband light sources,

however, especially as the source spectra become broader, often present spectral dips in their power spectra.

Inhibition of the side lobes of spatial PSFs in optical imaging has been previously investigated. For example, Crowe *et al.* [Crowe 1993] proposed a nonlinear digital operator to be applied in the post-processing stage to suppress side lobe effects of the spatial PSF on images obtained through a square aperture. Similarly, digital signal processing and optimization algorithms on the acquired interferometric signal have been previously employed in OCT to increase resolution or to minimize the effect of the PSF sidelobes when the source had either a power spectrum departing from a Gaussian or when several sources were combined to generate a source with larger spectral bandwidth. Bashkansky *et al.* [Bashkansky 1998b] showed how a simple deconvolution can lead to an equivalent reshaping of the spectrum structure of the source resulting in an increase in the axial resolution. However, this method leads to a significant increase of the noise floor. Tripathi *et al.* [Tripathi 2002] later proposed to reduce the side lobes in the axial PSF applying a correction curve on the measured interferometric signal. The authors reported side lobes reduction with a lower increase in noise floor. Zhang *et al.* [Zhang 2001b] demonstrated an optimization algorithm to select the wavelengths and coherence lengths of several LED's which were combined to obtain an axial PSF with a shorter coherence length and reduced side lobes compared to an arbitrary combination of sources. However, except for [Zhang 2001b] all the above described methods are based on post data acquisition signal processing techniques while we present in this Chapter the experimental results demonstrating inhibition of side lobes of the axial PSF in OCT by optical spectral shaping of the source power spectrum

prior to data acquisition. Our research is motivated by the hypothesis that correcting the power spectrum at the source output and thus before data acquisition will be more useful for practical use than as a post-processing correction especially for *in vivo* real-time imaging where there is no extra post-processing time available for correcting the side lobes in the PSF.

For a free-space Michelson interferometer where there are no wavelength-dependent or frequency-dependent losses throughout the interferometer, we can use Equation 3.27 to represent the AC part of the detected interferometric signal that will be given by

$$\langle\langle I(t) \rangle\rangle_{AC} \propto \int_{-\infty}^{\infty} S(\omega) \cos[\phi_r(\omega, t) - \phi_s(\omega, t)] d\omega, \quad (5.1)$$

where $\phi_r(\omega, t)$ and $\phi_s(\omega, t)$ are the phases accumulated through propagation in the reference and the sample arms, respectively. The envelope function of the detected signal defines the axial PSF of the imaging system. While in practice electrical envelope detection circuits and devices such as lock-in amplifiers or RMS voltmeters can be utilized, mathematically we describe the envelope function of a signal through forming an analytical signal representation of the detected signal as

$$s_a(t) = s(t) - iH\{s(t)\}, \quad (5.2)$$

where $s(t)$ is a square-integrable real signal such as given by Equation 5.1 and $H\{*\}$ is Hilbert transform operator where the Hilbert transform of $s(t)$ is given by

$$H\{s(t)\} = \frac{1}{\pi} \int_{-\infty}^{\infty} \frac{s(t')}{t' - t} dt' . \quad (5.3)$$

The absolute value of the complex analytical signal $s_a(t)$ provides the envelope of the real signal $s(t)$ which is given by

$$s_{env}(t) = |s(t) - iH\{s(t)\}| = \sqrt{s(t)^2 + [H\{s(t)\}]^2} . \quad (5.4)$$

By plugging Equation 5.1 into 5.4 we obtain a mathematical description of the PSF of the OCT imaging system given by

$$PSF(t) = \sqrt{\langle\langle I(t) \rangle\rangle_{AC}^2 + [H\{\langle\langle I(t) \rangle\rangle_{AC}\}]^2} . \quad (5.5)$$

The detected photocurrent signal and thus the axial PSF of the OCT imaging system can also be related to the wavelength PSD of the light source that is given by

$$\langle\langle I(t) \rangle\rangle_{AC} \propto \int_{-\infty}^{\infty} S(\lambda) \text{Cos}[\phi_r(\lambda, t) - \phi_s(\lambda, t)] d\lambda , \quad (5.6)$$

In measurements, we often record the axial PSF as a function of the position of the reference arm mirror rather than time where the change in the position of the reference arm mirror is equivalent to the increase in the reference arm optical path length where the reference arm mirror may be scanned with a linear translational stage moving at a constant speed.

In Chapter 4, we discussed the effect of the shape of the source power spectrum on the OCT signal and simulated the axial PSFs for a real superluminescent diode and virtual ideal sources with specific spectral characteristics. Now we propose a new use of a novel programmable spectral processor (PSP; Newport OSP-9100) for OCT instrumentation. For the first time, this component is shown to be applicable to the optical shaping of the power spectrum of a broadband source before data acquisition in OCT imaging. This processor is based on the Texas Instrument DLP™ micromirror technology [Duncan 2003]. The light, which enters the PSP via a single mode fiber, is dispersed across the micromirror array by a diffraction grating, and is then re-imaged into the exit fiber via the grating. The hundreds of thousands of micromirrors in the array act as a reflective spatial light modulator, selectively reflecting portions of the spectrum into the exit single mode fiber, while simultaneously eliminating or reducing portions of the original spectral components causing spectral dips that are not desirable. Figure 5.1 illustrates the process of optical spectral shaping via a digital light processor (DLP) also known as a digital micro mirror device (DMD).

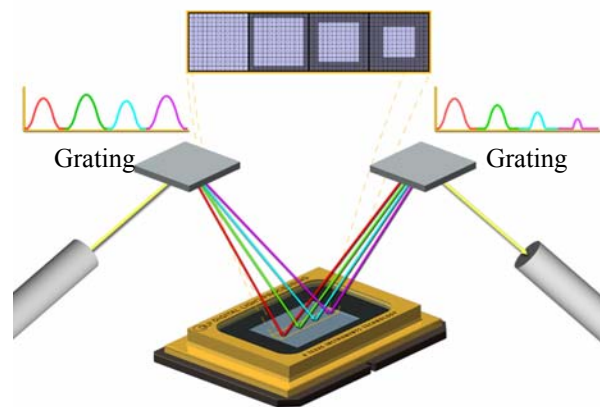


Figure 5.1: Selective attenuation of optical power contained in different wavelength bands via DMD [Duncan 2003].

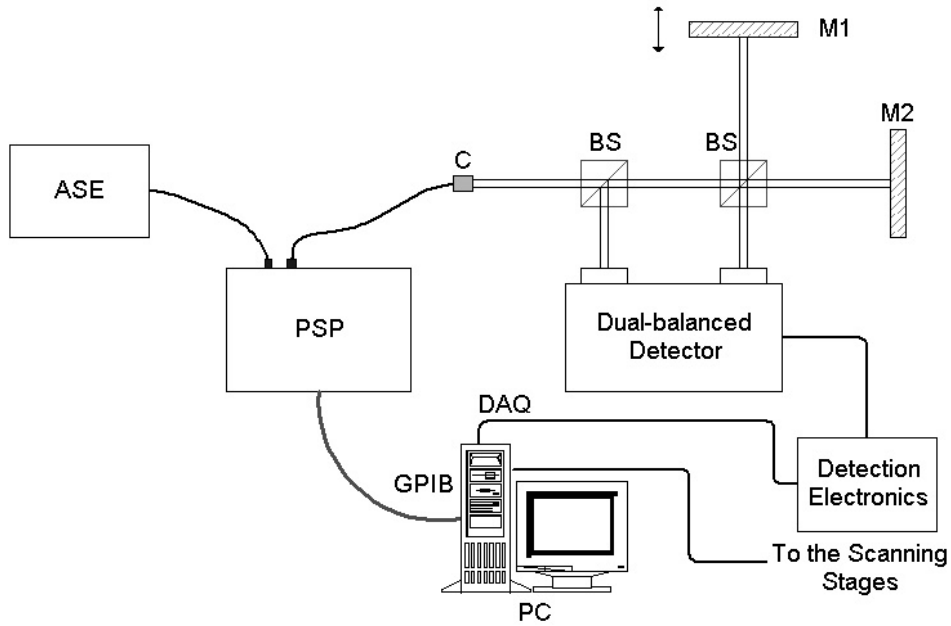


Figure 5.2: Schematic of the experimental setup used for axial PSF measurements: PSP, programmable spectral processor; C, collimator; BS's, beamsplitters; M1, M2, mirrors.

A free space Michelson interferometer depicted in Figure 5.2 was implemented with a balanced photoreceiver (Nirvana 2017-M) to measure the axial PSF before and after optical spectral shaping. A balanced photoreceiver was employed to eliminate intensity noise of the light source. A broadband amplified spontaneous emission (ASE) source (Newport BBS-430) emitting at $1565 \pm 40 \text{ nm}$ was employed during the experiments. This source was selected in this set of experiments given that the PSP operates between 1520 nm and 1620 nm. The PSP was connected to the ASE source through a single mode fiber patch cord. The optical power at the output of the PSP was 7.72 mW while it passed through the PSP without any shaping. A fiber pigtailed collimator delivered the optical power from the output of the PSP to the interferometer. Axial scanning was performed at a speed of 1 mm/s with a linear translational stage. A personal

computer (PC) was used to control the PSP and the translational stages that carry the mirrors and to acquire the data via a DAQ board using LabView (see Appendix B). We employed a digital lock in amplifier (Stanford Research SR-830) to perform envelope detection of the signal modulated by the Doppler shift introduced by the scanning reference arm mirror.

To shape the PSD of the ASE source we first needed to generate a transmission function for the PSP that sets the final shape of the PSD after the spectral shaper. Ideally, a Gaussian power spectrum is desired at the output of PSP. However, the device cannot amplify the optical power in any wavelength band. On the contrary it operates on the principle of power attenuation. Therefore, the purpose in our application is to clean the spectral dips in the source power spectrum so that the source PSD becomes smoother in shape. In order to set a transmission function for the PSP we first measured power spectrum of the ASE source denoted by $S_0(\lambda)$. A broadband Gaussian power spectrum $S_g(\lambda)$, which could fit under the measured power spectrum of the source, was then generated digitally using MatlabTM. The transmission curve $T(\lambda)$ was computed as the ratio of the generated $S_g(\lambda)$ to the original $S_0(\lambda)$ power spectra when $S_0(\lambda)$ was larger than or equal to $S_g(\lambda)$. Otherwise $T(\lambda)$ was assigned zero. Then $T(\lambda)$ was converted to dB-scale and each value was rounded to a single decimal place, because the attenuation resolution of the PSP was 0.1 dB. Figure 5.3 illustrates the generation of the transmission function and the resulting source power spectrum. We see that the shaped power spectrum does not have the spectral dips anymore but it is not an exact truncated Gaussian due to the limited resolution of the PSP.

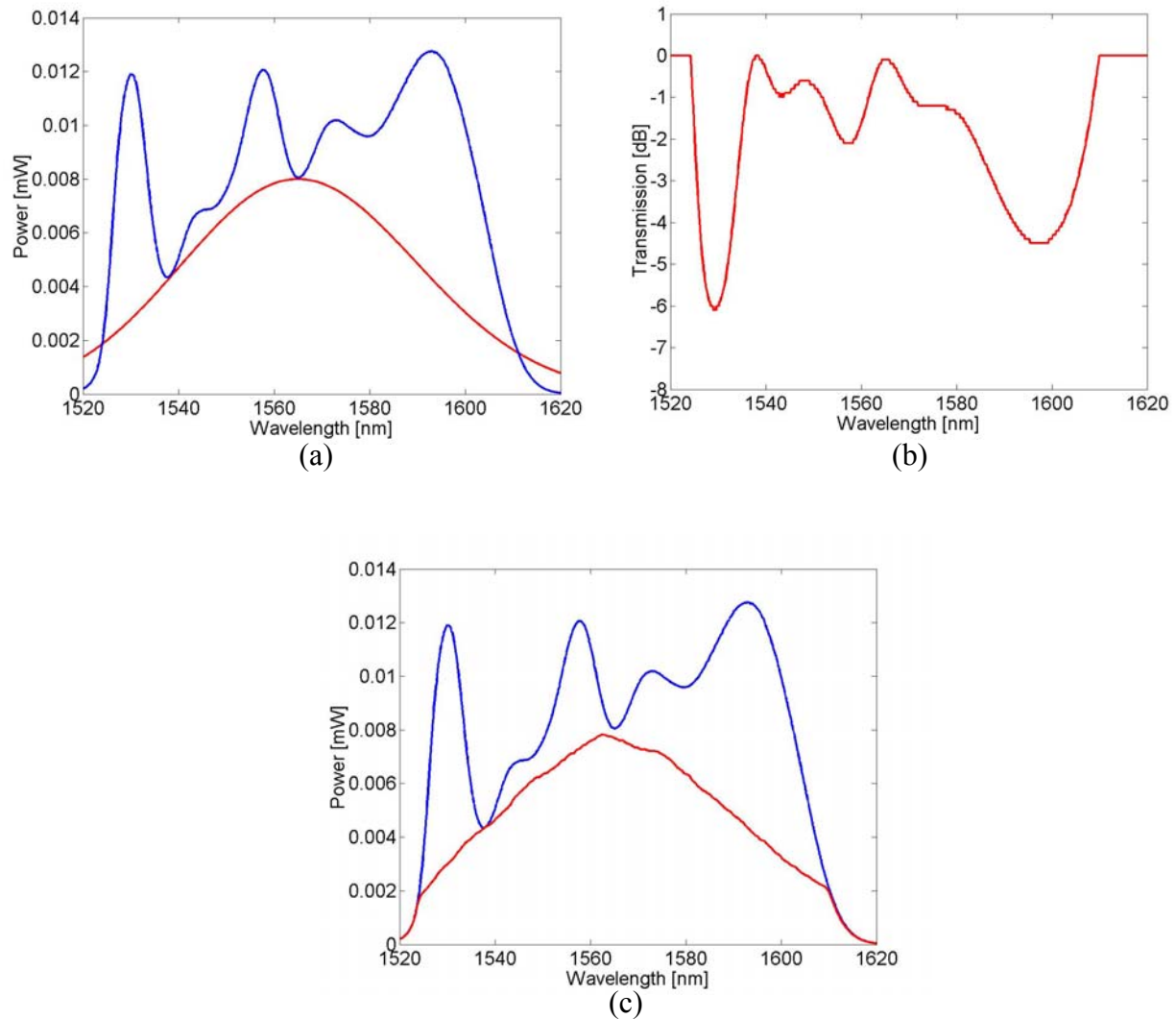


Figure 5.3: (a) The source PSD is the blue curve and underneath it a Gaussian PSD is fitted, (b) the transmission function which is obtained from the ratio of the source and Gaussian PSDs shown in (a) and is then rounded to one decimal place to accommodate 0.1 dB amplitude resolution, (c) the source PSD (blue curve) is presented with the resulting PSD underneath it measured using the transmission curve shown in (b).

Following the same procedure described above a second transmission curve was generated that gives a shaped power spectrum which has a slower transition from the peak region of the power

spectrum toward its tails. Figure 5.4(a) presents the second transmission function denoted T_2 along with the first one described in Figure 5.3 and denoted T_1 both as a function of wavelength. Transmission functions were sent to the PSP via GPIB. The final power spectra shaped by the PSP using transmission functions are presented in Figure 5.4(b) together and denoted S_1 and S_2 , respectively. S_1 , also shown in Figure 5.3(b), which is in linear scale, can be given by $10^{[(S_{0,dB}+T_{1,dB})/10]}$ where the subscript dB indicates that the function is in log-scale. The total power loss after the spectrum shaping was measured to be -2.3 dB, corresponding to a 4.54 mW of output power. When the second transmission function was transferred to the PSP, we obtained a shaped power spectrum S_2 as shown in Figure 5.4(b). For this case, the total power loss was -3.4 dB, corresponding to a 3.53 mW of output power. Figure 5.4(b) presents the original, i.e. unshaped, power spectrum of the ASE source as well.

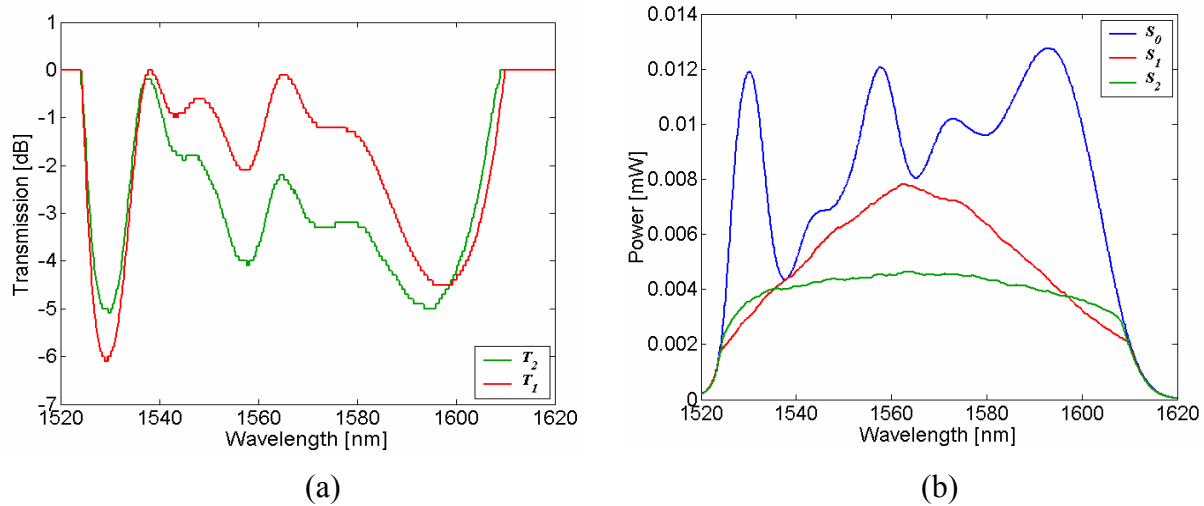


Figure 5.4: (a) The transmission functions to be transferred to the PSP to smooth the shape of the source power spectrum, (b) the power spectra measured with an OSA before and after spectral shaping: S_0 ; unshaped power spectrum, S_1 ; shaped power spectrum obtained with T_1 , and S_2 ; shaped power spectrum obtained with T_2 .

Figure 5.5 shows the axial PSFs corresponding to the original power spectrum as well as the two shaped power spectra shown in Figure 5.4(b). The PSFs were recorded using the experimental setup shown in Figure 5.2. With the first shaping operation, up to 12.9 dB suppression in the side lobes of the axial PSF was obtained as shown in Fig 5.5(a). The noise floor of the axial PSF in the far-field increased by only 2.2 dB. Similarly, with the second spectrum shaping operation up to 7.6 dB suppression in the sidelobes of the axial PSF was obtained as shown in Figure 5.5(b). The log-scale PSFs represent the ten times base-ten-logarithm of the recorded voltage signal that is normalized. The increase of the axial PSF in the far-field was in this case as small as 1.8 dB. In Table 5.1, the associated change in the FWHM, ASI and RMS-width of the axial PSFs of the original spectrum as well as that of the two shaped spectra are reported. The quantities are obtained using the methods described in Chapter 4. While the FWHM metric predicts a small loss in resolution, the two other metrics report either an increase or an insignificant change in axial resolution, further pointing to the need to further investigate experimentally the applied significance of the various resolution metrics.

Figure 5.6 shows side by side an image formed by the original spectrum and that formed by the shaped spectrum. These data are raw data with no averaging to reduce background noise and no image processing applied. Both images are 400 x 400 pixels and represent a 1-mm x 1-mm portion of an onion. The images are log-compressed which means that each axial scan also called A-scan which is acquired at the output of the lock-in amplifier in linear-scale in volts, are converted to log-scale and then normalized to 255 gray levels to form an 8-bit gray level image. Throughout the unshaped spectrum image, spurious structures are clearly visible as a

consequence of the side lobes of the PSF. The spectrally shaped image clearly shows suppression of ghost images.

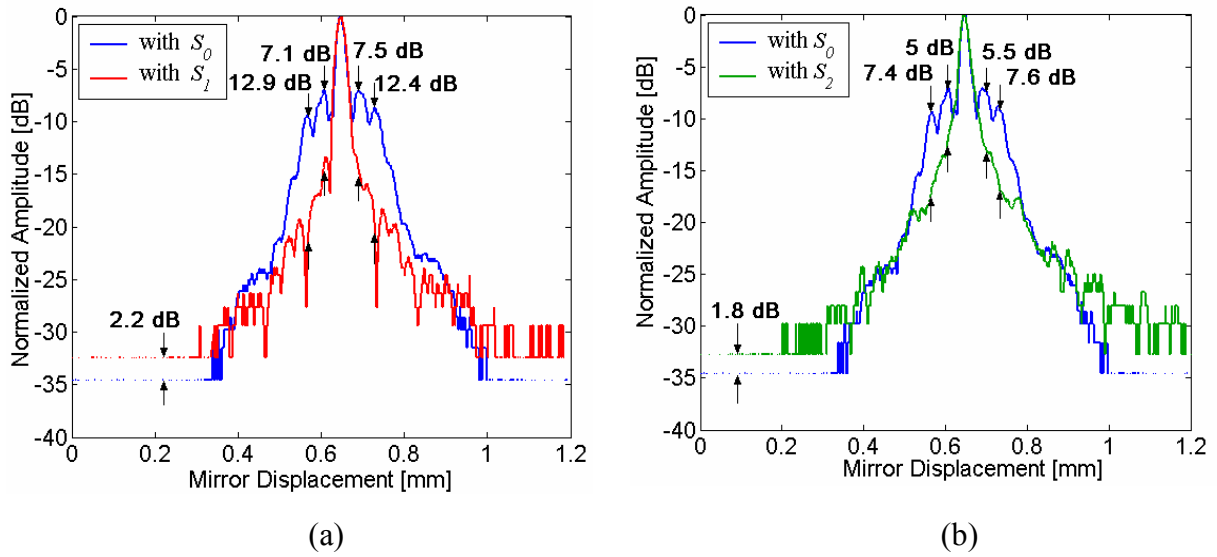


Figure 5.5: The PSFs recorded experimentally. We compare the change in PSF after first spectral shaping operation in (a), and after second one in (b) to the PSF recorded with the unshaped source power spectrum.

Table 5.1 Axial resolution for the differently shaped power spectra computed according to three metrics described in Chapter 4.

Axial PSF from	FWHM [μm]	ASI [μm]	RMS-width [μm]
S_0 (blue curve)	22.3	19.9	19.74
S_1 (red curve)	24.9	19.1	20.05
S_2 (green curve)	24	18.6	20.03

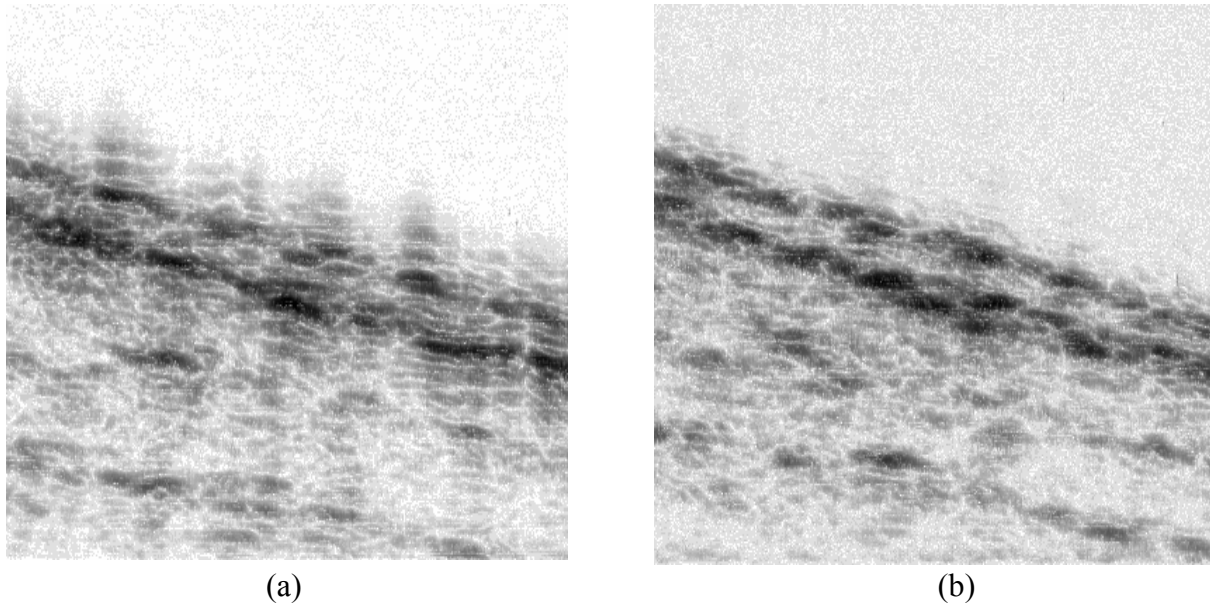


Figure 5.6: Images of onion before (a) and after (b) spectral shaping.

In conclusion, we have investigated the impact of optical spectral shaping of an OCT light source on the axial PSF of the system. The PSP enabled shaping the source power spectrum and inhibition of the side lobes of the axial PSF for two different spectral shapes that were smoother than the original spectrum. Shaping the source power spectrum was shown to be a powerful method for the optimization of the system PSF and suppression of spurious structures in the final image. Furthermore, optical spectral shaping is a real time process and allows hardware optimization for imaging rather than post-data acquisition digital signal processing.

5.2 Possible Extension: Modular Optical Spectral Shaper

In Section 5.1 the unit utilized was operable in a wavelength band from 1520 nm to 1620 nm. A modular optical spectral shaper based on DMD technology can be conceptualized to operate at other common wavelengths for OCT sources which are detailed in Table 2.1. However, in practice the extension is challenging. Figure 5.7 presents a possible schematic of an optical spectral shaper. This structure is similar to that of femtosecond pulse shapers [Weiner 2000]. In this configuration the grating and DMD are one focal length away from a cylindrical lens. The grating that disperses the individual wavelengths of the spectrum of the light source in a cone is followed by the cylindrical lens, which focuses the dispersed beam on the DMD so that it forms a thin wide rectangle at the surface of DMD where the total reflectance at each wavelength is controlled by the number of micromirrors that are turned on. Light reflected from the DMD passes through the cylindrical lens and individual wavelengths are recombined at the grating again. The beam that is spectrally processed is coupled back into a single-mode optical fiber via a fiber-pigtailed collimator. This setup is similar to the one summarized in Figure 5.1.

A major challenge in such a modular system is the overall power efficiency. SLDs, which are commonly employed in OCT because of their large bandwidth and low cost, provide relatively low optical power (e.g. on the order of 1 mW). Therefore, it is not preferred to lose extra optical power which will decrease the incident power on the specimen, while incident power on the specimen is critical for SNR of the system and penetration depth in the specimen. The insertion loss of the PSP presented in Section 5.1 is measured at <7 dB. The sources for the loss in this system are the double-incidence of the light beam on the diffraction grating which has <100%

diffraction efficiency, throughput efficiency of the DMD that is estimated to be in the range of 65% including mirror reflectivity, fill factor, diffraction efficiency and duty cycle [Dudley 2003] and losses while coupling the light beam back into a single-mode fiber.

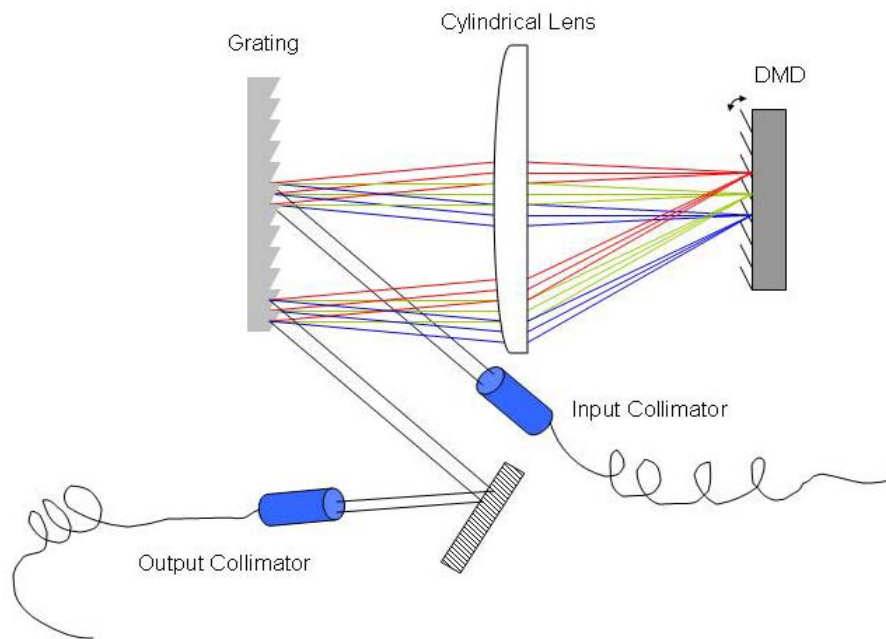


Figure 5.7: Schematic that presents a possible structure for an optical spectral shaper.

At a typical OCT wavelength band such as from 800nm to 1300nm, the first challenge to realize an optical spectral shaper is to find a diffraction grating with high diffraction efficiency over a wide wavelength band covering the broad bandwidth of the source. The OCT sources often emit unpolarized light. On the other hand, the efficiency of blazed diffraction gratings strongly depend on the state of polarization of the incident light being higher for one polarization state (except very low blaze angles). Furthermore, the efficiency of a grating is rated at a given

wavelength called blaze wavelength while measured in Littrow configuration. Littrow configuration describes a specific incidence angle for the beam when its first order diffracted light is retroreflected, i.e. travels on the same axis with the incident light. The diffraction efficiency with a light beam incident on a blazed diffraction grating with an angle different than Littrow angle may decrease significantly. For example, diffraction efficiency of a diffraction grating with 830 grooves/mm and 21.4° blaze angle, which is rated to be $\sim 90\%$ at Littrow configuration, is computationally expected to decrease down to $\sim 60\%$ when the incidence angle is 50° which would add up to 4.4 dB loss in a double-pass configuration. In practice, loss is measured as low as ~ 10 dB including the fill factor on the photodiode of the power meter. To implement an optical spectral shaper with a reflective blazed diffraction grating operated in Littrow configuration is physically not possible given that the first-order diffracted beam propagating in a cone is to be collected by a lens and projected on to the DMD. Near-Littrow configuration can be implemented if the DMD is aligned to operate in retroreflective mode. Otherwise, the beam returning to the grating gets out-of-focus at the grating surface when the grating and the lens are not parallel, i.e. the grating is tilted to establish near-Littrow configuration. The incidence angle of the incoming light beam can be adjusted to implement a near-Littrow configuration keeping the grating and lens parallel. However, for small blaze angles this can be challenging. The retroreflective configuration requires a circulator at the fiber collimator to direct the returned light beam into another port rather than letting it go back to the source [Riza 2003]. One challenge at this step is the absence of broadband circulators at common OCT source wavelengths such as ~ 900 nm in the market. Without a circulator, operating the system in near-retroreflective mode can be a solution but the coupling of the returning light that

propagates close to the incident light beam in to a single mode fiber would be very challenging. Resonant diffraction gratings can be a good solution in obtaining high diffraction efficiencies in off-Littrow configuration. Recently, a research group has reported over 99% diffraction efficiency in the -1st order of a resonant diffraction grating made of a mirror, a dielectric layer and high index corrugation at layer-air interface at 1064 nm wavelength [Destouches 2005].

In an optical spectral shaper comprising a DMD, the DMD is employed as a reflective binary spatial light modulator (SLM) which controllably attenuates the optical power contained at certain wavelength bands over the source power spectrum given that each individual wavelength is incident on a sufficiently large micromirror array. Figure 5.8 demonstrates the transmission curve of DMDs which are optimized for different spectral ranges; UV, VIS and IR. The DMD from Texas Instruments consists of 1024x768 micromirrors with individual micromirror pitch size of 13.68 μm and $\sim 0.4 \mu\text{m}$ spacing between neighboring micromirrors. Each micromirror can be tilted in a binary fashion $\pm 12^\circ$ or $\pm 9.2^\circ$ on a diagonal axis. When tilted the DMD forms a 2D coarse diffraction grating with 13.9 μm grating pitch. The disadvantage of the DMD in such a configuration is the occurrence of many Fraunhofer diffraction orders when a coherent light beam is incident. While in many displays and optical imaging applications a large number of diffracted orders can be collected over a large solid angle, coupling all diffracted orders into a single-mode optical fiber in photonics applications is challenging.

Texas Instrument's DMD manufactured for telecom applications in the near infrared (DMD-IR) is specially designed to have $\pm 9.2^\circ$ tilt angle. In such a design the DMD forms a switched blazed

grating with 88% of the diffracted energy coupled into a single diffraction order at 1550 nm [Duncan 2002, Dudley 2003]. This DMD has been used in dynamic optical filtering and optical switching around the 1550 nm wavelength band [Dudley 2003]. However, it has been showed that the diffracted energy is shared by adjacent diffraction orders for a DMD with $\pm 10^\circ$ tilt angle at the same wavelength band [Duncan 2003].

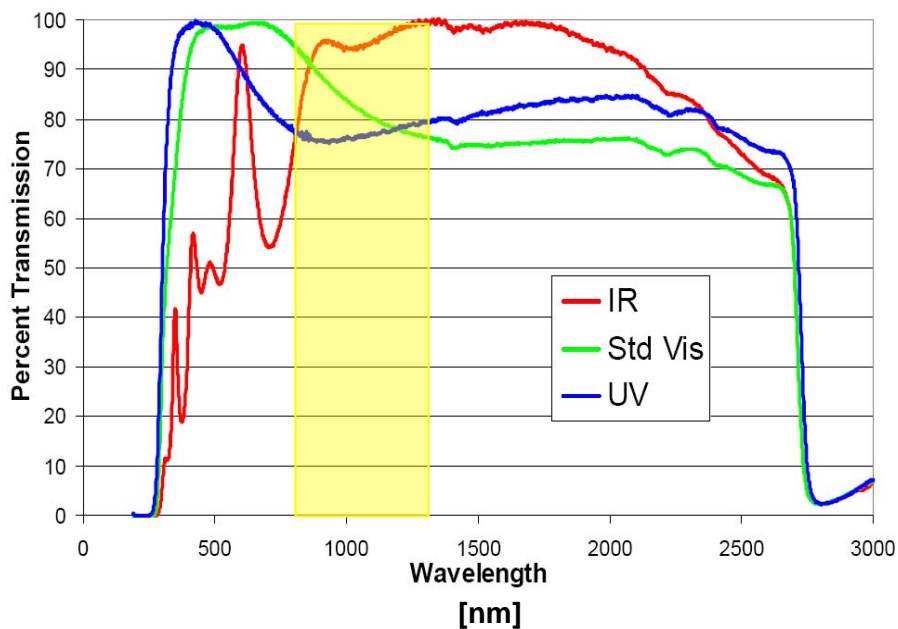


Figure 5.8: Transmission curve of DMD provided in three different versions. [Dudley 2003]. The yellow shaded area shows the range most OCT light sources emit at.

For applications with a light source centered somewhere between 800nm and 950nm, we see in Figure 5.8 that the transmission of the DMD for visible light applications starts to decrease smoothly in that wavelength band, while the one for IR makes a sharp increase particularly around ~900 nm both lacking a flat spectral response at 100%. Therefore, we decided that the visible light version of the DMD is more suitable for applications in low near-infrared up to

about 1000 nm. One major concern while using DMD-VIS is how it diffracts the incident beam. To observe the phenomenon, we visualized the diffraction pattern of DMD-VIS with $\pm 12^\circ$ tilt angle. A modelocked femtosecond Ti:Sapphire laser centered at 820 nm with a bandwidth of ~ 100 nm was employed. We used a fiber-pigtailed collimator to illuminate the DMD. Figure 5.9(a) shows the beam profile at the output of the collimator captured with a CCD camera. In Figure 5.9(b) we present the light beam reflected and diffracted by DMD when each micromirror was tilted $+12^\circ$. Figure 5.9(c) presents the diffraction pattern when a checker image was uploaded to the DMD so that some square groups of the micromirrors were tilted $+12^\circ$ and some -12° . In Figures 5.9(b) and (c) we see the 0^{th} order diffracted beam or reflected beam on the right-hand-side of the figures and many diffracted orders in 2D. The energy in the light beam is clearly spatially dispersed into many diffracted orders because of the DMD. To design an optical system to collect all diffracted beams in one spot and couple it into a single-mode fiber is a challenging task if possible. However, the MEMS mirrors employed as a reflective spatial light modulator like in a DMD can still be a promising technology for realization of modular optical spectral shapers especially considering the achievements which increased the diffraction efficiency in the IR version of the DMD to 88% in one diffracted order. Similar optimizations can be expected from manufacturers for operations at other wavelengths.

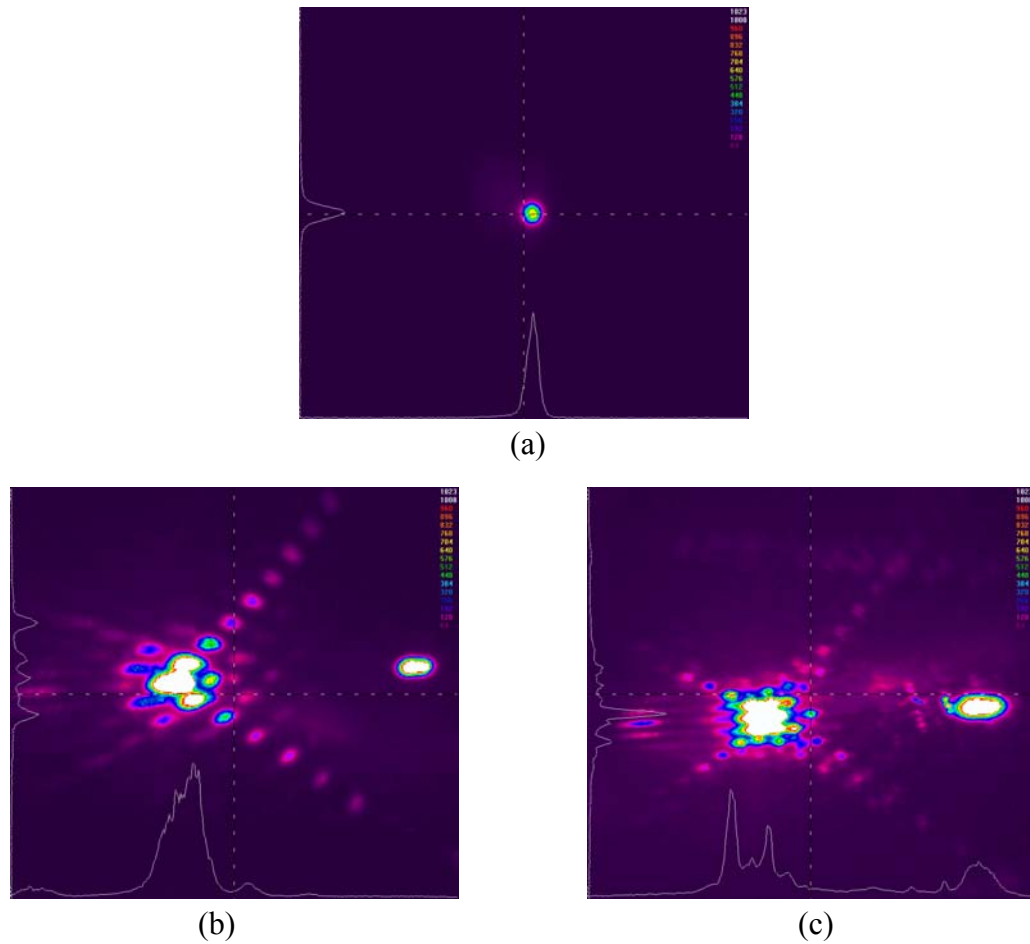


Figure 5.9: Beam profile (a) at the output of fiber collimator, (b) after DMD with micromirrors all tilted $+12^\circ$, and (c) after DMD where mirrors form a ‘checker image’

5.3 The Impact of Spectral Shaping on Task-Based Assessment

In Section 4.3 we introduced a statistical framework for task-based assessment in OCT [Rolland 2005]. The idea behind the task-based assessment is to optimize the imaging system by performing an objective assessment with some different system parameters such as the source

coherence length, the shape of the source power spectrum, the local variations of index of refraction in specimen scanned etc. In this approach specific tasks are defined and carried out by an observer. The evaluation of the performance of the observer is based on some quantitative results provided by the observer such as detectability and AUC. Therefore, the observer may also be called the evaluator. A mathematical framework is needed to be derived for the OCT system, the specimen being scanned, i.e. imaged, the tasks and the observer in order to perform a quantitative task-based assessment where the tasks in our case are chosen to be two classification tasks: signal-detection and resolution tasks. In this work, the impact of spectral shaping presented in Section 5.1 was analyzed with a task-based assessment method.

In our analysis we determined to use the Hotelling observer which implements an optimal linear discriminant [Barrett 2004]. The linearity of the discriminant ensures that it is easy to compute and less information about test data statistics is needed. An optimal linear discriminant maximizes a certain measure of separability of the classes defined in a classification task. The Hotelling observer maximizes the detectability measure d^2 , which is also called effective SNR, as well as the AUC when the test data is normally distributed. The Hotelling observer uses the information of mean vectors of test data and covariance matrices to generate the detectability and AUC.

5.3.1 Mathematical Model

We can represent any test data, i.e. signal or image as an N-by-1 column vector \mathbf{I} , which is in our case a set of photocurrent signal $I(t)$ acquired and sampled at the output of the OCT

photodetector. The detectability index i.e. the detectability, or effective signal-to-noise-ratio (SNR), associated with the performance of the Hotelling observer is given by

$$d^2 = \mathbf{X}^\dagger \mathbf{K}^{-1} \mathbf{X}, \quad (5.7)$$

where \mathbf{X} is a N-by-1 column vector representing the difference in the ensemble averaged vectors of the two classes of binary classification task for the hypothesis H_0 and the hypothesis H_1 which are discussed in Section 4.3. If the detected photocurrent signal supports the hypothesis H_0 , then it belongs to the 0th class and the signal vector is denoted by \mathbf{I}_0 . Similarly, if the photocurrent signal indicates that the hypothesis H_1 is true, we denote the signal vector by \mathbf{I}_1 . Hence, the vector \mathbf{X} will be given by

$$\mathbf{X} = \langle \dots \langle \mathbf{I}_1 \rangle \dots \rangle - \langle \dots \langle \mathbf{I}_0 \rangle \dots \rangle, \quad (5.8)$$

where $\langle \dots \langle * \rangle \dots \rangle$ indicates the ensemble average over all sources of randomness. The quantity \mathbf{K} in Equation 5.7 is an N-by-N matrix which represents the weighted average covariance matrices across the two classes based on their priori probability. If we assume that the probability of occurrence of each class is the same, i.e. one half, then \mathbf{K} will be given by

$$\mathbf{K} = \frac{1}{2}(\mathbf{K}_1 + \mathbf{K}_0), \quad (5.9)$$

where \mathbf{K}_i are the autocovariance matrices under each class (i.e. $i=0, 1$). The elements of the autocovariance matrix may be written as

$$K_i(t_n, t_m) = \langle \langle \langle I_i(t_n) I_i(t_m) \rangle \rangle \rangle - \langle \langle \langle I_i(t_n) \rangle \rangle \rangle \langle \langle \langle I_i(t_m) \rangle \rangle \rangle. \quad (5.10)$$

We can relate the detectability to a common scalar quantity called the area under the receiver operating characteristics curve (AUC), under the assumption that the Hotelling test statistic is normally distributed under each class [Barrett 1998 and 2004]. This normality assumption can be justified under the central limit theorem since the Hotelling test statistic is a linear combination of the components of the data vector and, for the task we are considering, these components are statistically independent random variables. The relation between the AUC and the detectability is given by

$$\text{AUC} = \frac{1}{2} + \frac{1}{2} \text{erf} \left(\frac{\sqrt{d^2}}{2} \right). \quad (5.11)$$

where $\text{erf}(\cdot)$ is the error function.

5.3.2 Evaluation of the Hotelling Observer Performance

We described in the Section 5.3.1 the basics on how to quantify the performance of a Hotelling observer by computing the associated detectability and AUC. The photocurrent signal derived indeed possesses two sources of randomness as discussed in Section 3.2. While the electrical field emitted by the source presents circular Gaussian statistics, the photodetection is a Poisson process due to the random arrival of photons at the detector. Thus, we derived the mean photocurrent signal in Equation 3.25 as

$$\langle\langle I(t) \rangle\rangle = \frac{e\rho}{\Delta t} \int_{-\infty}^{\infty} r(t-t') \left[\int_{-\infty}^{\infty} |m(\omega, t)|^2 S(\omega) d\omega \right] dt' , \quad (5.12)$$

which accounts for two sources of randomness. As a result, we should accordingly update the sampled autocovariance matrix elements shown in Equation 5.10 to include averaging over both sources of randomness as

$$K_i(t_n, t_m) = \langle\langle I_i(t_n) I_i(t_m) \rangle\rangle - \langle\langle I_i(t_n) \rangle\rangle \langle\langle I_i(t_m) \rangle\rangle . \quad (5.13)$$

A more explicit expression for the autocovariance matrix elements for the i^{th} class is needed to simulate the detectability and AUC for a task. Such an expression is given by [Rolland 2005]

$$K_i(t_n, t_m) \approx \left(\frac{e}{\Delta t} \right)^2 \int_{-\infty}^{\infty} r(t_n - t') r(t_m - t') \langle\langle N_i(t') \rangle\rangle dt' , \quad (5.14)$$

where a general definition of the mean photocurrent $N(t)$ is given by

$$\langle\langle N(t) \rangle\rangle = \rho \int_{-\infty}^{\infty} |m(\omega, t)|^2 S(\omega) d\omega . \quad (5.15)$$

As shown in Equations 5.12, 5.13 and 5.14 the source power spectrum is related to the mean number of photoelectrons $\langle\langle N(t) \rangle\rangle$, the mean photocurrent $\langle\langle I(t) \rangle\rangle$, and the autocovariance matrix \mathbf{K} which are critical parameters for the computation of the detectability and thus the AUC. Therefore, the spectral characteristic of the light source employed is expected to strongly affect the performance of the Hotelling observer.

Having the mathematical expressions to compute the detectability index and AUC of the Hotelling observer, we need to model a specimen to be employed in the imaging system, so the performance of the observer may be computed for a given task. In this investigation, we choose a single layer specimen model such as a glass plate bounded by two different interfaces (A and B) as shown in Figure 5.9. This Figure illustrates a more explicit specimen model similar to the one in Figure 4.1. The first interface is assumed to be between air and the front surface of the specimen which reflects a portion of the light beam, which is assumed to be normally incident on the surface, due to the change in refractive index from 1 to n , where n is the refractive index in the specimen. The second interface is modeled to be between the specimen and a substrate with a refractive index given by $n+\Delta n$. The Fresnel reflection coefficients at the first and second interfaces at normal incidence are given by

$$r_1 = \frac{1-n}{1+n} \quad , \quad r_2 = \frac{-\Delta n}{2n + \Delta n} \quad . \quad (5.16)$$

The more general expressions of the Fresnel coefficients would be used for non-normal incidences in future applications [Born and Wolf 2002]. Representing the thickness of the layer by a variable Δd , the phase accumulation of light propagating in the layer is given by $\exp(i\omega n m \Delta d / c)$ where m is the number of passes through the layer and c is the speed of light in vacuum. Assuming that the rest of the system is not optical frequency-dependent the frequency response of the sample arm $\hat{\alpha}_s(\omega)$ is given by

$$\hat{\alpha}_s(\omega) = r_1 + (1 - r_1^2) r_2 \exp\left(i\omega \frac{n2\Delta d}{c}\right) \quad , \quad (5.17)$$

where we assume that the reflected optical power becomes negligible for the second and higher order reflections at the interfaces depicted by a dashed line in Figure 5.10.

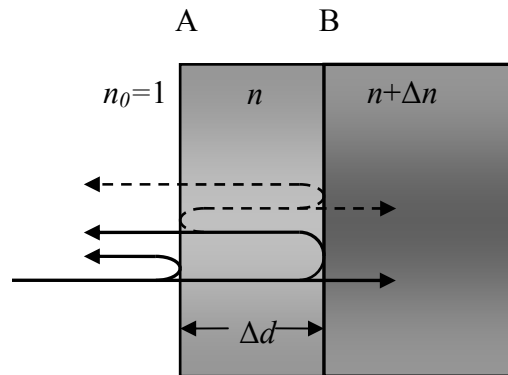


Figure 5.10: Specimen model: n is the refractive index of the specimen and Δn is the change of refractive index from the specimen to the substrate.

5.3.3 Task Definitions

We focused our investigation on two classification tasks, a signal-detection task and a resolution task, for the performance assessment of the Hotelling observer in OCT imaging. These tasks shall be performed by the Hotelling observer as described above and the performance will be evaluated using the detectability and AUC analysis.

The signal detection task is established to specify the minimum change in refractive index Δn between the specimen layer and the substrate at the second interface, which can be detected by the system. The thickness of the layer Δd is set to a constant quantity which is approximately twice the source coherence length so that the light beams reflected from the first and second interfaces (A and B) of the specimen do not interfere. If there is no second interface to be

detected, then the hypothesis H_0 is true. Under ideal conditions there is no second interface if Δn equals zero. On the other hand, the second interface can be detected, i.e. there is a second interface, for any non-zero value of Δn . This is the case when hypothesis H_1 is true. The observer computes the detectability and AUC as a function of Δn in order to determine how they behave with increasing values of Δn .

The goal of the resolution task is to assess the minimum thickness of the specimen layer that the system can discriminate and to observe the performance of the observer with increasing thickness of the specimen. We set the change in refractive index from the specimen layer to the substrate Δn to various constant values. When the thickness of the specimen layer Δd equals zero, the second interface overlay the first interface. This is the true case for hypothesis H_0 . On the other hand for a nonzero thickness Δd the hypothesis H_1 is true, i.e. an interface may be resolved. The observer performance is quantified by computing the detectability and AUC as a function of the specimen layer thickness Δd . Figure 5.11 demonstrates the specimen structures for both hypotheses under each task.

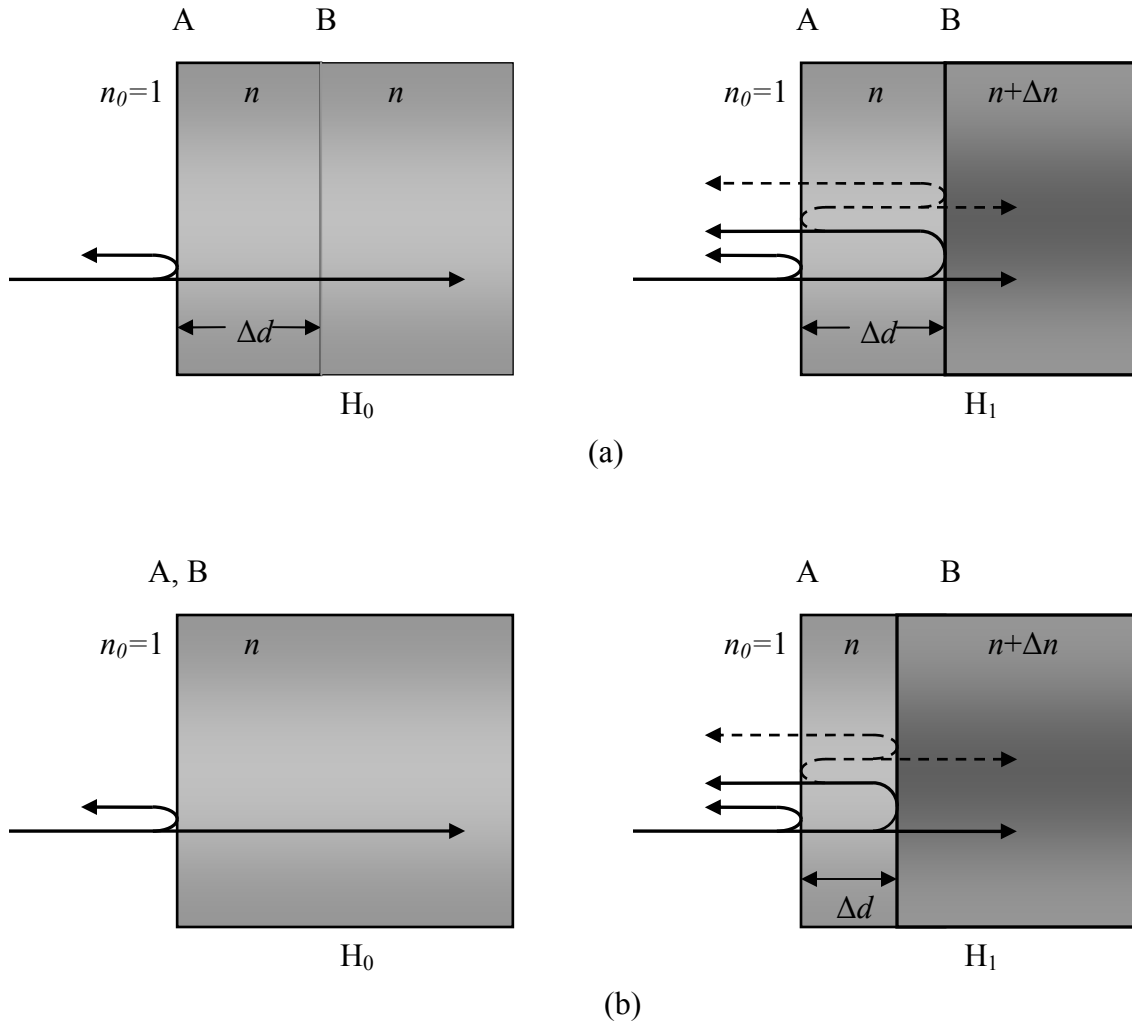


Figure 5.11: The structure of the specimen which presents the cases when the hypothesis is true for (a) signal detection task where the difference in refractive index between specimen and the substrate Δn is the variable, and (b) resolution task where the specimen thickness is the variable.

5.3.4 Simulation Results

We investigated the signal detection and resolution tasks while the Hotelling observer performed the task for different source power spectra. The first power spectrum we used in our simulation was that of a broadband amplified spontaneous emission (ASE) source (Newport BBS-430) emitting at $1565\pm 40\text{nm}$. Our goal was to compare the detectability and AUC for unshaped and shaped powers spectra of the same ASE source. We explained the spectral shaping process in Section 5.1. The measured wavelength power spectra of the source before and after spectral shaping that are shown in Figure 5.4(b) were prepared for simulations by first converting them to frequency spectra. The power spectra as a function of optical frequency were then normalized by the area under the original power spectrum, i.e. the source power before spectral shaping performed. Figure 5.12 presents each power spectra (S_0 : the original source power spectrum, S_1 and S_2 : shaped power spectra) prepared to be employed in the simulations. The original power spectrum of the ASE source contained significant spectral dips previously presented to cause side lobes in the PSF of the imaging system. With the spectral shaping process, smoother power spectra S_1 and S_2 with no spectral dips were created at the cost of 2.3 dB and 3.4 dB loss of optical power over the original power spectrum S_0 as discussed in Section 5.1.

The first step of the simulation procedure was to obtain the mean number of generated photoelectrons and thus the mean photocurrent signal and the autocovariance matrix. Then we derived and computed the detectability and AUC for either a signal-detection or a resolution task, while simulating those quantities, we ignored the losses and phase shifts of the beam splitter in the OCT system that was chosen to have free-space Michelson interferometer structure

as shown in Figure 3.1(a). The reference mirror was assumed to have a flat reflection response with 100% reflectivity for all frequencies; $\hat{\alpha}_r(\omega)$ is 1. Hence, $m(\omega, t)$ that is defined in Equation 3.14 and also appears in Equation 5.12 became

$$m(\omega, t) = \exp[i\phi_r(\omega, t)] + \left(r_1 + (1 - r_1^2) r_2 \exp\left(i\omega \frac{n2\Delta d}{c}\right) \right) \cdot \exp[i\phi_s(\omega, t)] . \quad (5.18)$$

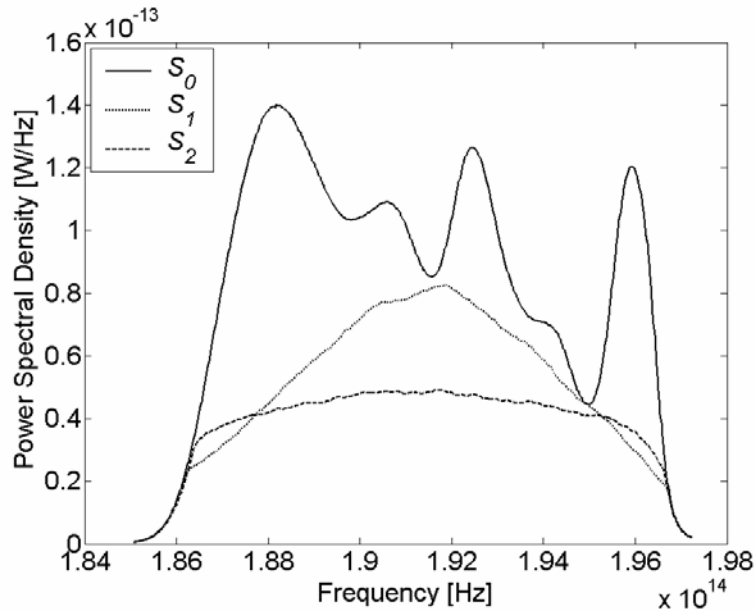


Figure 5.12: The frequency power spectrum of the ASE source S_0 ; solid curve, power spectrum after the first shaping operation S_1 (i.e. dotted curve) and after the second shaping operation S_2 (i.e. dashed curve).

The mean photocurrent signal of the OCT system was detected at a photodetector when the optical path in the reference arm of the interferometer is scanned, for example, by a linear translational stage moving at a constant speed of v_m . The increase in the optical path length of the reference arm was given by $v_m t$ where t is the time interval when scanning was performed.

Thus t presented the measurement time for one scan as well. The distance l_r was fixed to show

the distance from the beam splitter to the initial position of the reference mirror while l_s was the distance from the beam splitter to the front surface of the specimen. The phases accumulated in the reference and sample arms of the interferometer were then given by

$$\phi_r(\omega, t) = \frac{\omega}{c}(2l_r + 2v_m t) \quad \text{and} \quad \phi_s(\omega, t) = \frac{\omega}{c}2l_s, \quad (5.19)$$

and used in Equation 5.18. The distance l_r was assigned to be slightly smaller than l_s , i.e. $l_s - 28 \mu\text{m}$ so that the front surface of the specimen could be detected in scanning simulation. The measurement time t was set to 0.8 ms while the speed of the translational stage was 0.154 m/s. The photodetector modeled in the simulations had a bandwidth of 125 KHz (like that of a Nirvana Model 2017 photoreceiver) corresponding to 4 μs of detector integration time. Hence, we formed a time vector for the simulations that we performed using MatlabTM which consisted of 2000 discrete samples with 0.4 μs sampling period spanning from 0 to 0.8 ms so that the Nyquist sampling condition was satisfied. In all simulations, the refractive index of the specimen n , which was considered to be skin that is a potential specimen in future clinical applications, was chosen to be 1.4. We used trapezoidal numerical integrations to compute integral expressions.

5.3.4.1 Signal-Detection Task

We prepared and ran simulations for the signal-detection and resolution tasks separately. As previously described, the signal-detection task was performed to determine the impact of change in refractive index Δn on the detectability and AUC generated by the Hotelling observer, while

the specimen thickness Δd was set to a constant. We set the specimen thickness Δd to 50 μm , which was approximately twice the longest axial resolution computed for each power spectrum that were presented in Table 5.1. We simulated the detectability as a function of a change in refractive index Δn and demonstrated the results for each power spectra in Figure 5.13(a) while Δn was increased from zero to 2×10^{-5} . We then computed the AUC using Equation 5.11 and plotted the relation between the AUC and Δn in Figure 5.12(b). We did not increase Δn beyond 2×10^{-5} , because all AUC curves already reached their maximum that is unity before Δn equals 2×10^{-5} . The value of the AUC corresponds to the probability of signal-detection. For example, AUC equals one when the probability of signal-detection is 100%. Similarly, when AUC is 0.5, the probability of signal-detection is 50%.

Figure 5.13(a) shows that the detectability for the original, i.e. unshaped, power spectrum is larger than the ones for the two shaped power spectra for any non-zero Δn . The optical spectral shaping is based on attenuating optical power at certain wavelength bands and thus it causes inevitable power loss. If we denote the areas under the power spectrum curves in Figure 5.12 A_0 for S_0 , A_1 for S_1 and A_2 for S_2 , we can clearly see that $A_0 > A_1 > A_2$ where the area under power spectrum curve defines the optical power of the particular source. Indeed we see in Figure 5.13(a) that the power spectrum which encloses larger optical power leads to higher detectability at a given Δn . Similarly, the AUC curves in Figure 5.13(b) are observed to be rising to the maximum value of one faster for power spectra enclosing larger optical power.

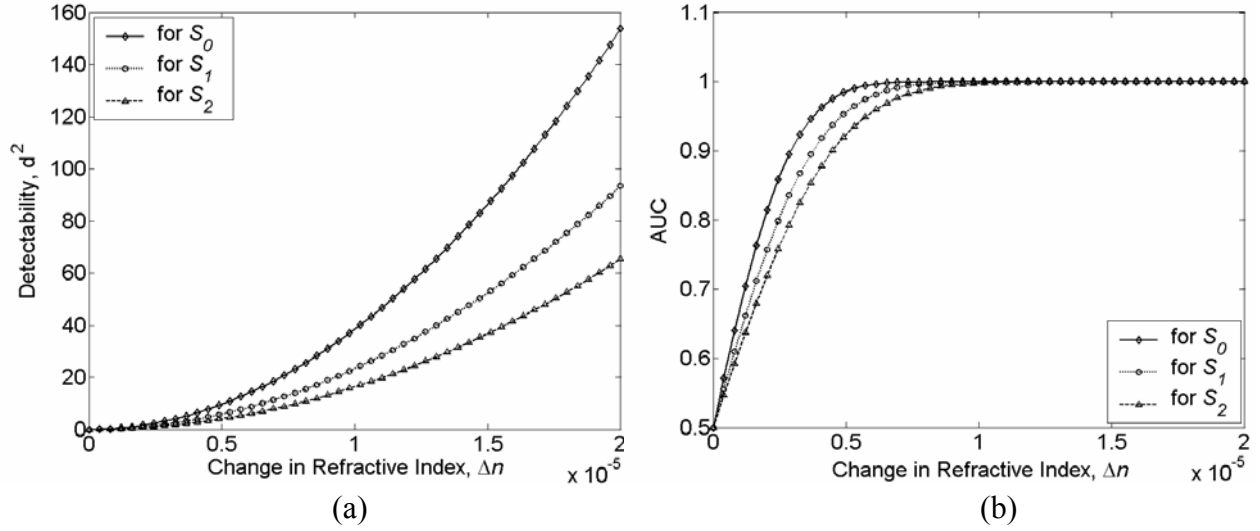


Figure 5.13: (a) Detectability and (b) AUC as a function of change in refractive index Δn between the specimen and the substrate.

To suppress the effect of difference in optical power in the simulations, we normalized each power spectra individually with its optical power, i.e. area under the measured power spectrum, so that each normalized power spectrum enclosed the same optical power which is unity. These power spectra are presented in Figure 5.14. For each power spectrum shown in Figure 5.14, we demonstrate in Figure 5.15 the AUC curves as a function of the change in refractive index. While the AUC curve for the original power spectrum is the same with the one shown in Figure 5.13(b), we observe that the AUC curves generated from power spectra with different spectral shapes but now with the same power are overlapping closely unlike in Figure 5.13(b). Both simulations demonstrate that the optical power is the dominant parameter while simulating the detectability and AUC for the changes in refractive index Δn in a signal-detection task.

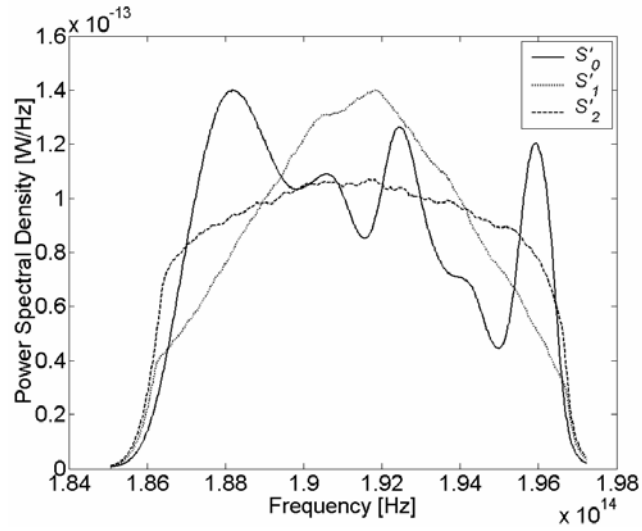


Figure 5.14: Power spectra each normalized to have unit optical power.

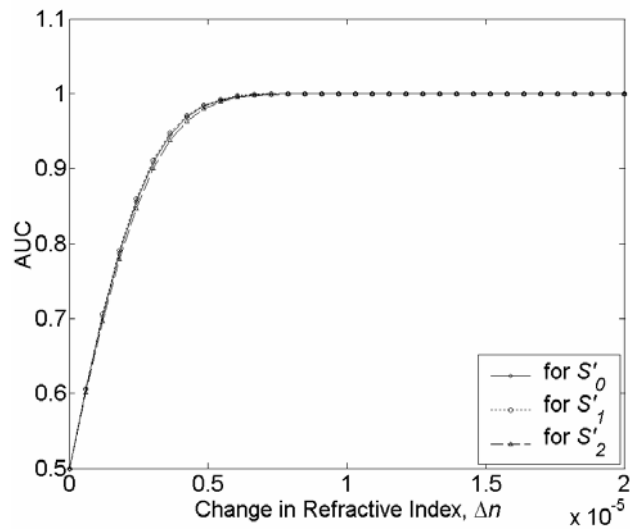


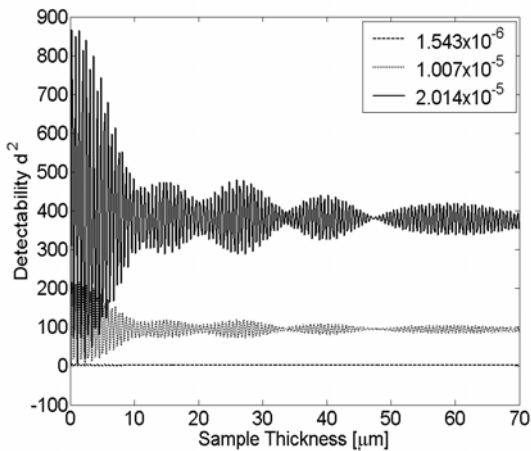
Figure 5.15: AUC curves computed using the power spectra shown in Figure 5.10.

5.3.4.2 Resolution Task

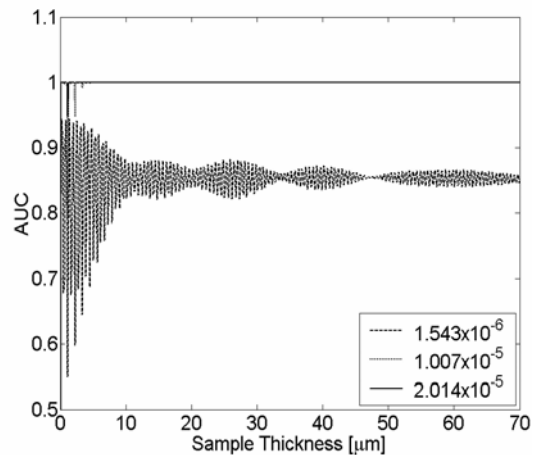
The goal of the resolution task is to quantify the minimum specimen thickness Δd for which the OCT system can resolve the reflections from the interfaces A and B of the specimen shown in Figure 5.10. To study the performance of the Hotelling observer for the resolution task, we set Δn to certain constant values and varied the specimen thickness Δd for each value of Δn . We used the information presented in Figure 5.13(b) to select values of Δn . From Figure 5.13(b), for each curve we selected the Δn , denoted Δn_1 , providing an AUC value of 0.75, i.e. 75% probability of signal-detection, and the minimum Δn , denoted Δn_2 , providing an AUC value of 1; We then doubled Δn_2 , which will be denoted Δn_3 . To simulate the performance of the Hotelling observer for the resolution task, we determined Δn_1 , Δn_2 and Δn_3 from Figure 5.13(b) as 1.543×10^{-6} , 1.007×10^{-5} and 2.014×10^{-5} for the power spectrum S_0 , and 1.976×10^{-6} , 1.160×10^{-5} and 2.320×10^{-5} for the power spectrum S_1 , and 2.362×10^{-6} , 1.365×10^{-5} and 2.730×10^{-5} for the power spectrum S_2 , where S_0 , S_1 and S_2 are shown in Figure 5.12. The detectability index and AUC as a function of the specimen thickness Δd for each power spectra and for the each selected change in refractive index value are shown in Figure 5.16. In the resolution task simulations, the specimen thickness is varied from zero to 70 μm which is larger than the twice of the maximum axial resolution presented in Table 5.1.

In Figure 5.16(a)-(c) we observe that the detectability for the resolution task increases with an increasing change in refractive index. AUC curves shown in Figure 5.16(d)-(f) reach the value of 1 faster for larger values of Δn . On the other hand, for all minimum changes in refractive index chosen Δn_1 , AUCs never reach one, which means that the probability of resolution for small

changes in refractive index never became 100%. However, those AUC curves tend to approach an asymptote about an AUC value of 0.85. Until reaching the asymptote, we observe oscillations in the AUC as well as detectability curves for specimen thicknesses of less than half the coherence length of the source, i.e. axial resolution of the imaging system. The oscillation period is measured as half the center wavelength of the source, which is the period of the interference fringes for any broadband light source centered at the same wavelength. Thus, the oscillations indicate that the light beam reflected from the first interface A interferes with the one reflected from the second interface B, when the specimen thickness satisfies the condition that the light beam travels an optical path less than half the coherence length in the specimen. The oscillations in AUC of the sources represented with power spectra S_1 and S_2 show that the probability of discrimination of interfaces by the Hotelling observer fluctuates continuously over a broader range of specimen thickness even if it is well above half the source coherence length in the specimen.



(a)



(d)

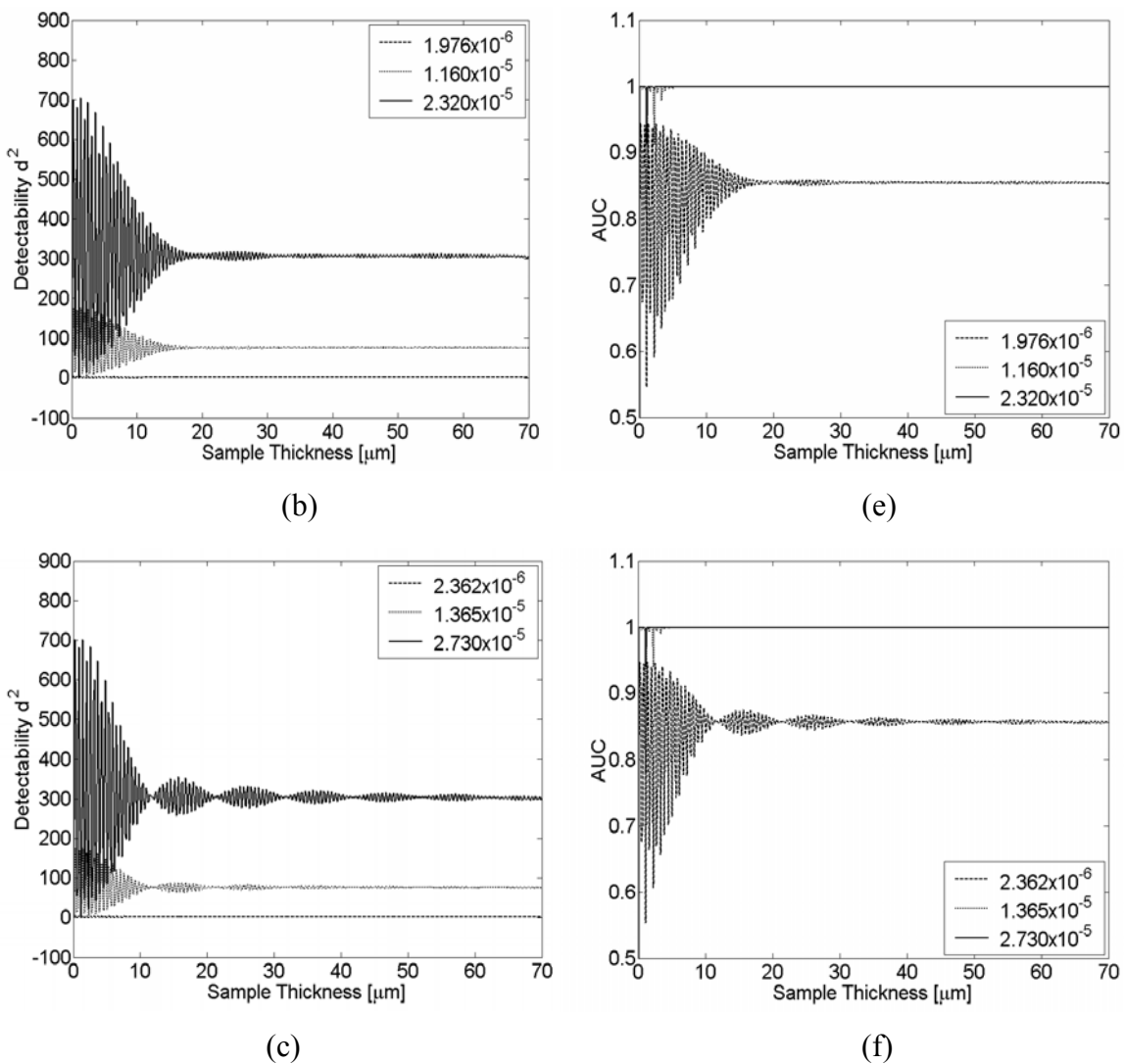


Figure 5.16: Detectability as a function of the specimen thickness for the ASE source (a) with the power spectrum S_0 , (b) with the shaped power spectrum S_1 , and (c) with the shaped power spectrum S_2 which are shown in Figure 5.8, and the corresponding AUC as a function of the specimen thickness for the power spectra (d) S_0 , (e) S_1 , and (f) S_2 .

5.3.5 Discussion

We demonstrated the impact of the source spectral shape on the performance of the Hotelling observer in a signal-detection task and a resolution task in optical coherence imaging. The noise

sources considered in the simulations are circular Gaussian noise from the broadband source and Poisson noise from the detector. Except for those sources of noise, the system is assumed to be ideal with unpolarized light, no dispersion in the specimen and imaging system, and linear scanning of a homogenous specimen with normally incident light experiencing Fresnel reflections at the boundaries of the specimen.

We showed that the spectral shape is a major factor in the quantitative assessment of performance when a resolution task is considered. Our analysis concluded that for a signal-detection task, the area under the power spectrum curve, i.e. the optical power of the light source, is dominant and sources with higher power provide larger detectability regardless of their shape. The associated AUC increases faster with a same change in refractive index Δn and reaches unity at smaller values of Δn as well. When we equalized the optical power of the light source with various spectral shapes, results showed that the AUC for each power spectra overlapped closely. This finding indicates that shaping the source power spectrum does not have an impact on the OCT performance for the signal-detection task we defined and that the optical power of the light source is the major factor defining the performance of the system for this specific task.

The second set of simulations presented the performance of the Hotelling observer for the assessment of a resolution task. Results showed that spectral irregularities in the source power spectrum lead to fluctuations in detectability and AUC curves over a large range of specimen thicknesses while the local variation in refractive index Δn is relatively small, e.g. 1.543×10^{-6} . For larger values of Δn , we observed that the detectability index as a function of the specimen

thickness had larger values and the AUC curves reached 1 for small values of specimen thickness. This phenomenon means that the Hotelling observer can discriminate the interfaces for any non-zero distance between them if Δn has a relatively large value [Rolland 2005]. Such an outcome was original considering classical concepts for axial resolution, which states that two distinct layers can be resolved if the distance between layers, i.e. interfaces, is as large as the measure obtained by a metric presented in Chapter 4. However, in the task-based metric for resolution described above, the results show how the axial resolution depends also on the local variations of index of refraction in the specimen scanned. Importantly, the analysis indicates that the second interface can be resolved even if it is extremely close to the first one, i.e. the distance between them is less than half the source coherence length, under some circumstances. An example to such circumstances shown above is a large enough change in the index of refraction at the interface or layer. As an example, in Figure 5.16(f) this change corresponds to 2.73×10^{-5} .

CHAPTER SIX: DETECTION ELECTRONICS IN OCT

In this Chapter, we discuss a crucial component in OCT imaging, which is the detection electronics. We demonstrate compact low-cost demodulating detection electronics with a monolithic integrated-circuit active filters and a logarithmic amplifier. Such an approach aims at the optimization of the size of the system towards compact imaging systems for clinical use. We first present the mathematical background of detection and then the design of the logarithmic amplifier-based OCT detection electronics. The sensitivity of the system with both the designed electronics and the commercial lock-in amplifier both having equivalent electrical bandwidth is quantified, and images of fresh onion recorded using both detection schemes are presented for comparison.

6.1 Analog Signal Processing

An OCT image is reconstructed by recording and processing the interference of broadband light beams back-scattered and/or back-reflected from a specimen with reference the light back-reflected from a retroreflector or mirror. Scanning the position of the reference retroreflector/mirror varies the optical range in the specimen from which light scattered or back-reflected can interfere with the reference light.

The motion at the reference retroreflector/mirror, which can be provided by placing it on a linear translational stage moving at a speed v_m , induces a Doppler frequency shift f_D in the reference

beam. When the Doppler shifted reference beam is recombined with the sample beam at the beam splitter of the interferometer to produce interference at the photodetector, the Doppler shift is transferred to the frequency of the generated electrical signal. In other words, the detected electrical signal is modulated or heterodyned. We can model the Doppler shift modulation in the axial PSF of the OCT system starting from the general signal expression given by

$$\langle\langle I(t) \rangle\rangle = \frac{e\rho}{\Delta t} \int_{-\infty}^{\infty} r(t-t') \left[\int_{-\infty}^{\infty} |m(\omega, t)|^2 S(\omega) d\omega \right] dt' , \quad (6.1)$$

where the term $m(\omega, t)$ will be modeled to present the axial PSF measurement, i.e. there are perfect mirrors or retroreflectors in both arms of the interferometer and no additional losses present. Under such assumptions $m(\omega, t)$ is given by

$$m(\omega, t) = \exp[i\phi_r(\omega, t)] + \exp[i\phi_s(\omega, t)] = \exp\left[i\frac{\omega}{c}2(l_r + v_m t)\right] + \exp\left[i\frac{\omega}{c}2l_s\right], \quad (6.2)$$

where l_r is the distance from the beam splitter to the initial position of the reference arm mirror and l_s is the distance from the beam splitter to the sample arm mirror whose position is fixed during the measurement. The magnitude or absolute square of $m(\omega, t)$ is given by

$$|m(\omega, t)|^2 = 2 + 2 \operatorname{Re} \left\{ \exp \left[i \left(\frac{\omega}{c} 2(l_r + v_m t) - \frac{\omega}{c} 2l_s \right) \right] \right\} . \quad (6.3)$$

The first term in Equation 6.3 ends up as a DC signal in the signal shown in Equation 6.1, while the second term forms an AC signal which is given by

$$\langle\langle I(t) \rangle\rangle_{AC} = \frac{2e\rho}{\Delta t} \operatorname{Re} \left\{ \int_{-\infty}^{\infty} r(t-t') \left[\int_{-\infty}^{\infty} S(\omega) \exp \left[i \left(\frac{\omega}{c} 2(l_r - l_s) + \frac{\omega}{c} 2v_m t \right) \right] d\omega \right] dt' \right\}. \quad (6.4)$$

When we replace ω by $\omega - \omega_0 + \omega_0$ in Equation 6.4, where ω_0 is the center frequency of source power spectrum, then Equation 6.4 becomes

$$\begin{aligned} \langle\langle I(t) \rangle\rangle_{AC} \propto \operatorname{Re} \left\{ \int_{-\infty}^{\infty} r(t-t') \left[\exp \left[i \frac{\omega_0}{c} 2(l_r - l_s + v_m t) \right] \right. \right. \\ \left. \left. \times \int_{-\infty}^{\infty} S(\varpi + \omega_0) \exp \left[i \frac{\varpi}{c} 2(l_r - l_s + v_m t) \right] d\varpi \right] dt' \right\}, \end{aligned} \quad (6.5)$$

where $\varpi = \omega - \omega_0$. In Equation 6.5 l_r and l_s are non-varying quantities, thus l_r minus l_s is a constant. Hence the term $\omega_0 2(l_r - l_s)/c$ represents a phase term ϕ_Δ which depends on the initial position of the reference arm and sample arm mirrors. The time-varying term $\exp[i\omega_0 2v_m t/c]$ in Equation 6.5 includes the Doppler shift in the electrical frequency domain that is induced by the motion of the scanning reference arm mirror. The modulation of the signal by the Doppler shift can be expressed by

$$\exp \left[i \frac{\omega_0}{c} 2v_m t \right] = \exp \left[i 2\pi \left(\frac{\nu_0 2v_m}{c} \right) t \right] = \exp \left[i 2\pi \left(\frac{2v_m}{\lambda_0} \right) t \right], \quad (6.6)$$

where the amount of the Doppler shift is given by $f_D = \nu_0 2v_m / c = 2v_m / \lambda_0$ as previously derived in Section 3.2 in a different mathematical framework. As we see in Equation 6.6 both the speed of the translational stage and the center wavelength of the broadband light source

illuminating the OCT system affect the amount of Doppler frequency shift. We can derive an expression for the electrical bandwidth of the detected signal, Δf , where the expression is given by $\Delta f = \Delta v 2v_m / c = \Delta \lambda 2v_m / \lambda_0^2 = \Delta \lambda f_D / \lambda_0$. Other depth scanning mechanisms, for example the Fourier-domain optical delay line (FD-ODL), may be configured to shift the center frequency of the electrical signal as well, where the FD-ODL parameters also set the electrical bandwidth of the signal similar to the expression above [Rollins 1998].

An OCT system can also employ an external phase modulator, such as a piezoelectric fiber stretcher [Sato 2000, Akcay 2001], a piezo-stack [Hoeling 2000], an acousto-optic phase modulator [Xie 2003], or an electro-optic phase modulator [de Boer 2001]. Considering that a sinusoidal modulating signal is applied, the externally phase modulation of a signal denoted $s(t)$ and given by $A \exp[i\omega t]$ will be presented including an additional sinusoidal oscillating frequency term as

$$\tilde{s}(t) = A \exp\left[i\left(\omega t + M \sin(\omega_m t)\right)\right], \quad (6.7)$$

where \tilde{s} represents a phase modulated term, M is the modulation index and ω_m equals $2\pi f_m$, where f_m is the modulation frequency. Thus, when there is phase modulation, the expression in Equation 6.5 becomes

$$\begin{aligned} \langle\langle I(t) \rangle\rangle_{AC} \propto \operatorname{Re} \left\{ \int_{-\infty}^{\infty} r(t-t') [\exp[i(\omega_D t + \phi_\Delta + M \sin(\omega_m t))] \right. \\ \left. \times \int_{-\infty}^{\infty} S(\varpi + \omega_0) \exp\left[i \frac{\varpi}{c} 2(l_r - l_s + v_m t)\right] d\varpi \right\} dt' \end{aligned} \quad (6.8)$$

where ω_D is $2\pi f_D$ where f_D is described earlier. The modulation term can be expanded into Fourier series such that it becomes

$$\exp[iM \sin(\omega_m t)] = \sum_{p=-\infty}^{\infty} J_p(M) \exp[ip \omega_m t], \quad (6.9)$$

where $J_p(M)$ is the p^{th} order Bessel function of the first kind [Haykin 1994, Akcay 2001]. With the given expression of the phase modulation, the phase modulated signal will be given by

$$\begin{aligned} \langle\langle I(t) \rangle\rangle_{AC} \propto \operatorname{Re} \left\{ \sum_{p=-\infty}^{\infty} \int_{-\infty}^{\infty} r(t-t') [J_p(M) \exp[i(\omega_D + p \omega_m)t + i \phi_\Delta] \right. \\ \left. \times \int_{-\infty}^{\infty} S(\varpi + \omega_0) \exp\left[i \frac{\varpi}{c} 2(l_r - l_s + v_m t)\right] d\varpi \right\} dt' \end{aligned} \quad (6.10)$$

In Equation 6.10 we see that the overall frequency shift in the modulated signal equals to the sum of the Doppler shift and an integer multiple of the external modulation frequency. While the integer p determines the order of the Bessel function of first kind, the modulation index M is the parameter which decides what amplitude it takes. That is, given the modulation index M , we demodulate the p^{th} harmonic of the modulated signal given that the p^{th} order Bessel function takes on the largest amplitude. For example, we should demodulate the second harmonic signal if the amplitude of $J_1(M)$ is smaller than the one of $J_2(M)$.

Figure 6.1 presents the RF frequency distribution of the signal which was detected by a fiber-optic OCT system. The phase modulation was performed by a piezoelectric fiber stretcher which was driven with a 20 kHz triangular voltage waveform. We took the measurement at the output of the photoreceiver via an RF spectrum analyzer (HP3585A). The interference signal was detected, while the optical path lengths of each interferometer arm was set to be equal and both fixed, i.e. no Doppler shift present. We observed first four harmonics of the signal and partially the fifth harmonic which was centered at 100 kHz. A fiber-optic based imaging system with a piezoelectric fiber stretcher as a phase modulator is presented in Section 6.2.

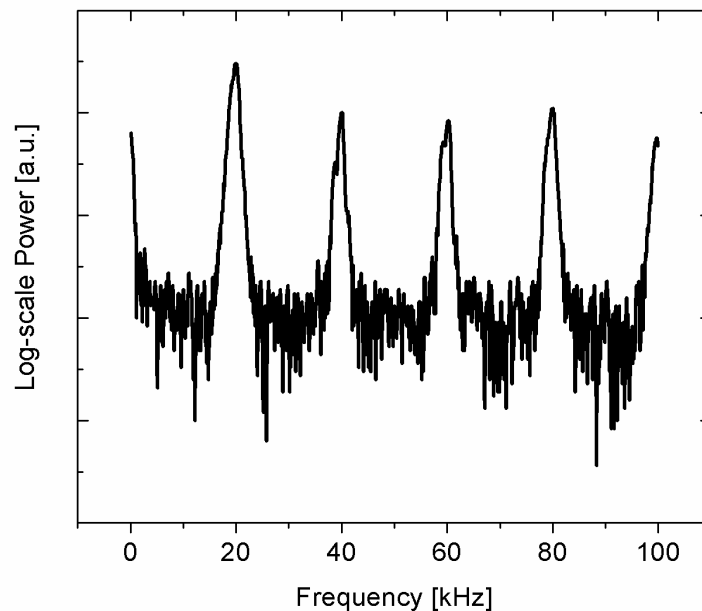


Figure 6.1: Interference signal phase modulated by a piezoelectric fiber stretcher driven at 20 kHz

There are three important steps included in the detection electronics stage of an OCT system, where the detected analog signal is processed. These steps are:

1. Transimpedance amplification of the photocurrent signal generated by the photodetector.
2. Electrical Filtering.
3. Envelope detection or demodulation.

A transimpedance amplifier, which is a unit usually embedded in a photoreceiver converts the photocurrent signal generated at the photodetector to a voltage signal. The voltage signal is modulated at the sum of the Doppler shift and an integer multiple of the modulation frequency. Furthermore, it is bandlimited having an electrical bandwidth given by Δf which is described above for one case where the scanning is provided by a translational stage. The electrical filter is employed to filter the signal at the total modulation frequency and in the band of the signal. Therefore, the ideal electrical filter is the one that is a band pass filter centered at the total modulation frequency having a pass band as narrow as the signal bandwidth. The final stage of the detection electronics is the demodulation process, i.e. envelope detection, of the filtered signal. Lock-in amplifiers [Izatt 1996], demodulating logarithmic amplifiers [Rollins 1998], RMS voltmeters [Hoeling 2000], analog CMOS circuits [Kariya 2004], and field-programmable gate arrays (FPGA) [Schaefer 2004] have been employed in various OCT systems for analog signal processing after photodetection. The detection electronics that amplifies the OCT signal and conducts the demodulation sets the sensitivity and SNR [Hee 2002]. After the detection electronics stage, the analog OCT signal is sampled and converted to a digital signal. The digital signal is acquired by a data acquisition board (DAQ) and is recorded in the hard disk of a PC. A

set of detected OCT signals processed and then acquired by a DAQ board is prepared to present for example a cross-sectional image of the specimen scanned.

6.2 Imaging System

We implemented a fiber-based OCT system using single mode optical fiber as shown in Figure 6.2. The light source illuminating the system is a superluminescent diode (Superlum D930-HP) centered at 930 nm with ~80 nm spectral bandwidth. The optical power was measured as 0.33mW at the sample arm which is the optical power incident on the specimen. Two custom-designed broadband fiber couplers that can support the large bandwidth of the light source were employed in the system to enable the dual-balanced detection of the interference signal. A 50/50 fiber coupler was employed in the system to provide the second light beam for the dual-balanced photoreceiver. We terminated the free arm of the 50/50 coupler with an index matching oil to minimize reflection from the fiber-end that otherwise adds an extra DC current in one of the photodiodes of the photoreceiver. The interferometer was configured with a second fiber coupler (i.e. 80/20) which directed 80% of the input light to the sample arm and 20% to the reference arm. We wound a portion of the optical fiber in the reference arm around a piezoelectric tube. The piezoelectric tube expands and stretches the optical fiber when a voltage is applied, which enables phase modulation of the light traveling in the reference arm.

A gold-coated retroreflector placed on a linear stage that can scan as fast as 25 mm/sec (Newport VP-25XA) provided depth scanning of the sample while a second stage was employed for transversal scanning. The returning phase modulated reference light was recombined with the

light scattered or back-reflected from the sample at the 80/20 fiber coupler. While a part of the recombined light was directed to one of the two InGaAs photodiodes in the dual-balanced photoreceiver (Nirvana Model 2017), the rest returned to the 50/50 fiber coupler where it was split to reach the other photodiode.

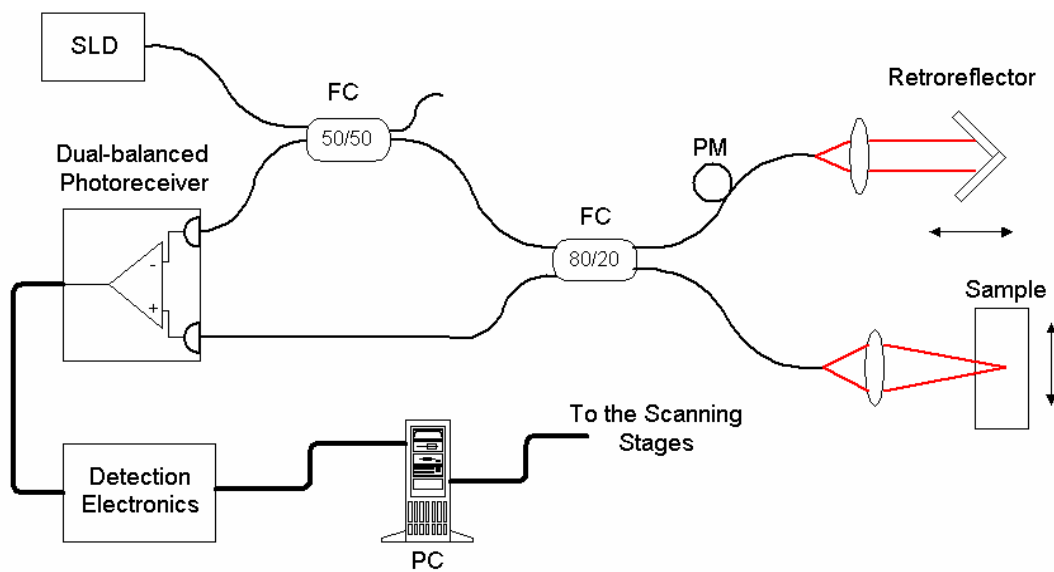


Figure 6.2: Schematic of the time-domain OCT system implemented with dual-balanced detection. SLD: Superluminescent Diode, FC: Fiber Coupler, PM: piezoelectric phase modulator. A PCI DAQ card in the PC acquires the signal processed by the detection electronics. The PC also controls the scanning stages.

We chose the dual-balanced detection technique to eliminate intensity noise of the light source [Podoleanu 2000]. The dual-balanced photoreceiver subtracts the photocurrents generated by the two photodiodes, and also includes a built-in transimpedance amplifier. The input signal of the detection electronics has two important characteristics: it is modulated at a frequency which is set by the sum of the Doppler frequency shift and the frequency of the voltage waveform driving

the piezoelectric phase modulator, and it is subject to various noise processes such as $1/f$ and detector noise some of which are outside the bandwidth of the signal and therefore can be filtered out. We first employed a lock-in amplifier (Stanford Research SR-830) as detection electronics in our system shown in Figure 6.1. We then replaced the lock-in amplifier with custom-designed detection electronics, detailed in Section 6.3. The signal generated by the detection electronics was acquired by a PCI data acquisition (DAQ) board that performed the analog-to digital conversion. A PC was employed to record the digital signal and to form an image at the end of the scanning process while controlling the motion of the stages.

Lock-in amplifiers are often used in the demodulation process in many applications. They are able to measure AC signals within a certain frequency band isolating it from out-of-band noise components. Figure 6.3 shows a simple diagram for a lock-in amplifier. The modulated signal at the input of the lock-in amplifier is multiplied with a reference signal that is a sinusoidal signal oscillating at the total modulation frequency of the input signal, while it is multiplied in another channel by the same reference signal that is phase shifted by 90° . If the first harmonic of the modulated input signal is to be demodulated, the frequency of the reference signal will be given by $f_D + f_m$. From the well-known rules of trigonometry, the result of the multiplication of two sinusoids is two AC signals one oscillating at the difference frequency and the other one at the sum frequency. Therefore, the resulting signal after multiplication and before low pass filtering (LPF) has a DC component and a high frequency component at two times the input signal frequency, when the reference signal is set to have the same frequency as the input signal. The high frequency component is then filtered out by LPF. The two channel multiplication in a lock-

in amplifier is useful when the phase of the input signal is desired to be measured in reference to the phase of the reference signal which is set by the user. However, phase information is lost when envelope detection is performed.

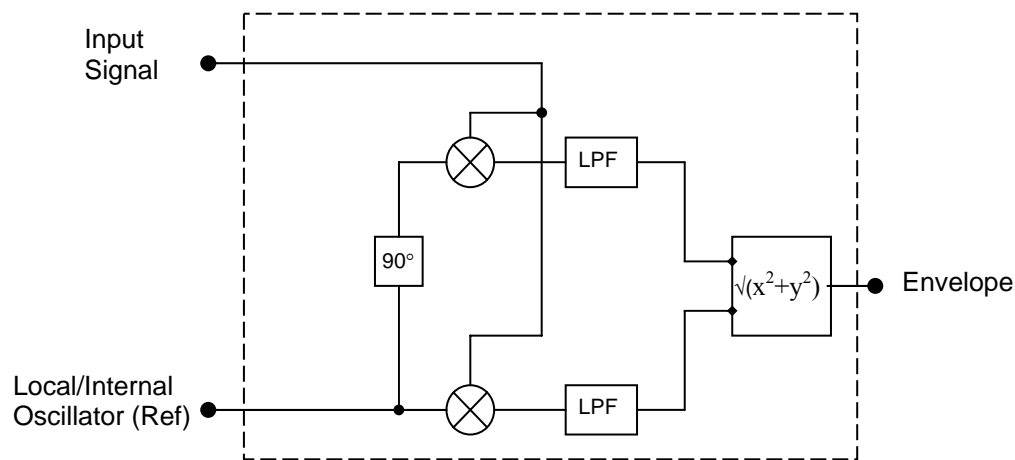


Figure 6.3: Diagram of a lock-in amplifier

6.3 Custom-designed Detection Electronics

The designed detection electronics serves to filter out-of-band noise components in the signal detected by the dual-balanced photoreceiver and to perform demodulation like a lock-in amplifier but much smaller in size. The OCT signal generated with the system shown in Figure 6.2 was phase modulated at 38.5 kHz. Active bandpass filters are commonly used for applications below 100 kHz, while at higher frequencies passive bandpass filters are preferred [Hee 2002] to filter a modulated signal.

We designed and implemented custom-electronics comprising a bandpass filter (BPF) followed by a demodulating logarithmic amplifier, a low pass filter (LPF), and a single-ended-to-differential amplifier. The BPF is a 4th order Butterworth band pass filter with two cascaded universal active filters (Burr Brown UAF42) that implement a KHN biquad topology. The UAF42 filters operate in the frequency range between 0 to 100 kHz and can be configured to realize Butterworth, Chebyshev, and Bessel filter types. The center frequency of the filter was set to 38.5 kHz, which corresponded to the sum of the Doppler shift and the modulation frequency induced by the piezoelectric fiber stretcher, with a 1.5 kHz bandwidth that can cover a signal bandwidth set by a scanning speed of up to 7.5 mm/s. The demodulating logarithmic amplifier is also an integrated circuit (Analog Devices AD606). The output of a logarithmic amplifier is the logarithm of the input signal's envelope [Nash 1999], but with a characteristic rectifier-type ripples that need to be removed with low pass filtering. Thus an LPF was implemented to be used after logarithmic amplifier with additional UAF42s. At the final stage, additional conversion gain was added by a single-ended-to-differential amplifier (Analog Devices AD8138). We implemented a switch to potentially bypass the LPF after the demodulating logarithmic amplifier. Figure 6.4 shows the block diagram of the designed detection electronics. Figure 6.5 shows the output response of the custom-designed detection electronics with the cascaded LPF and an additional gain unit after the demodulating logarithmic amplifier, which is called the case with modified gain. With only additional gain unit while the LPF is bypassed, the output response, which is titled the output with original gain, is also presented. In Figure 6.6 we present a sinusoid input waveform with a frequency of 38.5 kHz together with two output

waveforms, which are the envelopes of the input waveform obtained with LPF bypassed and not. The cutoff frequency of the LPF was set to 20 kHz which was below the frequency of the ripples appearing at the output of the logarithmic amplifier. Indeed, in Figure 6.6, we can see that the frequency of the rectifier-type ripples at the output waveform recorded with the LPF bypassed is ~77 kHz and those ripples in the signal were filtered out when the LPF was switched on.

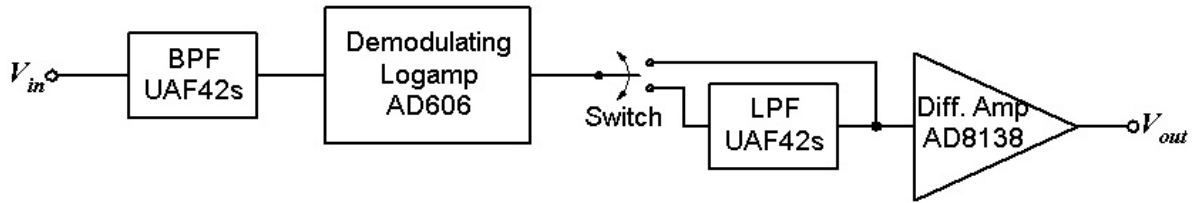


Figure 6.4: Schematic of the detection electronics designed to demodulate the OCT signal generated at the dual-balanced photoreceiver. BPF: Bandpass Filter, LPF: Low Pass Filter.

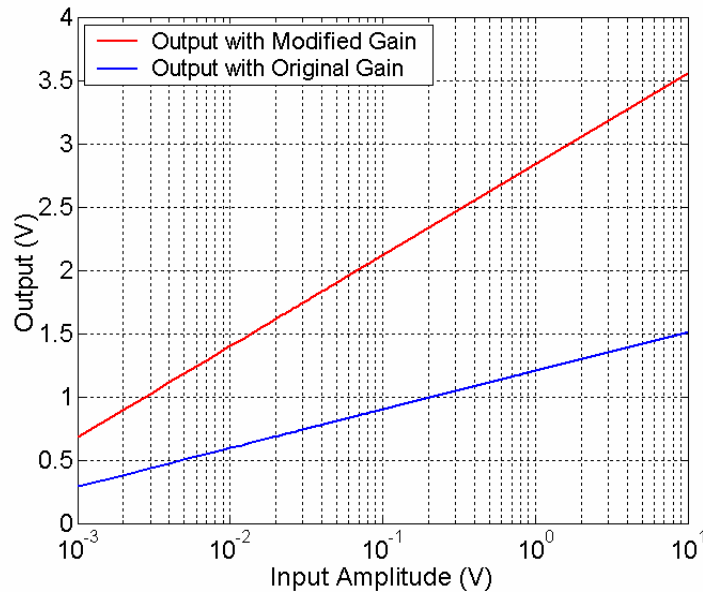


Figure 6.5: The output response of the detection electronics with and without the filtering and additional gain at the final stage.

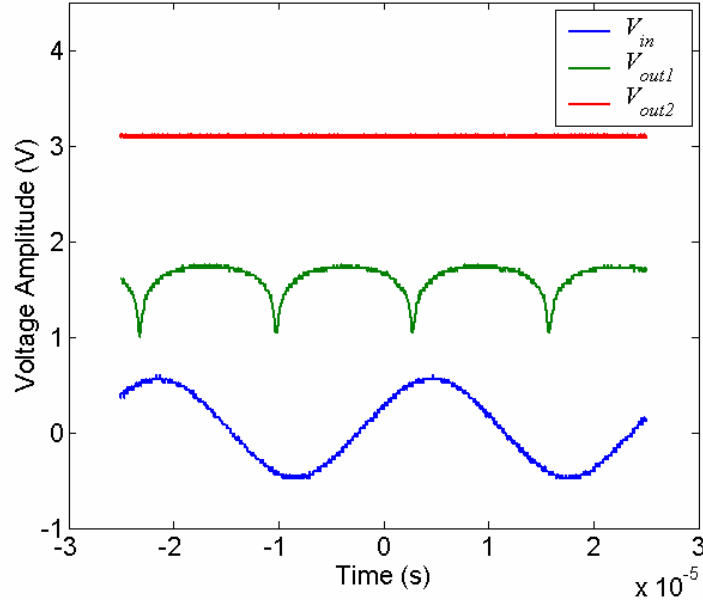


Figure 6.6: Input and output waveform relation of the designed OCT demodulator. Bottom sinusoid is the input waveform V_{in} . The middle curve is the output V_{out1} when the LPF is bypassed and the top curve V_{out2} is the output when the LPF is switched on.

The conversion formula for the detection electronics system with the low pass filter and additional gain stage after the demodulating logarithmic amplifier was measured as

$$V_{out} = 0.7172 \cdot \log_{10} \left[\frac{V_{in}}{0.000112} \right], \quad (6.11)$$

where V_{in} was the amplitude of the modulated input signal and V_{out} was the output of the detection electronics. The circuit was implemented on a 8cm x10cm four-layer printed circuit board. Figure 6.7 shows the photograph of the detection electronics implemented on the printed circuit board. In Appendix A, we present the circuitry of the detection electronics we designed.

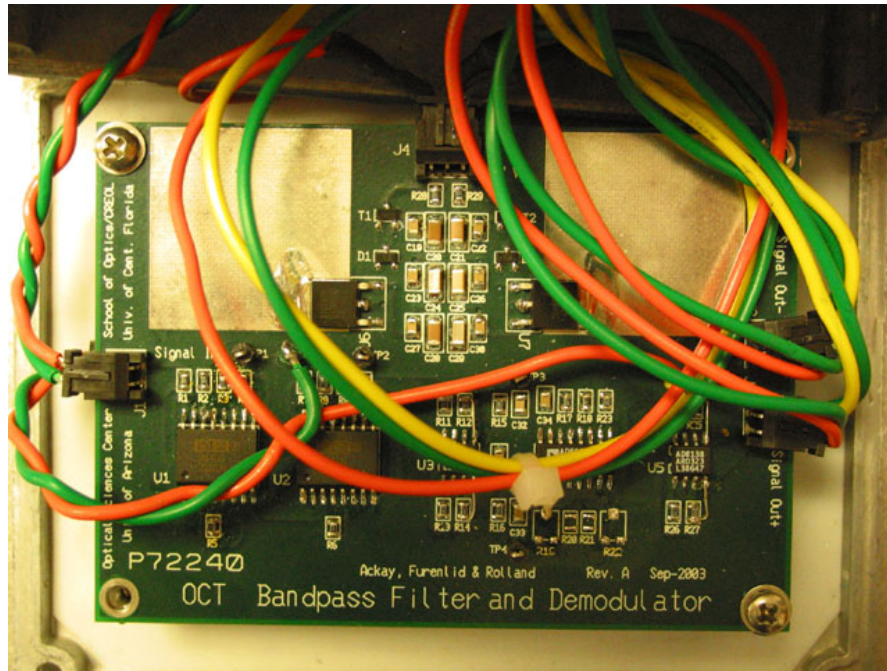


Figure 6.7: Photo of the printed circuit board designed for filtering and envelope detection.

6.4 Results

To quantify the sensitivity of the imaging system when the lock-in amplifier (Stanford Research SR830) and the new detection electronics were employed, we used an OD1.2 filter followed by a mirror in the sample arm of the setup shown in Figure 6.2. Figure 6.8 shows the structure of the sample and the focused sample arm light beam. We measured that the OD1.2 filter attenuates the optical power of the incident light by -12.36 dB. The controlled attenuation provided the information that the OCT signal peaked at -24.72 dB reflectivity given that the sample arm beam passes twice through the OD1.2 filter after being back-reflected by the mirror. Therefore, this

sample structure imitates a mirror that has a reflectivity of -24.72 dB while the mirror with no filter in front is assumed to have 100% reflectivity that corresponds to 0 dB. Fig. 6.9(a) shows the signal recorded with the lock-in amplifier. We then scanned the same sample configuration using our detection electronics for comparison. Fig. 6.9(b) shows the signal recorded with the custom-designed detection electronics. The time constant of the lock-in amplifier was set to 100 μ s which corresponds to a 1.59 kHz LPF bandwidth that is equivalent to the bandwidth of the designed detection electronics.

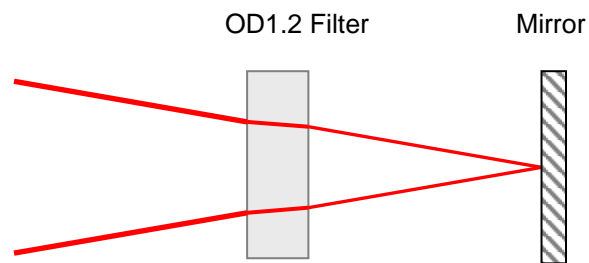


Figure 6.8: The sample configuration to determine the sensitivity of the OCT system shown in Figure 6.1.

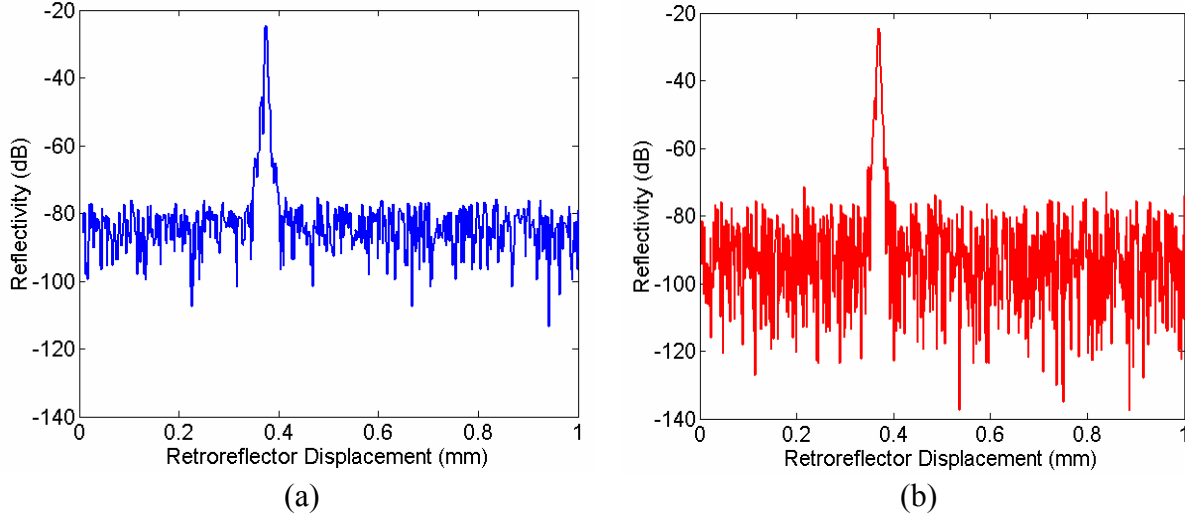


Figure 6.9: The OCT signals recorded using (a) the lock-in amplifier (SR830), (b) the custom-designed logarithmic amplifier-based detection electronics.

We then compared the performance of the designed detection electronics to the lock-in amplifier considering the sensitivity of the implemented system with both detection schemes. The system sensitivity is a measure which is defined by the reciprocal of the minimum detectable reflectivity. This definition means that sensitivity equals to SNR for the signal recorded with a 100% reflective sample. Such a case happens when all incident optical power is collected back. Given recorded signals shown in Figure 6.9, knowing that the optical power collected by sample arm focusing optics is attenuated by 24.72 dB, the sensitivity S of the imaging system is given by

$$S = 20 \cdot \log_{10} \left(\frac{V_p}{\sigma_n} \right) + 24.72 \text{ ,} \quad (6.12)$$

where V_p is the peak voltage of the detected signal and σ_n is the standard deviation of the signal noise floor [Laubscher 2002]. Table 1 shows the sensitivity of the imaging system with each detection scheme.

Table 6.1 System sensitivity S for the two detection electronics

OCT with	Sensitivity S (dB)
Custom-designed Detection Electronics	87.8
Lock-in Amplifier	88.8

In the final assessment step, we prepared a fresh-onion sample to obtain its cross-sectional OCT image using both detection electronics discussed above. The size of the imaged section of the onion sample was $500 \mu\text{m} \times 640 \mu\text{m}$. Figure 6.10(a) demonstrates the image recorded using the lock-in amplifier. Figure 6.10(b) shows an image of the same fresh-onion sample recorded using the custom-designed detection electronics. Due to the nature of the logarithmic amplifier, the images obtained with the custom designed detection electronics are in log-scale. However, the output from the lock-in amplifier is in linear scale and therefore such images were converted to log-scale after data acquisition. The images are 8-bit (255 gray level). No image averaging or image processing methods were applied. The polygonal structure of the onion sample is clearly visible in both images.

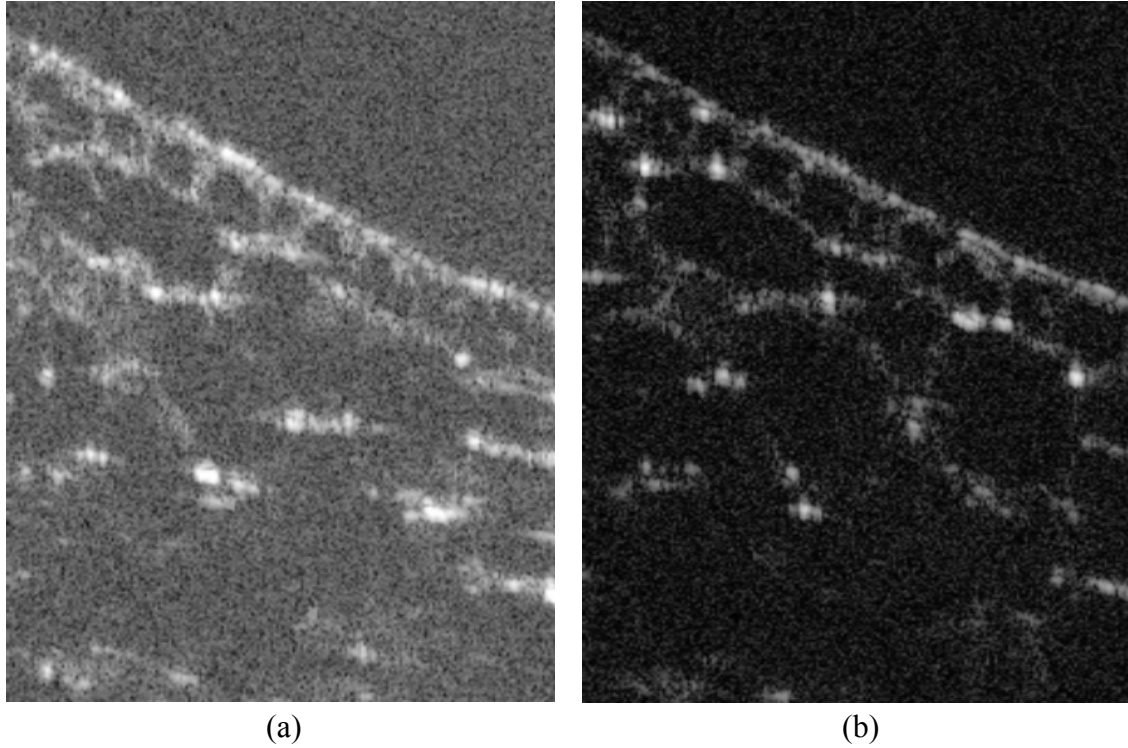


Figure 6.10: Onion image ($500 \mu\text{m} \times 640 \mu\text{m}$) where (a) the lock-in amplifier is employed to perform envelope detection, (b) the designed detection electronics is employed to process the analog signal generated by the photoreceiver.

6.5 Discussion

We analyzed the signal processing stage in OCT. While the optics of the imaging system set the limits for performance characteristics such as axial and lateral resolution, the sensitivity of the system depends on the detection electronics. We have demonstrated the feasibility of a compact and low-cost detection electronics implemented by a few ICs that filter, demodulate, and amplify the signal. While commercial lock-in amplifiers have the advantage of being tunable over a wide range of frequencies, which has value for optimization across various applications (e.g. real time

in vivo biomedical imaging versus *in vitro* biological imaging), the detection electronics we designed is targeted to operate purposely at fixed modulation frequency and signal bandwidth for *in vitro* or in the field biological imaging to achieve a compact and low-cost solution for portable imaging units. Importantly, we demonstrated that the portable unit provides an equivalent performance to the lock-in amplifier considering the system sensitivity. Presented detection electronics is easily adjustable to operate in any range from DC to 100 kHz by changing several surface mounted resistors. For modulations higher than 100 kHz, where the active filters are limited by the slew-rate and bandwidth requirements imposed on the operational amplifiers [Horowitz 1980], UAF42s can be replaced by passive filters comprising capacitor-inductor configurations which will not increase the size and cost of the system. Importantly, most lock-in amplifiers except some high-cost units that are quite large in size and thus not adequate for portable low-cost OCT systems do not operate in MHz range either.

CHAPTER SEVEN: SUMMARY OF CONTRIBUTIONS AND CONCLUSION

The work presented in this dissertation comprises three major contributions: a detailed discussion and theoretical analysis of axial resolution in optical coherence imaging considering the shape of the source power spectrum, the optimization of the imaging system performance via optical spectral shaping and the analysis of its impact on the system performance, and the design and development of a compact low-cost detection electronics which provides equivalent sensitivity to a commercial lock-in amplifier.

In optical coherence imaging the axial resolution that is typically in the range of 1-20 μm is a prominent advantage above many other biomedical or biological imaging systems such as commercial magnetic resonance imaging (MRI) systems that provide resolution on the order of $10^3 \mu\text{m}$ and ultrasound technology with resolution on the order of $10^2 \mu\text{m}$. Indeed, axial resolution is a major selling point of optical coherence tomography and microscopy considering that light gets absorbed in $<3 \text{ mm}$ in turbid tissue such as skin and thus cannot penetrate into such tissues as deep as MRI and ultrasound. Despite the importance of axial resolution, we do not see any reference specifically focused on this topic prior to 2002. Part of the work we conducted targeted to fill this gap and to provide an analytical presentation of axial resolution. The analysis consists of two important points: reliability of the current approach and its comparison with two other metrics, and the effect of the source spectral shape on axial resolution. Our work led to a publication [Akçay 2002] which now serves as a major reference to the studies on the quantification of axial resolution in optical coherence imaging systems. As part

of the work conducted, we critically approached and evaluated a common assumption, which suggested that approximating the spectral shape of a broadband light source with a known center wavelength and spectral bandwidth to a Gaussian was legitimate to estimate the coherence length and thus the axial resolution. Different metrics such as ASI and RMSW along with FWHM were employed in our computations for coherence length and compared to each other. We compared several cases. In one case, the axial resolution was compared for two source power spectra: a Gaussian, and a non Gaussian which was visibly close enough to a Gaussian but having a slight dip at the peak (1.4% below the peak amplitude). A ~10% difference in coherence lengths was reported although the two power spectra had the same center wavelength and spectral bandwidth. The analysis was extended to different power spectra having the same center wavelength and spectral bandwidth but different amplitudes of spectral dip. The formation of the side lobes in point spread function was presented in relation to the irregularities in the source power spectrum, while their effect on axial resolution was analyzed using different metrics as part of the key contribution. In the above studies the quantification of axial resolution was based on an ideal system, i.e. the dispersion in the system was considered to be zero, while later in a follow-up study, an analysis was conducted showing the impact of group velocity dispersion in the specimen on axial resolution [Lee 2005, Akcay 2005a].

Another key contribution of our work was the experimental demonstration of the side lobe inhibition in the axial PSF of an OCT system and the achievement of suppression of spurious structures in the reconstructed images by optical spectral shaping of the source power spectrum. Such an experimental study was presented to our knowledge for the first time [Akcay 2003].

This was a distinct work when compared to earlier studies directed towards the suppression of side lobes in the axial PSF, which were based on post-data acquisition digital signal processing. Furthermore, spectral shaping described a direct instrument optimization method that is the optimization of a broadband light source for the OCT imaging. In addition, we contributed a performance assessment method, called task-based assessment, which analyzed the impact of spectral shaping in OCT imaging. This method, which was demonstrated in OCT research for the first time by our group [Rolland 2004 and 2005], was employed to quantify the performance of the imaging system based on two tasks: a signal detection and a resolution tasks. Results showed that reshaping the source power spectrum was a benefit essentially to the resolution task, as opposed to both the detection and resolution tasks [Akçay 2005b]. In a signal detection task, the optical power of the source was shown to be the dominant factor regardless of the shape of the source power spectrum. In a resolution task, the importance of the specimen local variations in index of refraction was demonstrated showing that the axial resolution improved with increasing change in index of refraction at an interface in the specimen.

Finally, towards the optimization of OCT and OCM for use in clinical settings, we analyzed the detection electronics stage. Detection electronics is a crucial component of the system that is designed to capture extremely weak interferometric signals in biomedical and biological imaging applications. Drawbacks of a commercially available lock-in amplifier utilized to demodulate the detected signal are its size and cost. We designed and tested detection electronics to achieve a compact and low-cost solution for portable imaging units and demonstrated that the design provided an equivalent performance to the commercial lock-in amplifier considering the system

sensitivity [Akçay 2005c]. The implemented detection device consists of a few ICs that filter, demodulate and amplify the signal, therefore the device is extremely compact in size compared to a lock-in amplifier. While commercial lock-in amplifiers have the advantage of being tunable over a wide range of frequencies, which has value for optimization across various applications, the detection electronics we designed was targeted to operate purposely at fixed modulation frequency and signal bandwidth to create a compact and low-cost solution for portable imaging units. Nonetheless, designed detection electronics can be adjusted for applications in the frequency range from 0 to 100 kHz by changing several surface mounted resistors. Although changing resistors does not provide instant tunability, it gives the freedom to adjust the current detection electronics or implement new ones for specific bandwidth and center frequency in the given range prior to any targeted application.

As part of future work, the optical spectral shaping can be extended to operate at other common wavelengths and bandwidths for OCT sources. While different spectral shaping structures can be developed employing not only DMDs but also other spatial light modulators, techniques to overcome challenges in utilizing DMD-VIS can be developed. Also, micromirror based reflective spatial light modulators concentrating diffraction energy in a single order while operating at a desired wavelength and bandwidth may rise in the photonics market. On the other hand, major future work will be the extension of the task-based assessment method to include more complexity such as polarization effects, modulation, additional noise sources, scattering and dispersion.

APPENDIX A: CIRCUITRY OF DETECTION ELECTRONICS

In this appendix we present the electrical layout, i.e. circuitry, of the detection electronics which is described and discussed in Chapter 6. The full circuitry is demonstrated in four Figures. Figure A.1 shows the 4th order Butterworth filter that is designed with two UAF42 universal active filters to band pass filter an input signal modulated at ~40 kHz with a bandwidth of up to 1.5 kHz. In Figure A.2 we see the demodulating logarithmic amplifier (AD606) that follows the BPF. At the output of the AD606 we installed a switch which connects the output either to the next stage which includes an LPF that has a cutoff frequency of 20 kHz and a single-ended-to-differential amplifier (AD8138) which are shown in Figure A.3, or to the single-ended-to-differential amplifier bypassing the LPF so that we have the freedom to engage the LPF or not. Figure A.4 presents the voltage regulator which provides ± 5 Volts power supply to the AD606 and the AD8138 and ± 15 Volts to the UAF42's from ± 17 Volts DC input voltage from a laboratory DC power supply.

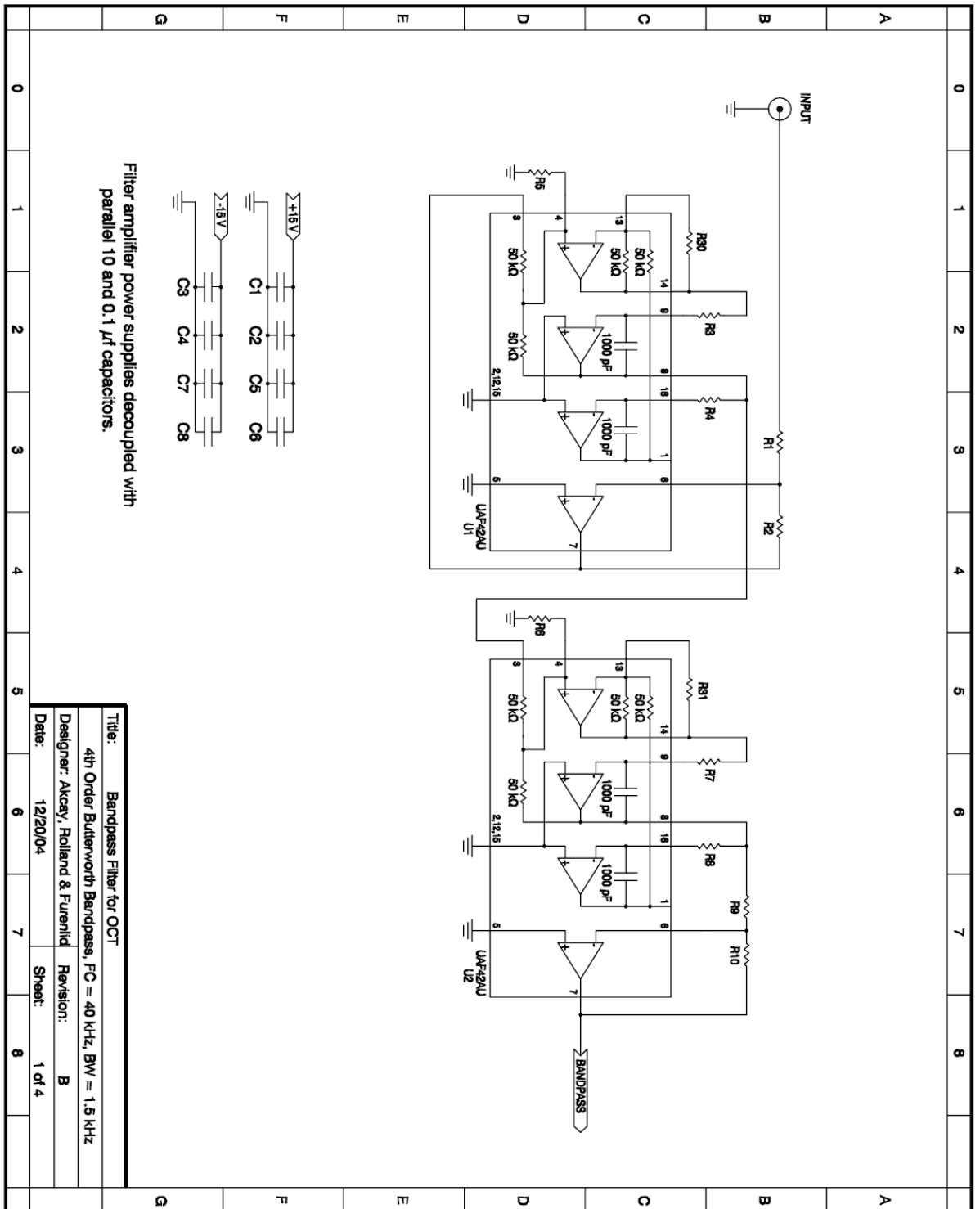


Figure A.1: BPF circuitry

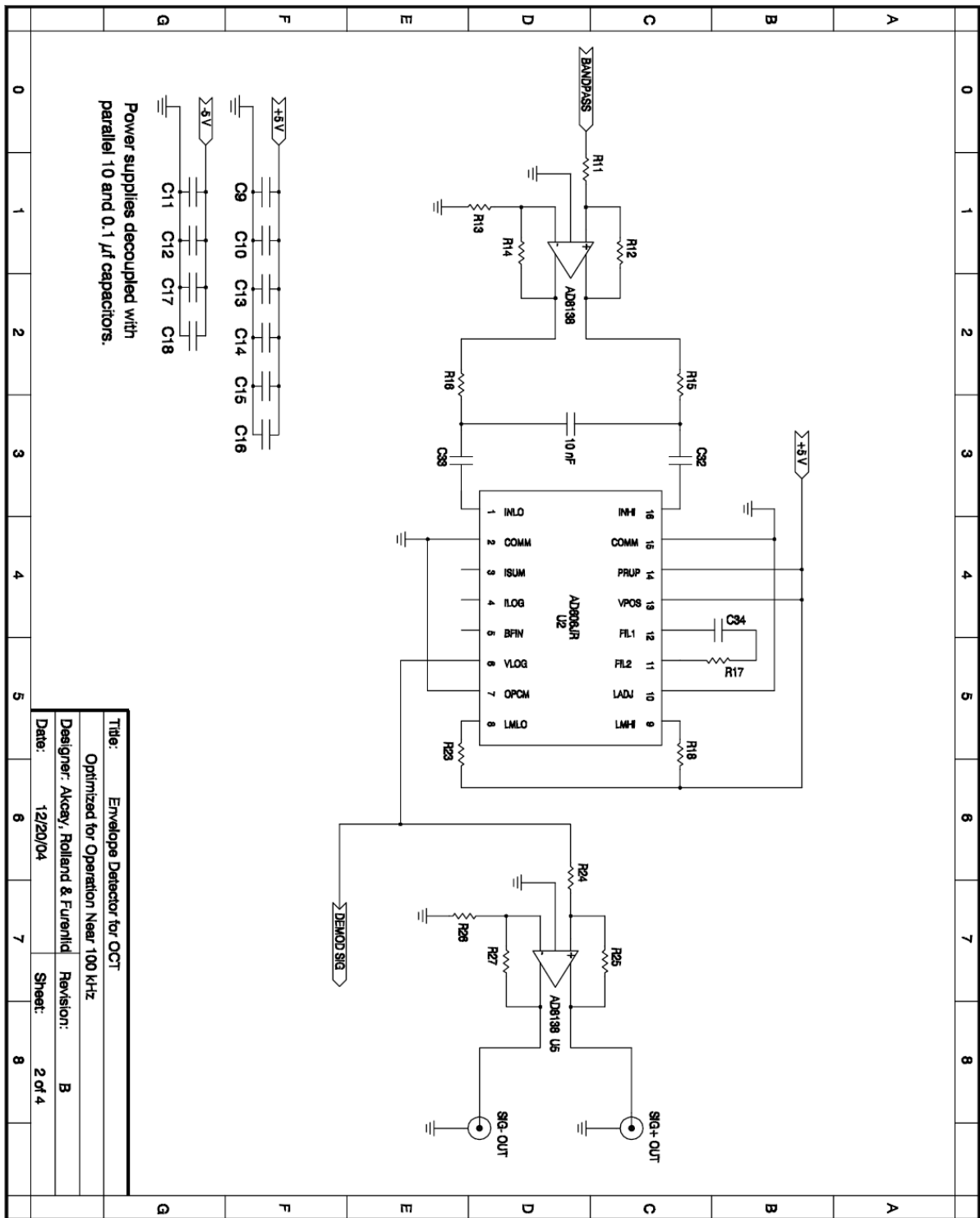


Figure A.2: Circuitry of the demodulation, i.e. envelope detection stage

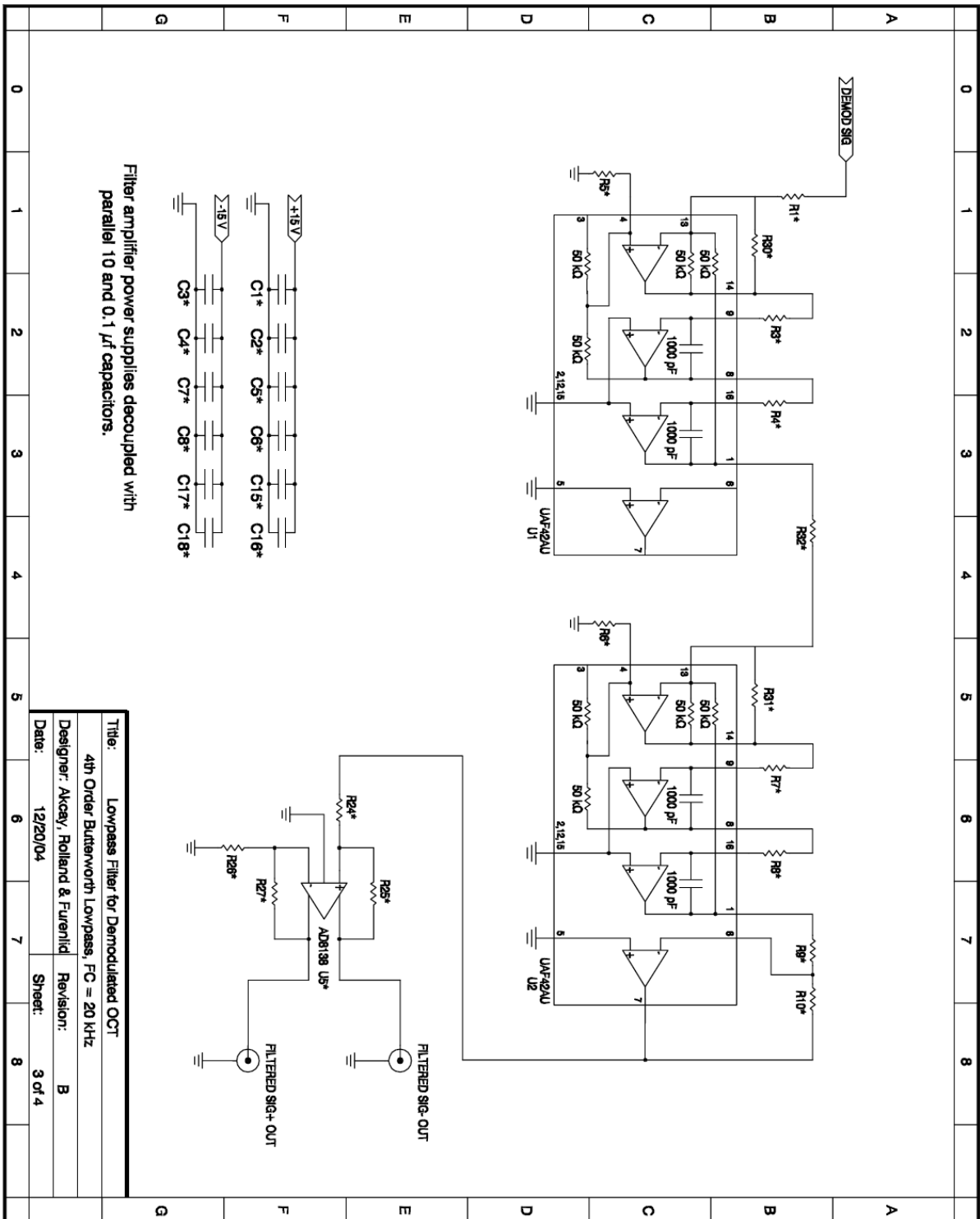


Figure A.3: Circuitry of LPF

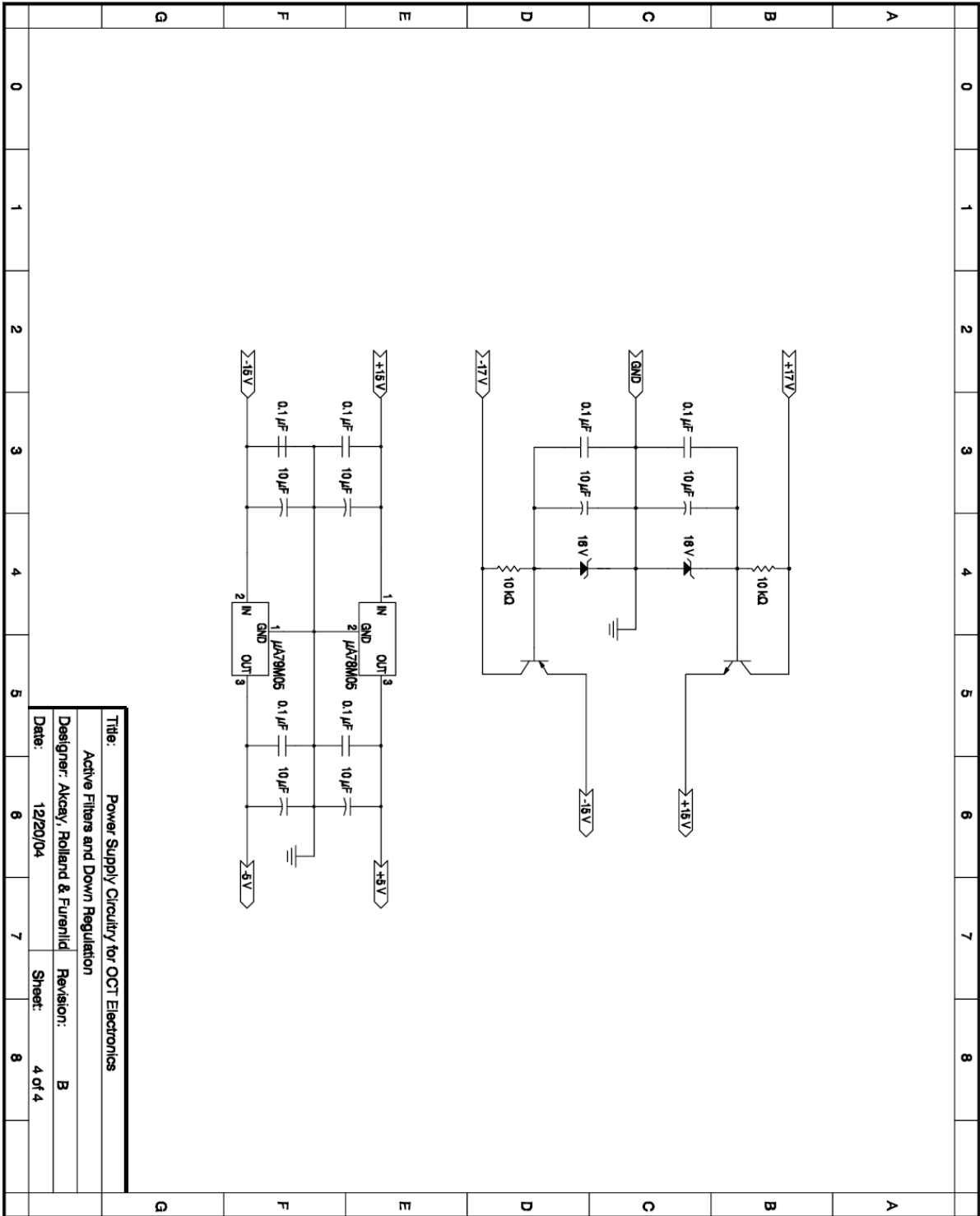


Figure A.4: Power supply circuitry

APPENDIX B: LABVIEW INTERFACE

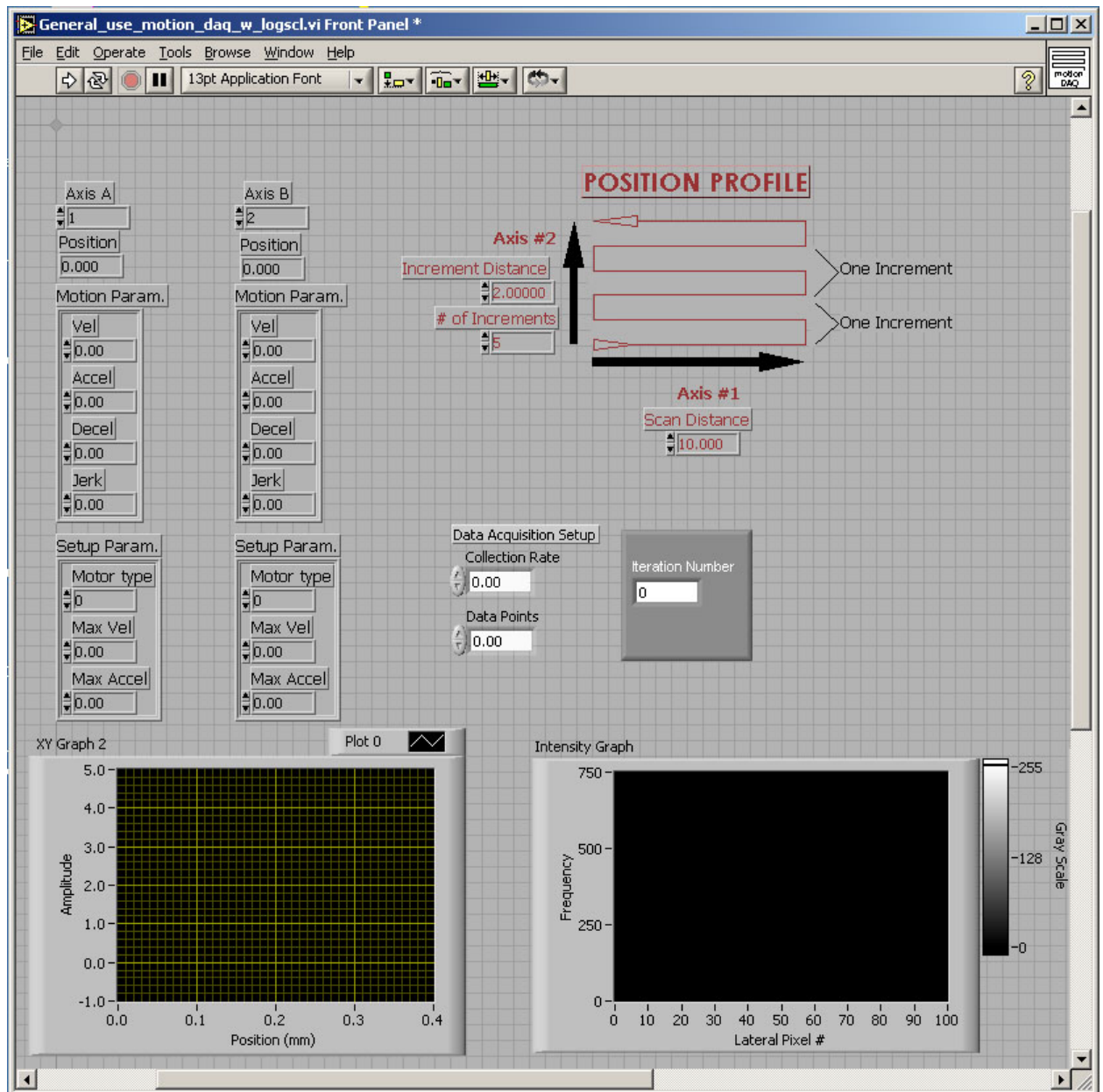


Figure B.1: The screen capture of the LabView interface where the parameters for imaging are entered. Such parameters are the speed of the stages, the distance they travel at each step, the sampling rate of the data acquisition and the number of samples recorded at each axial-scan.

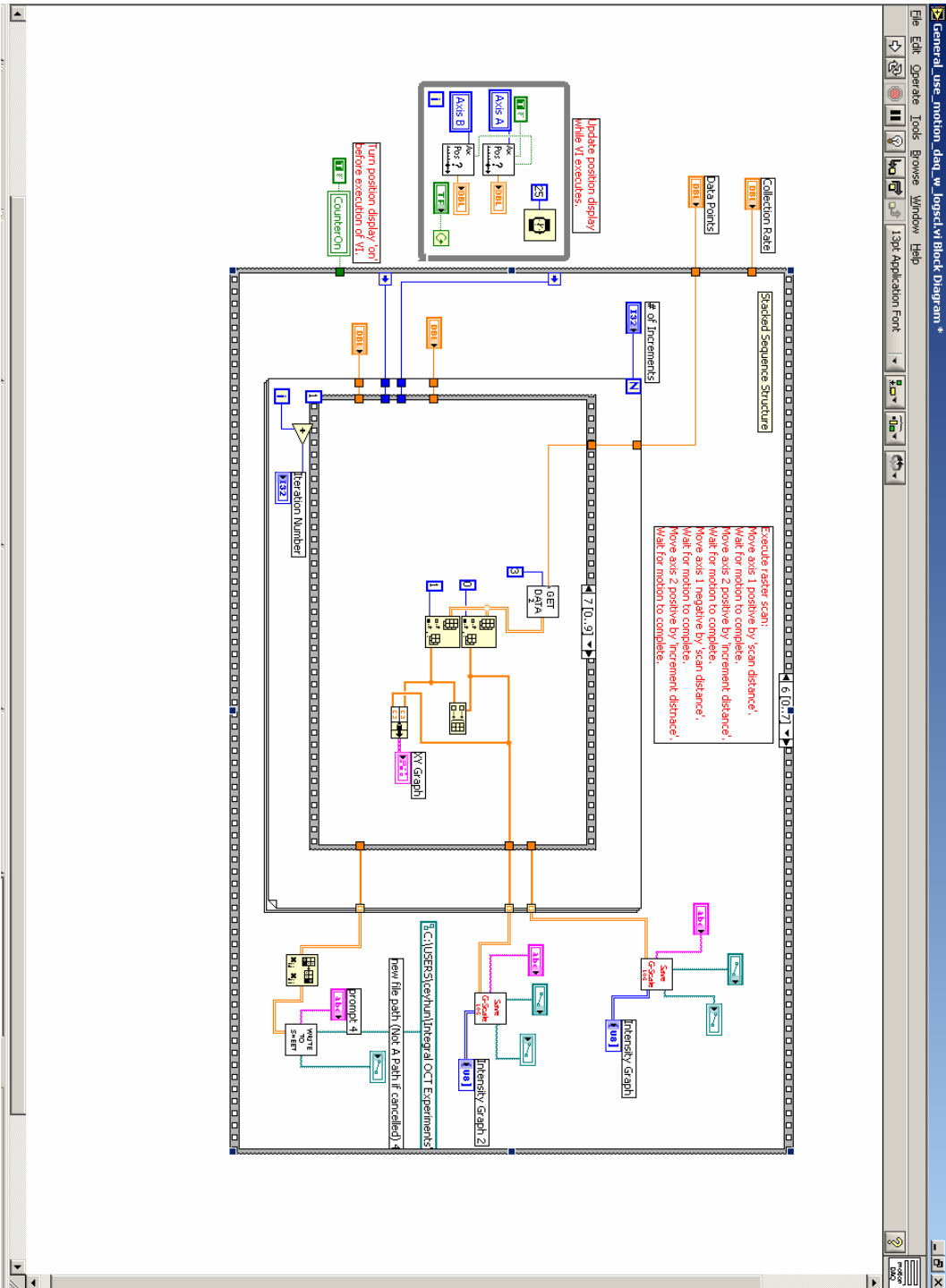


Figure B.2: A screen capture of the LabView blockdiagram of the code controlling the stages and DAQ

LIST OF REFERENCES

- [Aguirre 2003] Aguirre, A.D., Hsiung, P., Ko, T.H., Hartl, I., and Fujimoto, J.G. (2003). High-speed optical coherence microscopy for high-speed, *in-vivo* cellular imaging. *Optics Letter* 28, 2064-2066.
- [Akçay 2001] Akçay, A.C. (2001). "Fiber optic interferometer for optical coherence microscopy imaging," M.S. Thesis, University of Central Florida, Orlando, FL.
- [Akçay 2002] Akçay, A.C., Parrein, P.P., and Rolland, J.P. (2002). Estimation of longitudinal resolution in optical coherence imaging. *Applied Optics* 41, 5256-5262.
- [Akçay 2003] Akçay, A.C., Rolland, J.P., and Eichenholz, J.M. (2003). Spectral shaping to improve the point spread function in optical coherence tomography. *Optics Letters*, 28, 1921-1923.
- [Akçay 2005a] Akçay, A.C., Lee, K.S., and Rolland, J.P. (2005). Dispersion manipulation in optical coherence tomography with Fourier-domain optical delay line. in Coherence Domain Optical Methods and Optical Coherence Tomography in Biomedicine IX, V.V. Tuchin, J.A. Izatt, and J.G. Fujimoto eds., *Proc. SPIE 5690*, 512-522.
- [Akçay 2005b] Akçay, A.C., Clarkson, E., and Rolland, J.P. (2005). The impact of source spectral shape on task-based assessment of detection and resolution in OCT. *Applied Optics* (accepted).
- [Akçay 2005c] Akçay, A.C., Furenlid, L.R., Costa, M.A., and Rolland, J.P. (2005) Compact low-cost detection electronics for optical coherence imaging. *Electronics Letters* (submitted).
- [Anderson 1981] Anderson, R.R. and Parrish, J.A. (1981). The Optics of Human Skin. *The Journal of Investigative Dermatology*, 77, 13-19.

- [Barrett 1990] Barrett, H.H. (1990). Objective assessment of image quality: effects of quantum noise and object variability. *JOSA A* 7, 1266-1278.
- [Barrett 1998] Barrett, H.H., Abbey, C.K., and Clarkson, E. (1998). Objective assessment of image quality. III. ROC metrics, ideal observers, and likelihood-generating functions. *JOSA A* 15, 1520-1535.
- [Barrett 2004] Barrett, H.H., and Myers, K.J., Ed. Saleh, B.E.A. (2004). *Foundations of Image Science*. Wiley Series in Pure and Applied Optics, Hoboken, New Jersey.
- [Bashkansky 1998a] Bashkansky, M., Duncan, M.D., Goldberg, L., Koplow, J.P., and Reintjes, J. (1998). Characteristics of a Yb-doped superfluorescent fiber source for use in optical coherence tomography. *Optics Express* 3, 305-310.
<http://www.opticsexpress.org/abstract.cfm?URI=OPEX-3-8-305>
- [Bashkansky 1998b] Bashkansky, M., Duncan, M.D. and Reintjes, J. (1998). Signal Processing for Improving Field Cross-correlation Function in Optical Coherence Tomography. *Applied Optics* 37, 8137 (1998).
- [Bizheva 2003] Bizheva, K., Povazay, B., Hermann, B., Sattmann, H., Drexler, W., Mei, M., Holzwarth, R., Hoelzenbein, T., Wacheck, W. and Pehamberger, H. (2003). Compact, broad-bandwidth fiber laser for sub-2-mm axial resolution optical coherence tomography in the 1300-nm wavelength region. *Optics Letters*, 28, 707-709.
- [Born and Wolf 2002] Born, M. and Wolf, E. (2002). *Principles of Optics 7th (expanded) edition*. University Press, Cambridge.

- [Bouma 1995] Bouma, B., Tearney, G.J., Boppart, S.A., Hee, M.R., Brezinski, M.E. and Fujimoto, J.G. (1995). High-resolution optical coherence tomographic imaging using a mode-locked Ti:Al₂O₃ laser source. *Optics Letters*, 20, 1486-1488.
- [Bouma 1996] Bouma, B., Tearney, G.J., Bilinsky, I.P., Golubovic, B. and Fujimoto, J.G. (1996). Self-phase-modulated Kerr-lens mode-locked Cr:forsterite laser source for optical coherence tomography. *Optics Letters*, 21, 1839-1841.
- [Bouma 2002] Bouma, B.E., and Tearney, G.J. (2002). "Optical Sources," in *Handbook of Optical Coherence Tomography*, B. E. Bouma, and G. J. Tearney, eds. (Marcel Dekker, Inc., New York, 67-97.
- [Bourquin 2003] Bourquin, S., Aguirre, A.D., Hartl, I., Hsiung, P., Ko, T.H., Fujimoto, J.G., Birks, T.A., Wadsworth, W.J., Bunting, U., and Kopf, D. (2003). Ultrahigh resolution realtime OCT imaging using a compact femtosecond Nd:Glass laser and nonlinear fiber. *Optics Express* 11, 3290-3297. <http://www.opticsexpress.org/abstract.cfm?URI=OPEX-11-24-3290>
- [Bracewell 1965] Bracewell, R. (1965). *The Fourier Transform and Its Applications*, (McGraw-Hill, Inc., New York), Ch. 8.
- [Bruno 2003] Bruno, O.P. and Chaubell, J. (2003). Inverse scattering problem for optical coherence tomography. *Optics Letters*, 28, 2049-2051.
- [Chinn 1993] Chinn, S.R., and Swanson, E.A. (1993). Blindness limitations in optical coherence domain reflectometry. *Electronics Letters* 29, 2025-2027.

- [Clark 2004] Clark, A.L., Gillenwater, A. Alizadeh-Naderi, R., El-Naggar, A.K., and Richards-Kortum, R. (2004). Detection and diagnosis of oral neoplasia with an optical coherence microscope. *J. of Biomedical Optics* 9(6), 1271-1280.
- [Clivaz 1992] Clivaz, X. Marquis-Weible, F. Salathe, R.P. Novak R.P. and Gilgen, H.H. (1992). High-resolution reflectometry in biological tissues. *Optics Letters*, 17, 4-6.
- [Colston 1998] Colston, Jr., B.W., Sathyam, U.S., DaSilva, L.B., Everett, M.J., Stroeve, P., and Otis, L.L. (1998). Dental OCT. *Optics Express*, 3, 230-238.
<http://www.opticsexpress.org/abstract.cfm?URI=OPEX-3-6-230>.
- [Crowe 1993] Crowe, D.G., Shamir, J., and Ryan, T.W. (1993). "Sidelobe reduction in optical signal processing," *Applied Optics* 32, 179.
- [Danielson 1987] Danielson, B.L. and Whittenberg, C.D. (1987). Guided-wave reflectometry with micrometer resolution. *Applied Optics*, 26, 2836-2842
- [Danielson 1991] Danielson, B.L. and Boisrobert, C.Y. (1991). Absolute optical ranging using low coherence interferometry. *Applied Optics*, 30, 2975-2979.
- [de Boer 1999] de Boer, J.F., Srinivas, S.M., Park, B.H., Pham, T.H., Chen, Z., Milner, T.E., and Nelson, J.S. (1999). Polarization Effects in Optical Coherence Tomography of Various Biological Tissues. *IEEE J. of Selected Topics in Quantum Electronics*, 5, 1200-1204.
- [de Boer 2001] de Boer, J.F., Saxer, C.E., and Nelson, J.S. (2001). Stable carrier generation and phase-resolved digital data processing in optical coherence tomography. *Applied Optics* 40, 5787-5790.

- [de Boer 2002] de Boer, J.F., and Milnet, T.E. (2002). Review of polarization sensitive optical coherence tomography and Stokes vector determination. *J. of Biomedical Optics* 7(3), 359-371.
- [Destouches 2005] Destouches, N., Tishchenko, A.V., Pommier, J.C., Reynaud, S., Parriaux, O., Tonchev, S. and Ahmed, M.A. (2005). 99% efficiency measured in the -1st order of a resonant grating. *Opt. Express* 13, 3230-3235.
<http://www.opticsexpress.org/abstract.cfm?URI=OPEX-13-9-3230>
- [Drexler 1999] Drexler, W., Morgner, U., Kartner, F.X., Pitris, C., Boppart, S.A., Li, X.D., Ippen, E.P. and Fujimoto J.G. (1999). *In vivo* ultrahigh resolution optical coherence tomography. *Optics Letters*, 24, 1221-1223.
- [Dudley 2003] Dudley, D., Duncan, W., and Slaughter, J. (2003). "Emerging Digital Micromirror Device (DMD) Applications," in *MOEMS Display and Imaging Systems*, H. Urey, ed., Proc. SPIE 4985, 14-25.
- [Duncan 2002] Duncan, W.D., Bartlett, T., Lee, B., Powell, D., Rancuret, P., and Sawyers, B. (2002). "Dynamic optical filtering in DWDM systems using DMD," *Solid State Electronics* 46,1583-1585.
- [Duncan 2003] Duncan, W., Lee, B., Rancuret, P., Sawyers, B., Stalcup, W., Endsley, L., and Powell, D. (2003). "DLP™ Switched Blaze Grating; the Heart of Optical Signal Processing," in *MOEMS and Miniaturized Systems III*, J. H. Smith, ed., Proc. SPIE 4983, 297-304.

[Feldchtein 1998] Feldchtein, F.I., Gelikonov, G.V., Gelikonov, V.M., Kuranov, R.V., Sergeev, A.M., Gladkova, N.D., Shakhov, A.V., Shakhova, N.M., Snopova, L.B., Terent'eva, A.B., Zagainova, E.V., Chumakov, Yu.P., and Kuznetzova, I.A. (1998). Endoscopic applications of optical coherence tomography. *Optics Express*, 3, 257-270.

<http://www.opticsexpress.org/abstract.cfm?URI=OPEX-3-6-257>.

[Fenster 2000] Fenster, A. and Downey, D.B. (2000). *Three-Dimensional Ultrasound Imaging*. Handbook of Medical Imaging, Chapter 7, SPIE Press: Bellingham, Washington.

[Fercher 1988] Fercher, A.F. Mengedoht, K. and Werner W. (1988). Eye-length measurement by interferometry with partially coherent light. *Optics Letters*, 13, 186-188.

[Fercher 1996] Fercher, A.F. (1996). Optical coherence tomography. *J. Biomed. Opt.* 1(2), 157-173.

[Fercher 2000] Fercher, A.F., Hitzenberger, C.K., Sticker, M., Moreno-Barriuso, E., Leitgeb, R., Drexler, W. and Sattmann, H. (2000). A thermal light source technique for optical coherence tomography. *Optics Communications*, 185, 57-64.

[Fercher 2002] Fercher, A.F., and Hitzenberger, C.K. (2002). *Optical coherence tomography*, in Progress in Optics 44, Wolf, E. ed., Elsevier Science B.V., 215-302.

[Fercher 2003] Fercher, A.F., Drexler, W., Hitzenberger, C.K., and Lasser, T. (2003). Optical coherence tomography - principles and applications. *Rep. Prog. Phys.* 66, 239-303.

[Fiete 1987] Fiete, R.D., Barrett, H.H., Smith, W.E., and Myers, K.J. (1987). Hotelling trace criterion and its correlation with human-observer performance. *JOSA A* 4, 945-953.

- [Fujimoto 1986] Fujimoto, J.G. De Silvestri S. Ippen, E.P. Puliafito, C.A. Margolis, R. and Oseroff, A. (1986). Femtosecond optical ranging in biological systems. *Optics Letters*, *11*, 150-152.
- [Gilgen 1989] Gilgen, H.H., Novak, R.P., Salathe, R.P., Hodel, W. and Beaud, P. (1989). Submillimeter Optical Reflectometry. *Journal of Lightwave Technology*, *7*, 1225-1233.
- [Goodman 1985] Goodman, J.W. (1985) *Statistical Optics*. John Wiley & Sons, Inc. New York., Ch. 5, Ch. 7.
- [Haykin 1994] Haykin, S. (1994). *Communication Systems*. John Wiley & Sons, Inc. New York.
- [Hee 1992] Hee, M.R., Huang, D., Swanson, E.A., and Fujimoto, J.G. (1992). Polarization-sensitive low-coherence reflectometer for birefringence characterization and ranging. *JOSA B*, *9*, 903-908.
- [Hee 2002] Hee, M.R. (2002). *Optical Coherence Tomography: Theory*, in Handbook of Optical Coherence Tomography, Bouma, B.E. and Tearney, G.J. eds. Marcel Dekker, Inc. New York, NY, 41-66.
- [Hitzenberger 1999] Hitzenberger, C.K., Baumgartner, A., Drexler, W., Fercher, A.F. (1999). Dispersion Effects in Partial Coherence Interferometry: Implications for Intraocular Ranging. *J. of Biomedical Optics* *4(1)*, 144-151.
- [Hoeling 2000] Hoeling, B.M., Fernandez, A.D., Haskell, R.C., Huang, E., Myers, W.R., Petersen, D., Ungersma, S.E., Wang, R., Williams, M.E., and Fraser, S.E. (2000). An optical coherence microscope for 3-dimensional imaging in developmental biology. *Optics Express* *6*, 136. <http://www.opticsexpress.org/abstract.cfm?URI=OPEX-6-7-136>.

- [Horowitz 1980] Horowitz, P., and Hill, W. (1980). *The art of electronics*. Cambridge University Press, New York, NY.
- [Huang 1991a] Huang, D. Swanson, E.A. Lin, C.P. Schuman, J.S. Stinson, W.G. Chang, W. Hee, M.R. Flotte, T. Gregory, K. Puliafito, C.A. and Fujimoto, J.G. (Nov. 1991). Optical Coherence Tomography. *Science*, 254, 1178-1181.
- [Huang 1991b] Huang, D.; Wang, J. Lin, C.P. Puliafito, C.A. and Fujimoto, J.G. (1991). Micron-Resolution Ranging of Cornea Anterior Chamber by Optical Reflectometry. *Lasers in Surgery and Medicine*, 11, 419-425.
- [Izatt 1994] Izatt, J.A., Hee, M.R., Owen, G.M., Swanson, E.A. and Fujimoto, J.G. (1994). Optical coherence microscopy in scattering media. *Optics Letters*, 19, 590-592.
- [Izatt 1996] Izatt, J.A., Kulkarni, M.D., Wang, H., Kobayashi, K. and Sivak, M.V. (1996). Optical Coherence Tomography and Microscopy in Gastrointestinal Tissues. *IEEE J. of Selected Topics in Quantum Electronics*, 2, 1017-1028.
- [Kariya 2004] Kariya, R., Mathine, D.L., and Barton, J.K. (2004). Analog CMOS Circuit Design and Characterization for Optical Coherence Tomography Signal Processing. *IEEE Trans. Biomed. Eng.* 51, 2160-2163.
- [Kholodynkh 2003] Kholodynkh, A.I., Petrova, I.Y., Larin, K.V., Motamedi, M. and Esenaliev, R.O. (2003). Precision of measurement of tissue optical properties with optical coherence tomography. *Applied Optics*, 42, 3027-3037.
- [Ko 2004] Ko, T.H., Adler, D.C., Fujimoto, J.G., Mamedov, D., Prokhorov, V., Shidlovski, V., Yakubovich, S. (2004). Ultrahigh resolution optical coherence tomography with a

broadband superluminescent light source. *Optics Express* 12, 2112-2119.

<http://www.opticsexpress.org/abstract.cfm?URI=OPEX-12-10-2112>

[Kulkarni 1997] Kulkarni, M.D., Thomas, C.W., and Izatt, J.A. (1997) Image enhancement in optical coherence tomography using deconvolution. *Electronics Letters* 33, 1365-1367.

[Kwong 1993] Kwong, K.F., Yankelevich, D., Chu, K.C., Heritage, J.P. and Dienes, A. (1993). 400-Hz mechanical scanning optical delay line. *Optics Letters*, 18, 558-560.

[Laubscher 2002] Laubscher, M., Ducros, M, Karamata, B., Lasser, T., and Salathe, R. (2002). Video-rate three-dimensional optical coherence tomography. *Optics Express* 10, 429-435.

[Lee 2005] Lee, K.S., Akcay, A.C., Delemos, T., Clarkson, E., and Rolland, J.P. (2005). Dispersion control with Fourier-domain optical delay line in a fiber optic imaging interferometer. *Applied Optics*, 44, 4009-4022.

[Macovski 1983] Macovski, A. (1983). *Medical Imaging Systems*, Prentice-Hall, Englewood Cliffs.

[Mandel and Wolf 1995] Mandel, L. and Wolf, E. (1995). *Optical Coherence and Quantum Optics*. Cambridge University Press, New York.

[Masters 1999] Masters, B.R. (1999). Early Development of Optical Low-Coherence Reflectometry and Some Recent Biomedical Applications. *J. of Biomedical Optics*, 4, 236-247.

[Michelson 1881] Michelson, A.A. (1881). The relative motion of the Earth and the Luminiferous ether. *American Journal of Science*, 128, 120-129.

[Michelson 1887] Michelson, A.A.; Morley, E.W. (1887). On the Relative Motion of the Earth and Luminiferous Ether. *American Journal of Science*, 203, 333-345.

- [Mobley 2003] Mobley, J., and Vo-Dinh, T. (2003). Optical Properties of Tissue. In *Biomedical Photonics Handbook*. Vo-Dinh, T. eds. CRC Press. Ch. 2.
- [Myers 1985] Myers, K.J., Barrett, H.H., Borgstorm, M.C., Patton, D.D., and Seelye, G.W. (1985). Effect of noise correlation on detectability of disk signals in medical imaging. *J. Opt. Soc. Am. A*, 2, 1752-1759.
- [Nash 1999] Nash, E. (1999). Ask the Applications Engineer – 28, Logarithmic Amplifiers Explained. *Analog Dialogue* 33.
<http://www.analog.com/library/analogDialogue/archives/33-03/ask28/log-amps.pdf>.
- [Pan 1995] Pan, Y., Birngruber, R., Rosperich, J. and Engelhardt, R. (1995). Low-coherence optical tomography in turbid tissue: theoretical analysis. *Applied Optics*, 34, 6564-6574.
- [Pan 2001] Pan, Y., Xie, H., and Fedder, G.K. (2001). Endoscopic optical coherence tomography based on a microelectromechanical mirror. *Optics Letters*, 26, 1966-1968.
- [Parrish 1981] Parrish, J.A. (1981). New Concepts in Therapeutic Photomedicine: Photochemistry, Optical Targeting and the Therapeutic Window. *Journal of Investigative Dermatology* 77, 45-50.
- [Podoleanu 1999] Podoleanu, A.G., Rogers, J.A., and Jackson, D.A. (1999). OCT *En-face* Images from the Retina with Adjustable Depth Resolution in Real Time. *IEEE J. of Selected Topics in Quantum Electronics*, 5, 1176-1184.
- [Podoleanu 2000] Podoleanu, A. (2000). Unbalanced versus balanced operation in an optical coherence tomography system. *Applied Optics*, 39, 173-182.
- [Povazay 2002] Povazay, B., Bizheva, K., Unterhuber, A., Hermann, B., Sattmann, H., Fercher, A.F., Drexler, W., Apolonski, A., Wadsworth, W.J., Knight, J.C., Russell, P.St.J.,

- Vetterlein, M. and Scherzer, E. (2002). Submicrometer axial resolution optical coherence tomography. *Optics Letters*, 27, 1800-1802.
- [Qi 2004] Qi, B., Himmer, A.P., Gordon, L.M., Yang, X.D.V., Dickensheets, L.D., and Vitkin, I.A. (2004). Dynamic focus control in high-speed optical coherence tomography based on a microelectromechanical mirror. *Optics Communications* 232, 123-128.
- [Riza 2003] Riza, N., and Mughal, M.J. (2003) Broadband optical equalizer using fault-tolerant digital micromirror. *Optics Express*, 11, 1559-1565.
<http://www.opticsexpress.org/abstract.cfm?URI=OPEX-11-13-1559>.
- [Roggan 1999] Roggan, A., Friebel, M., Dörshel, K., Hahn, A. And Müller, G. (1999). Optical properties of circulation human blood in the wavelength range 400-2500nm. *Journal of Biomedical Optics*, 4(1), 36-46.
- [Rolland 1992] Rolland, J.P., Barrett, H.H. (1992). Effect of random background inhomogeneity on observer detection performance. *J. Opt. Soc. Am. A*, 9, 649-658.
- [Rolland 2004] Rolland, J.P., O'Daniel, J., Clarkson, E., Cheong, K., Akcay, C.A., Parrein, P., DeLemos, T. and Lee, K.S. (2004). AUC-based resolution quantification in optical coherence tomography. in Medical Imaging: Im. Percep., Obs. Per. Tech. Asses., D. P Chakraborty and M. P. Eckstein, eds., *Proc. SPIE 5372*, 334-343.
- [Rolland 2005] Rolland, J., O'Daniel, J., Akcay, C., DeLemos, T., Lee, K.S., Cheong, K., Clarkson, E., Chakrabarti, R., and Ferris, R. (2005), Task-based optimization and performance assessment in optical coherence imaging. *J. Opt. Soc. Am. A*, 22, 1132-1142.
- [Rollins 1998] Rollins, A.M., Kulkarni, M.D., Yazdanfar, S., Ung-arunyawee, R. and Izatt, J.A. (1998). *In vivo* video rate optical coherence tomography. *Optics Express*, 3, 219-229.

- [Rollins 1999] Rollins, A.M., and Izatt, J.A. (1999). Optimal interferometer designs for optical coherence tomography. *Optics Letters*, 24, 1484-1486.
- [Sato 2000] Sato, M., Seino, K., Onodera, K., and Tanno, N. (2000). Phase-drift suppression using harmonics in heterodyne detection and its applications in optical coherence tomography. *Optics Communications* 184, 95-104.
- [Schaefer 2004] Schaefer, A.W., Reynolds, J.J., Marks, D.L. and Boppart, S.A. (2004). Real-time Digital Signal Processing-Based Optical Coherence Tomography and Doppler Optical Coherence Tomography. *IEEE Trans. Biomed. Eng.* 51, 186-190.
- [Schmitt 1993] Schmitt, J.M., Knuttel, A. and Bonner, R.F. (1993). Measurement of optical properties of biological tissues by low-coherence reflectometry. *Applied Optics*, 32, 6032-6042.
- [Schmitt 1997a] Schmitt, J.M., Lee, S.L. and Yung, K.M. (1997). An optical coherence microscope with enhanced resolving power in thick tissue. *Optics Communication*, 142, 203-207.
- [Schmitt 1997b] Schmitt, J.M. and Knuttel, A. (1997). Model of optical coherence tomography of heterogeneous tissue. *J. Opt. Soc. Am. A*, 14, 1231-1242.
- [Schmitt 1997c] Schmitt, J.M., Lee, S.L., and Yu, K.M. (1997). An optical coherence microscope with enhanced resolving power in thick tissue. *Optics Communications* 142, 203-207.
- [Schmitt 1998] Schmitt, J.M. (1998). Restoration of Optical Coherence Images of Living Tissue Using The Clean Algorithm. *J. of Biomedical Optics* 3(1), 66-75.

- [Smith 1986] Smith, W.E., Barrett, H.H. (1986). Hotelling trace criterion as a figure of merit for the optimization of imaging systems. *J. Opt. Soc. Am. A*, 3, 717-725.
- [Sticker 2002] Sticker, M., Pircher, M., Götzinger, E., Sattmann, H., Fercher, A.F. and Hitzenberger, C.K. (2002). *En face* imaging of single cell layers by differential phase-contrast optical coherence microscopy. *Optics Letter*, 27, 1126-1128.
- [Superlum 2005] Superlum Diodes Ltd., Russia. SLD Based Products (2005).
http://www.superlumdiodes.com/sld_based.htm
- [Szydlo 1998] Szydlo, J., Delachenal, N., Gianotti, R., Walti, R., Bleuler, H. and Salathe, R.P. (1998). Air-turbine driven optical low-coherence reflectometry at 28.6-kHz scan repetition rate. *Optics Communication*, 154, 1-4.
- [Takada 1987] Takada, K., Yokohama, I., Chida, K. and Noda, J. (1987). New measurement system for fault location in optical waveguide devices based on an interferometric technique. *Applied Optics*, 26, 1603-1606.
- [Tearney 1995] Tearney, G.J., Brezinski, M.E., Southern, J.F., Bouma, B.E., Hee, M.R., and Fujimoto, J.G. (1995). Determination of the refractive index of highly scattering human tissue by optical coherence tomography. *Optics Letters*, 20, 2258-2260.
- [Tearney 1996] Tearney, G.J., Bouma, B.E., Boppart, S.A., Golubovic, B., Swanson, E.A. and Fujimoto, J.G. (1996). Rapid acquisition of *in vivo* biological images by use of optical coherence tomography. *Optics Letters*, 21, 1408-1410.
- [Tearney 1997a] Tearney, G.J., Bouma, B. and Fujimoto, J.G.(1997). High-speed phase- and group-delay scanning with a grating-based phase control delay line. *Optics Letters*, 22, 1811-1813.

- [Tearney 1997b] Tearney, G.J., Brezinski, M.E., Bouma, B., Boppart, S.A., Pitris, C., Southern, J.F., and Fujimoto, J.G. (1997). In vivo Endoscopic Optical Biopsy with Optical Coherence Tomography. *Science*, 276, 2037-2039.
- [Thrane 2000] Thrane, L., Yura, H.T. and Andersen, P.E. (2000). Analysis of optical coherence tomography systems based on the extended Huygens-Fresnel principle. *J. Opt. Soc. Am. A*, 17, 484-490.
- [Tripathi 2002] Tripathi, R. Nassif, N., Nelson, J.S., Park, B.H., and de Boer, J.F. (2002). “Spectral Shaping for non-Gaussian source spectra in optical coherence tomography,” *Optics Letters* 27, 406-408.
- [Tuchin 2002] Tuchin, V.V. (2002) *Introduction to Optical Biomedical Diagnostics*. Handbook of Optical Biomedical Diagnostics, Tuchin, V.V. ed. SPIE Press: Bellingham, Washington.
- [US Patent No. 4,319,190] Brown, T.R. (1982). Nuclear magnetic resonance imaging in space and frequency coordinates.
- [Vabre 2002] Vabre, L., Dubois, A. and Boccara, A.C. (2002). Thermal-light full-field optical coherence tomography. *Optics Letter*, 27, 530-532.
- [Wang 1999] Wang, L., and Weiner, A.M. (1999). Programmable spectral phase coding of an amplified spontaneous emission light source. *Optics Communications*, 167, 211-224.
- [Weiner 1988] Weiner, A.M., Heritage, J.P. and Kirschner, E.M. (1988). High-resolution femtosecond pulse shaping. *J. Opt. Soc. Am. B*, 5, 1563-1572.
- [Weiner 2000] Weiner, A.M. (2000). Femtosecond pulse shaping using spatial light modulators. *Rev. of Sci. Instruments*, 71, 1929-1960.

- [Welzel 2001] Welzel, J. (2001). Optical coherence tomography in dermatology: a review. *Skin Research and Technology*, 7, 1-9.
- [Wollenweber 1999] Wollenweber, S.D., Tsui, B.M.W., Lalush, D.S., Frey, E.C., LaCroix, K.J., and G.T. Gullberg, G.T. (1999). Comparison of Hotelling Observer Models and Human Observers in Defect Detection from Myocardial SPECT imaging. *IEEE Trans. On Nuclear Science* 46, 2098-2103.
- [Xie 2003] Xie, T., Wang, Z., and Pan, Y. (2003). High-speed optical coherence tomography using fiberoptic acousto-optic phase modulation. *Optics Express* 11, 3210.
<http://www.opticsexpress.org/abstract.cfm?URI=OPEX-11-24-3210>.
- [Yadlowski 1995] Yadlowsky, M.J., Schmitt, J.M. and Bonner, R.F. (1995). Multiple scattering in optical coherence microscopy. *Applied Optics*, 34, 5699-5707.
- [Youngquist 1987] Youngquist, R.C., Carr, S. and Davies, D.E.N. (1987). Optical coherence-domain reflectometry: a new optical evaluation technique. *Optics Letters*, 12, 158-160.
- [Zhang 2001a] Zhang, Y., Sato, M., and Tanno, N. (2001). Numerical investigations of optimal synthesis of several low coherence source for resolution improvement. *Optics Communications* 192, 183-192.
- [Zhang 2001b] Zhang, Y., Sato, M., and Tanno, N. (2002). "Resolution improvement in optical coherence tomography by optimal synthesis of light-emitting diodes," *Optics Letters*. 26, 205-207.
- [Zvyagin 2003] Zvyagin, A.V., Smith, E.D.J. and Sampson, D.D. (2003). Delay and dispersion characteristics of a frequency-domain optical delay line for scanning interferometry. *J. Opt. Soc. Am. A*, 20, 333-341.